Visible Light Emission from Silicon-Based Optoelectronic Thin Films

Toshihiko TOYAMA

January, 1997

Osaka University
Faculty of Engineering Science
Toyonaka, Osaka

Visible Light Emission from Silicon-Based Optoelectronic Thin Films

シリコン系機能薄膜材料からの可視域発光に関する研究

Toshihiko TOYAMA

January, 1997

大阪大学

Osaka University
Faculty of Engineering Science
Toyonaka, Osaka

VISIBLE LIGHT EMISSION FROM OPTOELECTRONIC SILICON THIN FILMS

Toshihiko TOYAMA

January, 1997

Abstract

A series of systematic studies has been carried out on the mechanism of visible light emission from optoelectronic silicon thin films, i.e. hydrogenated amorphous silicon (*a*-Si:H) and nanocrystalline Si (*nc*-Si).

Electroluminescence (EL) in *a*-Si:H at a high electric field has been investigated employing ac-driven double insulating EL devices. EL emission involving a spectral component above the optical energy gap has been observed at the internal electric field in *a*-Si:H over 1 MV/cm. Intraband transitions of hot-electrons in conduction bands are the most acceptable mechanism for the EL emission. The lucky drift model based on the phonon scattering process leads to the estimated mean free path of 1.0 nm. The average electron energy of 0.13 eV is estimated at the electric field in *a*-Si:H of 1 MV/cm. Utilizing the electroabsorption (EA) technique, the internal electric field in *a*-Si:H of the ac-driven double insulating EL devices has been found to saturate at the electric fields of 1.2–1.5 MV/cm with an increase in the applied voltage. Assuming the field distortion due to generation of the transferred charge, the estimated transferred charge is found to rise sharply above the threshold fields of 1.2–1.5 MV/cm. The experimental results have revealed one of the most important results, i.e. electron avalanche multiplication would occur in *a*-Si:H at an electric field over 1 MV/cm.

The extended investigations have been carried out for both the EL and EA

measurements concerning with the temperature dependence and the alloy-induced effects. The mean free paths deduced from the EL spectrum and the ionization rate show the similar temperature dependence. With an increase in the temperature from 130 K to 300 K, the mean free paths gradually decrease in accordance with the theoretical line based on the optical phonon scattering process. In contrast, the mean free paths turn to rise at the higher temperatures up to 400 K. The mean free paths of a-$Si_{1-x}C_x$:H alloys ($x < 0.3$) evaluated from the EL spectra tend to decrease with increasing the optical energy gaps, and this tendency on the optical energy gap is consistent with that observed by the polarized EA measurements at low electric fields. These results imply that the structural-disorder-induced effects might affect on the high energetic electron transport in a-Si:H as well as the phonon scattering process.

The red-band photoluminescence (PL) from electrochemically anodized *nc*-Si and the blue-band PL from rapidly grown *nc*-Si have been studied. The red-band emitting *nc*-Si thin films were fabricated from μc-Si prepared by plasma chemical vapor deposition (CVD). The *nc*-Si thin films exhibit the PL emission with a peak energy of 1.6–1.8 eV at room temperature and the PL properties are changed corresponding to the fabrication conditions including the anodizing current density, the anodizing time, the initial thickness and the crystalline volume fraction in μc-Si before anodization. The Raman scattering and PL results indicate that the emission model based on the amorphous-like passivating layer is unlikely to explain the PL emission, while quantum confinement effects and the surface states models would be responsible for the visible light emission. The crystallite size of 2.4–3.8 nm depends mainly on the deposition conditions of plasma CVD for μc-Si before anodization, while the surface states on the crystallites may be activated for the light emission due to anodization.

The blue-band emitting *nc*-Si thin films were fabricated by solid phase growth employing the rapid thermal annealing (RTA) method at 800–1200°C for 1–5 min in vacuum from a-Si:H. The PL occurs at room temperature with a peak energy of 2.5–2.7 eV, which is almost independent of the RTA temperature and time. By contrast, the PL intensity depends on the RTA conditions. The *nc*-Si possesses structural features distinguished from blue-band emitting Si in literature, i.e. the *nc*-Si consists of crystallites with a grain size as large as 50–100 nm and little amount of $Si\text{-}O_x$ bonds. Therefore the emission models based on *nc*-Si embedded

in SiO_x matrix including quantum confinement effects can not be adopted for this case. The differential optical transmittance spectrum of the *nc*-Si thin films exhibits three spectral features at 2.6–2.7 eV, 3.0–3.1 eV and 3.4 eV. Since the first feature corresponds to the PL peak energy of the film, the optical transition, which may be associated with the localized states on the boundary of *nc*-Si crystallites, is the most likely origin for the PL emission. The latter two spectral features would correspond to the optical transitions in the quasi three dimensional energy band structure in crystalline Si (*c*-Si).

Applying the acquired film properties, *a*-Si:H/*c*-Si heterojunction photodiodes and *nc*-Si-based thin film light emitting diodes (TFLEDs) have been developed. Various photocurrent properties in a heterojunction structure consisting of plasma-CVD-deposited *n*-type μc-Si (10 nm) and undoped *a*-Si:H (1.0 μm) layers on a p^+-type ion-implanted region in an *n*-type *c*-Si substrate have been investigated. The photocurrent multiplication factor over 30 and the signal-to-noise ratio of around 170 have been achieved without any marked increase in the dark current at the reverse bias voltage around 35 V. The entirely solid state TFLED has fabricated on a SnO_2-coated glass substrate using electrochemically anodized *p*-type *nc*-Si as a light emitting active layer. The TFLED, of which *p-i-n* structure consists of the *nc*-Si and amorphous layers, exhibits clear rectifying *J–V* characteristics, while the visible EL emission is observed with applying the negative bias voltage on the SnO_2 electrode. The EL emission peak energy locates at 1.8 eV and observed emission color is orange-red.

ACKNOWLEDGMENT

This work has been done at the Semiconductor Laboratory, Department Electrical Engineering, Faculty of Engineering Science, Osaka University, Toyonaka, Osaka under the direction of Professor Hiroaki Okamoto and Professor emeritus Yoshihiro Hamakawa.

The author would like to express his sincere thanks to Professor Hiroaki Okamoto for his constant advice and encouragement throughout the course of this thesis work and critical reading of this thesis.

The author is extremely grateful to Professor Takeshi Kobayashi and Professor Masauki Okuyama for the kind advice and critical reading of this thesis.

The author is deeply grateful to Professor emeritus Yoshihiro Hamakawa for his constant instructive and heartfelt advice and also his critical reading of this thesis. This work would not have completed without his support.

The author wishes to make deep acknowledgment to Professor Sadahiko Yamamoto, Professor Kenji Gamo and Professor Tetsuro Kobayashi for their kind and useful guidance in the course of this study at Osaka University.

The author is much indebted to Dr. Kiminori Hattori, Mr. Kaoru Yamashita and Dr. Takeshi Kanashima of the Laboratory, Professor Taneo Nishino of Kobe University and Professor Hideyuki Takakura of Ritsumeikan University for their useful advice and discussions throughout the course study.

The author would like to express sincere gratitude to Mr. Chitose Sada of the Laboratory for his kind encouragement, useful discussion and skillful technical assistance throughout thesis work.

The author wishes to give his highest appreciation to his seniors, Professor Dusit Kruangam of Chulalongkorn University, Dr. Sasha M. Paasche, Messrs. Masahiro Deguchi and Yutaka Hattori for their kind encouragement and useful advice since the start of his research work. The author is gratefully indebted to Dr. Yasuo Tsutsumi, Dr. Yoshiteru Nitta and Mr. Katsunori Abe for their helpful advice.

The author wishes to express his gratitude to his collaborators in the Semiconductor Laboratory, Dr. Masashi Yoshimi, Dr. Claus-Dieter Abel and Mr. Kouichi Ishida for their valuable and enjoyable discussion.

The author is especially indebted to Messrs. Kazuhiro Hiratsuka, Takashi Ouchida and Tetsuyuki Matsui for their enthusiastic and excellent collaboration. The author would like to thank to Messrs. Teruaki Yamamoto, Yasuhito Kurokawa, Yoshihiro Kotani, and Takayuki Goto for their active work.

The author is indebted to his coworkers in the days of Eastman Kodak (Japan) Ltd., Dr. Yukio Tanaka, Dr. Ryoichi Tohmon and Mr. Tsuguto Takeuchi for their kind and enjoyable discussions. The author wishes to thank to the members, Dr. Uichi Itoh, Messrs. Yoshikatsu Asano, Masayuki Kuwabara, Hirokazu Ohta, Tohru Nukui, Takashi Ehara, Kazuyoshi Tsukuda and Ms. Shinobu Shinohara for their variable encouragement.

The author appreciates active and enjoyable discussions with the colloquies, Messrs. Wahid Shams-Kolahi, Kholid Ahamad, Young-Jae Cho and Kousaku Shimizu.

The author wishes to thank to his friends, Messrs. Takeshi Mori, Yoshiki Nakatani, Hisayoshi Fujikawa, Hiroshi Suzawa and Kazuhiro Tsuruta for their kind helpfulness.

Finally, the author wishes to thank his parents for their endless and warm encouragement.

Contents

Chapter I

Introduction

1.1. Historical Background

The eye of the human being can detect electro-magnetic wave with a wavelength in the range from ~380 nm to ~720 nm, i.e. the human being can see due to "visible light". The human being thereby gains a large amount of information reflected by the visible light via the eye. Then he has been naturally fascinated by the light emission and made great endeavors to acquire the light source instead of the sun light for thousands years. Today, we have obtained one of the ideal sources for the visible light, i.e. light emitting diodes (LEDs) and laser diodes due to great advances of the science and technologies centered upon compound semiconductors represented by AlGaAs. However the desire for a novel light source still continues.

Silicon is the dominant material in the semiconductor science as well as the microelectronics industry, and is likely to remain so for many years to come. [1] First industrial success has achieved on bulk crystalline Si (*c*-Si) which is applied toward micro-devices including microprocessors, memories and light detectors. Second industrial evolution has carried out due to the synthesis of optoelectronic Si thin films being representative of hydrogenated amorphous silicon (*a*-Si:H). [2] Remarkable advances have been made in the science and technology of the "giant-microelectronic" *a*-Si:H devices (i.e. large area devices composed by a great number of microelectronic elements) involving thin film transistors (TFTs) for active matrix liquid crystal displays (AMLCDs) [3] and two dimensional image sensor arrays. [4]

In contrast, as for the visible light emission, Si possesses a poor property due to the indirect energy band structure, that means that direct, radiative, band-to-band transitions are forbidden by the *k*-conservation selection rule. Therefore the light emission from Si has been almost centered upon the infrared light emission at low temperatures with an interest for the exciton or phonon behaviors. Nevertheless, two exceptions have been found in conjunction with the visible light emission from Si at room temperature; one is electroluminescence (EL) from *c*-Si devices at high electric fields and the other is luminescence from the low dimensional Si.

Visible light emission from bulk Si at high electric field has been already found in 1955. Breakdown radiation from "red-spot", or micro-plasmas, in Si *p-n* junctions was first reported by Newman *et al.* [5] and since then many papers have been devoted to the phenomenon until early 1960's. [6,7] The authors have been interested in the luminescence as a precursor of the nonlinear carrier transport phenomenon at high electric fields, i.e. hot-carrier-induced avalanche multiplication. [8,9] In 1981, Child *et al.* have re-focused upon the hot-carrier-induced EL. [10] They have reported the EL in miniaturized metal-oxide-semiconductor field-effect transistors (MOSFETs), and since then the large efforts have been performed on the analysis of the luminescence in MOSFETs related to the device degradation. [11–13] In submicrometer MOSFETs, the hot carrier injection limits the device reliability. [14] Consequently, the visible EL from *c*-Si at high electric fields is playing a role as a probe getting the physical information with repect to behaviors of hot carriers as well as aquiring the technological information on device performances.

Visible luminescence from low dimensional Si, in which the *k*-conservation selection rule will be relaxed, is one of the most exciting topics in recent several years. [15] The study has carried out on various Si systems, for example, Si/SiGe superlattice as the two dimensional system, [16] Si wire etched by ion beam as the one dimensional system, [17] and Si nano-sized particle as the zero dimensional system. [18] The most widely studied material is electrochemically anodized Si, i.e. porous Si as one or zero dimensional system. In 1990, the two groups have reported independently on the strong photoluminescence (PL) including visible light from porous Si at room temperature. [19,20] Canham has described that quantum confinement effects at quantum wires incorporated into porous Si are

responsible for the strong PL at room temperature. [19]

Since their reports, the PL from Si fabricated by various techniques have tremendously examined, then the spectral range of the PL has widely covered from infrared to ultraviolet. [21,22] The mainly studied PL is in the far-red to orange-yellow region, which we shall denote simply as the *"red-band"* PL in this article. In addition, PL in the green to violet region is studied due to some chemical treatments or synthetic fabrication techniques, which we shall denote as the *"blue-band"* PL. Canham has assorted the PL from the viewpoint of decay time, i.e. he denotes the S-band (slow-band) PL corresponding to the red-band PL, and denotes F-band (fast-band) corresponding to the blue-band PL. [21]

Since the first observation of the visible PL, alternative efforts have extensively carried out to develop a novel LED based on porous Si. As the results of the improvement employing various LED structures, such as Schottky barrier diodes [22,23] and p-*n* junction diodes [24], the emission color extends over most of the visible spectral region (including blue [25]) and the external quantum efficiency can reach about 0.2%. [26] The *nc*-Si LED technology would take advantage of a mature Si technology to combine optical and electronic components on a single substrate.

1.2. Purpose of This Work

The purpose of this thesis work is to study the visible light emission from optoelectronic Si thin films with an emphasis on a physical interest centered upon the emission mechanism. The study is composed by two parts: one is visible EL from *a*-Si:H at a high electric field (Chapter II) which is extended to the study on the high electric field effects on the carrier transport (Chapter III) [27–30], the other is PL from *nc*-Si in red-band (Chapter IV) and in blue-band (Chapter V) [31–33]. Also aimed in this thesis work is a technological application toward two dimensional matrix optoelectronic devices, especially, a high-gain photodiode utilizing the high electric field effects in a-Si:H [34] and a solid state thin film light emitting diode (TFLED) (Chapter VI) employing *nc*-Si as a light emitting active layer [31,32].

In Chapter II, we first describe visible electroluminescence (EL) from *a*-

Si:H employing the ac driven double insulating EL device structure. The EL emission has been observed at room temperature with a high electric field more than 1 MV/cm, being indicative of hot-electron-induced EL mechanism. This thesis work demonstrates the first observation of the hot-electron-induced visible light emission from *a*-Si:H. From an analysis of the EL spectrum, the hot electron properties including the mean free path and the average energy are estimated. Furthermore, the temperature dependence and the alloy-induced effects for the mean free path are discussed.

In Chapter III, we present the experimental results on the internal electric field at *a*-Si:H in the EL device structure utilizing an electroabsorption (EA) technique. The electric field saturation in a-Si:H at an electric field higher than 1 MV/cm is found and interpreted as the field distortion due to the transferred charge multiplication. On the experimental grounds involving the existence of hot-electrons evidenced in Chapter II, the transferred charge multiplication is concluded to be due to electron avalanche multiplication. From an analysis of the electric field dependence of the electron impact ionization rate, the electron mean free path are evaluated. Furthermore, the temperature dependence and the alloy-induced effects for the impact ionization rate with a comparison with the results of the EL spectrum in Chapter II.

In Chapter IV, we describe red-band photoluminescence (PL) from *nc*-Si fabricated by electrochemical anodization from microcrystalline Si (μc-Si). Red-band PL is related to the fabrication conditions including an anodizing current density, an initial thickness and crystallinity before anodization. From structural studies, in particular, an analysis of a Raman scattering spectrum performed on the *nc*-Si, the average crystallite size is evaluated. Comparing PL and Raman results, the emission mechanism with an emphasis on the relation to the quantum confinement effects is discussed.

In Chapter V, we present blue-band PL from *nc*-Si fabricated from *a*-Si:H employing solid phase growth by a rapid thermal annealing technique. Blue-band PL is discussed in relation with the annealing time and temperature. From structural studies incorporating x-ray diffraction and atomic force microscope measurements, the average crystallite size is estimated to be several tens nanometers. The differential transparent spectrum obtained by photo-induced thermoabsorption spectroscopy (TAS) is indicative of a formation of a quasi three dimensional energy

band structure in the *nc*-Si. The TAS spectrum also reveals optical transitions corresponding to PL energies.

In Chapter VI, we describe the application to an *a*-Si:H-based photodiode founded on our new results associated with the avalanche multiplication in Chapter III. We have developed an *a*-Si:H/*c*-Si heterostructure as an alternative structure of the double insulating EL device structure in order to achieve high electric field in *a*-Si:H and to extract the photogenerated carrier in *a*-Si:H to external electrodes. Next, we present development of the TFLED employing the electrochemically formed *nc*-Si described in Chapter IV as a light emitting active layer. We have observed visible light emission from the *nc*-Si based TFLED for the first time as an entirely solid state Si-based thin film light emitting devices.

In the final chapter, the main conclusions obtained through this thesis work are summarized.

References

[1] L. Esaki, *Highlights in Condensed Matter Physics and Future Prospects* (Plenum, New York, 1991).

[2] H. Fritche, *Amorphous Silicon and Related Materials, Advances in Disordered Semiconductors*, vol. 1, (World Scientific, Singapore, 1989), J.I. Pankove, *Hydrogenated Amorphous Silicon, Semiconductors and Semimetals*, vol. 21, (Academic Press, New York, 1984).

[3] E. Lueder, Mater. Rec. Soc. Symp. Proc. **377** (1995) 847.

[4] R.A. Street, X.D. Wu, R. Weisfield, S. Ready, R. Apete, M. Nguyen, and P. Nylen, Mater. Rec. Soc. Symp. Proc. **377** (1995) 757.

[5] R. Newman, W.C. Dash, R.N. Hall, and W.E. Burch, Phys. Rev. **98** (1955) 1556.

[6] A.G. Chynoweth and K.G. McKay, Phys. Rev. **102** (1956) 369.

[7] E. Kameieniecki, Phys. Stat. Sol. **6** (1964) 877.

[8] W. Shockley, Solid State Electron. **2** (1961) 35.

[9] P.A. Wolff, Phys. Rev. **95** (1954) 1415, J. Phys. Chem. Solids **16** (1960) 184.

[10] P.A. Childs, W. Eccleston, and R.A. Stuart, Electron. Lett. **17** (1981) 281.

[11] S. Tam and C. Hu, IEEE Trans. Electron Devices **31** (1984) 1264.

[12] T. Tsuchiya and S. Nakajima, IEEE Trans. Electron Devices **32** (1985) 405.

[13] A. Toriumi, M. Yoshimi, M. Iwase, Y. Akiyama, and K. Taniguchi, IEEE Trans.

Electron Devices **34** (1987) 1501.

[14] J Matsunaga and S. Kohyama, Appl. Phys. Lett. **15** (1978) 335.

[15] S.S. Iyer, R.T. Collins, and L.T. Canham, *Light Emission from Silicon* (MRS, Pittsburgh, 1992), M.A. Tischler, R.T. Collins, M.L.W. Thewalt, and G. Abstreiter (MRS, Pittsburgh, 1993), Z.C. Feng and R. Tsu, *Porous Silicon*, (World Scientific, Singapore, 1994), R.W. Collins, C.C. Tsai, M. Hirose, F. Koch and L. Brus, *Microcrystalline and Nanocrystalline Semiconductors*, (MRS, Pittsburgh, 1995).

[16] D.C. Houghton, N.L. Rowell, J.-P. Noël, G. Ares, M. Davies, A. Wang, and D.D. Perovic, Mater. Rec. Soc. Symp. Proc. **298** (1993) 3.

[17] A.G. Nassiopoulos, S. Grigoropoulos, D. Papadimitriou, and E. Gogolides, Phys. Stat. Sol. (b) **190** (1995) 91.

[18] H. Takagi, H. Ogawa, Y. Yamasaki, A. Ishizaka, and T. Nakagiri, Appl. Phys. Lett. **56** (1990) 2379.

[19] L.T. Canham, Appl. Phys. Lett. **57** (1990) 1046.

[20] V. Lehmann and U. Gösele, Appl. Phys. Lett, **58** (1991) 856.

[21] L.T. Canham, Phys. Stat. Sol. (b) **190** (1995) 9.

[22] A. Richter, P. Steiner, F. Kozlowski, and W. Lang, IEEE Elect. Device Lett. **12** (1991) 691.

[23] N. Koshida and H. Koyama, Appl. Phys. Lett. **60** (1992) 347.

[24] Z. Chen, G. Bosman, and R. Ochoa, Appl. Phys. Lett. **62**, 708 (1993).

[25] P. Steiner, F. Kozlowski, M. Wielunski, and W. Lang, Jpn. J. Appl. Phys. **33** (1994) 6075.

[26] J. Linnros and N. Lalic, Appl. Phys. Lett. **66** (1995) 3048.

[27] T. Toyama, K. Hiratsuka, H. Okamoto, and Y. Hamakawa, J. Appl. Phys. **77** (1995) 6354.

[28] T. Toyama, K. Hiratsuka, H. Okamoto, and Y. Hamakawa, J. Non-Cryst. Solids **198–200** (1996) 198.

[29] T. Toyama, T. Matsui, K. Hiratsuka, H. Okamoto, and Y. Hamakawa, Jpn. J. Appl. Phys. **35** (1996) (in press).

[30] T. Toyama, T. Matsui, H. Okamoto, and Y. Hamakawa, Appl. Surf. Sci. (in press).

[31] T. Toyama, T. Matsui, Y. Kurokawa, H. Okamoto and Y. Hamakawa, Appl. Phys. Lett. **69** (1996) 1261.

[32] T. Toyama, T. Matsui, T. Yamamoto, and H. Okamoto, Mater. Res. Soc. Symp. Proc. **452** (1997) (to be published).

[33] T. Toyama, T. Ouchida, H. Okamoto, and Y. Hamakawa, Appl. Surf. Sci. (in press).

[34] K. Ishida, S. Nakamura, T. Toyama, H. Okamoto, and Y. Hamakawa, Appl. Surf. Sci. (in press).

Chapter II

Hot-Electron-Induced Electroluminescence from Hydrogenated Amorphous Silicon

2.1. Introduction

In the next two chapters, we shall introduce to the study on the optical and electrical properties of hydrogenated amorphous silicon (*a*-Si:H) at high electric field above 1 MV/cm. We describe hot-electron-induced visible electroluminescent (EL) phenomena in Chapter II and electron avalanche multiplication in Chapter III. We note that these phenomena have never observed in *a*-Si:H with certain grounds before our experimental results. [1–4] We believed that the study on the *a*-Si:H properties at the high electric fields open up novel *a*-Si:H-based optoelectronic devices, in particular, a fast high-gain photodiode as an application of the avalanche multiplication.

In recent years, there have appeared several reports concerning "high-gain" photodiodes based on *a*-Si:H, in which the gain determined by the ratio from input light photon flux to output photocurrent exceeds unity upon deeply biased in the reverse direction. [5–8] The *a*-Si:H/*a*-SiN:H heterostructure photodiode in one of the earliest study [5] exhibits large gain of 10, whereas the time response is quite slow of the order milli-seconds. The photocurrent multiplication is interpreted as an alternative mechanism rather than the avalanche multiplication, that is, the interband tunneling injection process. Then the photodiode based on the avalanche multiplication mechanism has been believed to be the most promised candidate to

achieve simultaneously both high gain and fast response.

The other studies [6–8] have dealt with the photocurrent multiplication as the avalanche multiplication, although any firm ground has not been given for the avalanche multiplication mechanism, except for only few phenomenological grounds: dependence on a wavelength of incident light, [7] linearity between input-light and output-current. [8] In these previous studies the photocurrent characteristics has been performed at the electric fields on the order of 10^5 V/cm, since the dark current tends to grow sharply above the electric fields. [6–8] By contrast, as the results of steady-state photocurrent measurements [9] or time-of-flight (TOF) measurements, [10] no current increase has been observed until electric field of 5×10^5 V/cm.

A fundamental question then arises whether carriers become sufficient "hot" to induce impact ionization required for avalanche multiplication at the electric fields at the level of 10^5 V/cm in *a*-Si:H. Hot-electrons have been dynamically observed in *a*-Si:H in the femtosecond optical studies. [11,12] The optical absorption spectrum for the high energy photons of ~6 eV implies the existence of the photon-induced hot-carriers. [13] Regarding the electric-field-induced hot-carriers, Juska *et al.* have carried out the TOF measurements in associated with dependence of drift mobility on both electric fields and measurement temperatures. They have suggested that electrons are likely to become hot with an energy of 0.14 eV at electric field of 5×10^5 V/cm, whereas any carrier multiplication has not been observed in their experiments [10]. Therefore there has been no excellent experimental technique monitoring current in *a*-Si:H to reveal clearly the existence of the electric-field-induced hot-carrier.

With respect to crystalline semiconductors, hot-carriers has been directly observed since the 1950's [14] as EL emission under high electric field and the EL emission is one of the precursor for avalanche multiplication. For crystalline Si (*c*-Si), hot-carrier-induced EL emission has been observed from several devices such as deeply reverse-biased *p-n* junction diodes [14] or metal-oxide-semiconductor field-effect-transistors (MOSFETs). [15–17] For wide band-gap II-VI compound semiconductors represented by ZnS, it is well known that the visible hot-electron-induced EL emission has been observed employing the double insulating EL devices and applied to flat panel displays for the last 20 years. [18] The EL device structure is quite simple consisting basically of an insulator/a light

active layer/an insulator, so that various materials have applied to the light active layer. We have already applied wide energy gap amorphous semiconductors (i.e. hydrogenated amorphous silicon carbide alloys (*a*-SiC:H) and hydrogenated amorphous carbon (*a*-C:H)) seeking for the application to the displays [19–21] or light-converters. [22] We have achieved the visible EL emission, although the photoluminescence-(PL)-emission-like radiative recombination is suggested for the emission mechanism.

In this chapter, EL emission characteristics is described employing the EL device structure. From the EL emission features, the emission mechanism is discussed from the temperature and electric field dependence. Furthermore, discussion on the electron energy distribution, which should reflect the EL spectrum, reveals the electron mean free path.

2.2. Experimental Details

2.2.1. Sample Preparation

The double insulating EL devices, the structure shown in Fig. 2.1 was fabricated on a glass substrate coated by stacked transparent conductive oxide (TCO) films: indium tin oxide (ITO) and SnO_2 films. Amorphous layers in the EL devices were deposited by a cross-field plasma chemical vapor deposition (CVD) method employing the apparatus displayed in Fig. 2.2. The deposition conditions for *a*-Si:H as summarized in Table. 2.1 were given by those in the optoelectronic devices such as solar cells [23] or photosensors [5]. Also summarized in Table 2.1, the deposition conditions for insulating near-stoichiometric *a*-SiN:H layers deposited from a mixture of SiH_4 and NH_3 gasses were determined according to those in *a*-C:H-based blue light emitting EL devices. [19–21] Source gasses of SiH_4 and NH_3 were diluted in H_2, the parts of the volume of SiH_4 and NH_3 were

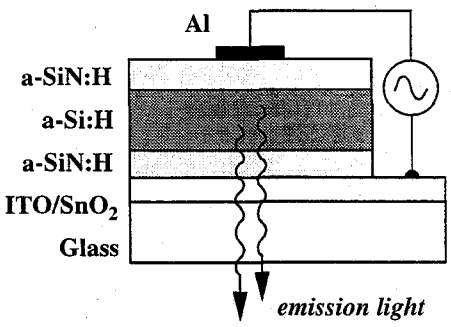

Fig. 2.1. Cross-sectional view of an ac-driven double insulating EL device.

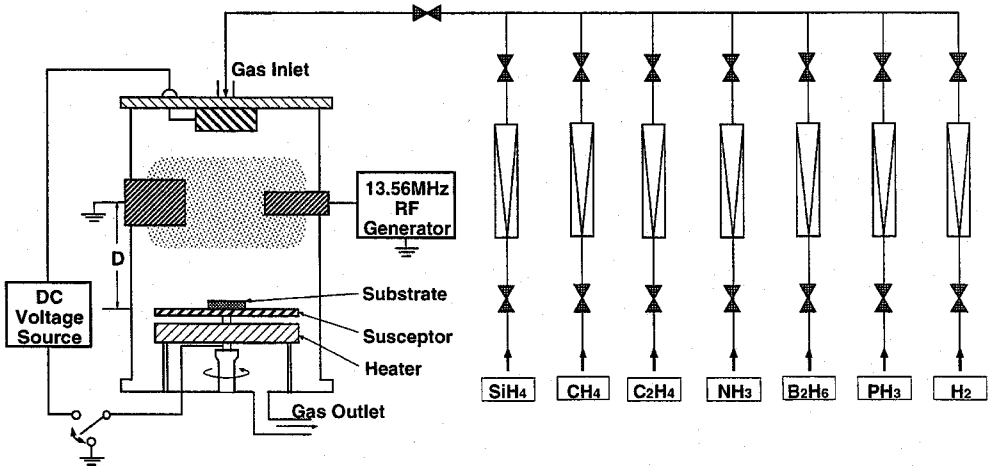

Fig. 2.2. Schematic diagram of plasma CVD apparatus. All of the Si thin films including amorphous or microcrystalline Si thin films elucidated in this thesis were fabricated employing this system. The source gases were diluted by H_2 into 10%.

Table 2.1. Deposition conditions of plasma CVD for *a*-Si:H and *a*-SiN:H.

	a-Si:H	*a*-SiN:H
Substrate Temperature	**180°C**	
Pressure	**133 Pa (1.0 Torr)**	
r.f. Power	**45 W**	
SiH_4 Gas Flow Rate	**20 sccm**	**5 sccm**
NH_3 Gas Flow Rate		**70 sccm**
Thickness	**100–500 nm**	

10%. The aluminum top electrode with an area of 0.033 cm^2 was evaporated at room temperature. The dielectric constants of *a*-Si:H and *a*-SiN:H were estimated to be about 12 and 6, respectively, from the measurements of capacitance of the EL devices with changing the thicknesses of the *a*-Si:H layer.

2.2.2. *EL Characterization*

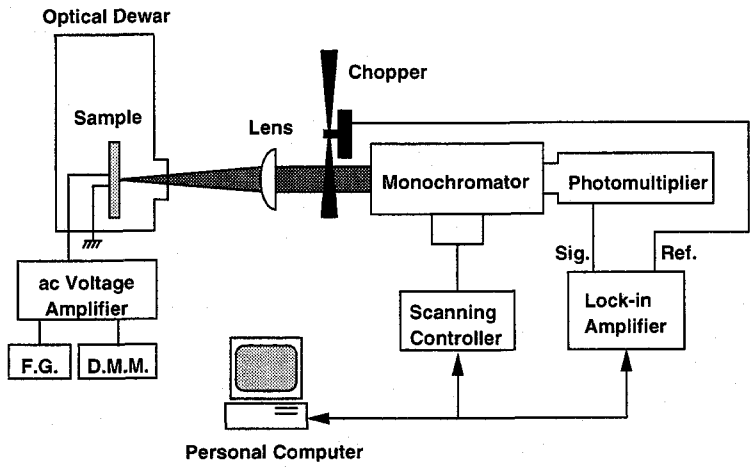

Fig. 2.3. Illustration of EL spectrum measurement apparatus. The EL emission was mechanically chopped with a frequency of about 820 Hz and its monochromated light was monitored by the cooled photomultiplier and the conventional lock-in amplifier system.

The EL devices were operated by a sinusoidal ac voltage at a frequency of 5 kHz. In this article, both an applied voltage and an electric field are represented by the values at zero-to-peak, namely the maximum height of the wave.

The integrated EL intensity was monitored by a cooled GaAs(Cs) photomultiplier (Hamamatsu Photonics R943-02) and a picoammeter (HP 4140B), thus the EL intensity is limited for the spectral region from 300 nm to 850 nm by the photomultiplier.

The EL spectrum measured by the conventional apparatus as illustrated in Fig 2.3. The EL devices were set in the optical dewar for the control of the measurement temperature ranging from 100 K to 400 K. The emission light was dispersed by a 20-cm monochromator (Jobin Yvon H-20IR) with 600-lines/mm 500-nm brazed grating. The detected signal of the dispersed light by the cooled GaAs(Cs) photomultiplier was amplified by a current amplifier and monitored by a double phase lock-in amplifier (NF Circuit Block 5610B), reference frequency

of which given by a mechanical chopper was about 820 Hz. The measured spectra were corrected for the wavelength dependence of the optical system as well as the optical absorption in *a*-Si:H.

2.3. Electroluminescence at High Electric Field

2.3.1 Experimental Results

The typical EL intensity characteristics at room temperature are plotted against applied voltage with changing of *a*-Si:H thicknesses as shown in Fig. 2.4. As with the *a*-C:H-based EL devices, the EL emission becomes detectable abruptly above the threshold voltage of 150 V at any *a*-Si:H thickness. At the threshold voltage, the electric field in *a*-Si:H measured by an electroabsorption (EA) method reaches about 1 MV/cm. [1,2] The detail interpretation associated with the electric field in terms of the EA method is discussed in Chapter III. The result of EL intensity characteristics indicates two features being different from interband photo emission

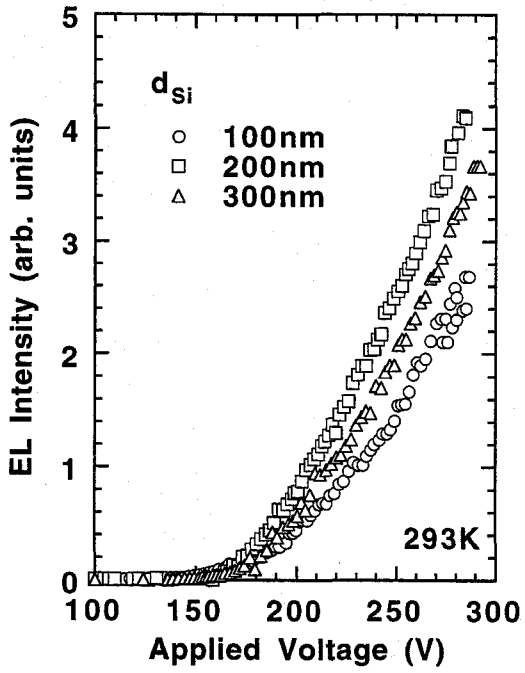

Fig. 2.4. EL intensity – applied voltage characteristics at room temperature as a function of *a*-Si:H thickness (d_{Si}). [d_{Si}: 100 nm, ○ ; 200 nm, □ ; 300 nm, △].

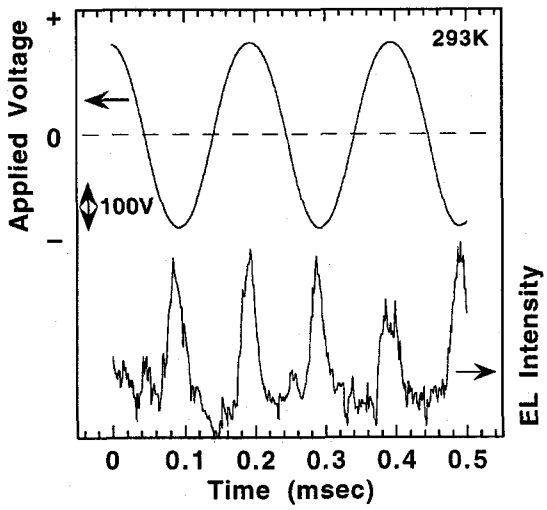

Fig. 2.5. Time response of applied voltage and EL intensity. The positive applied voltage represents the positive voltage applied on the Al electrode of the EL device.

features of *a*-Si:H as observed in PL emission [24] or EL emission due to injection current in a *p-i-n* diode [25]:

i) The EL emission is detectable even at room temperature under a high electric field about 1 MV/cm.

ii) Considering the measurable spectral range of the EL intensity, the EL emission has a spectral component being shorter than a wavelength of 850 nm.

On the first term the occurrence of the EL emission only at an electric field above the threshold voltage was clarified in Fig. 2.5 which compares the applied voltage with the EL emission in time domain.

The second term is confirmed in the EL spectra as displayed in Fig. 2.6 measured at different the applied voltages with changing thicknesses of *a*-Si:H to be 200 nm (Fig. 2.6(a)) and 400 nm (Fig. 2.6(b)). The measured EL intensity was converted to the number of emission photons per unit energy, n_{ph}, after division by the photon energy at every wavelength. The broad-band spectra decay near-exponential even above the optical energy gap E_o of 1.79 eV derived from Tauc's plots. [26] Since they include almost the whole visible region, the light emission is detected by the naked eye, although it is fairly weak being necessary for the observer's patient. The oscillation superposed on the near-exponential spectral decay is to be due to the optical interference which is confirmed by the dependence of the oscillation period on the *a*-Si:H thicknesses.

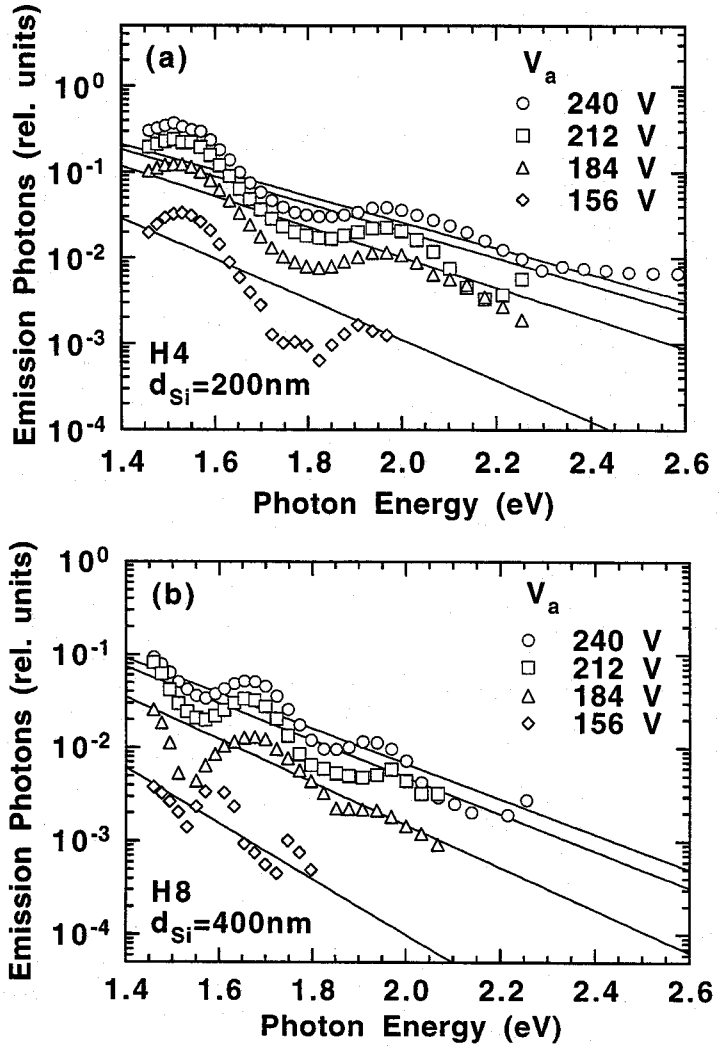

Fig. 2.6. Spectra of emission photon number per unit energy (n_{ph}) at different applied voltages (V_a) [V_a: 240 V, ○; 212 V, □; 184 V, △; 156 V ◇]. The *a*-Si:H thicknesses (d_{Si}) are 200 nm (a) and 400 nm (b). Solid lines are fitting lines calculated from the electron distribution function of Eq. (2.1). [$\hbar\omega = 50$ meV; $\lambda = 1.0$ nm.] The fitting requires the value of the internal field of *a*-Si:H which is obtained by Fig. 3.3.

2.3.2 *EL Emission Mechanism*

The results in Figs. 2.4–2.6 imply that the mechanism for the EL emission is different from the interband recombination like PL emission. Alternatively, intraband transition in conduction bands of electrons is the most likely emission mechanism in *a*-Si:H. Let us enumerate the reasons:

i) Radiative electron-hole recombination like PL emission is almost impossible. It has been reported that PL emission is almost completely quenched due to thermal activation of the generated electron-hole pare at room temperature even without applying any electric field, and that is also quenched due to electrical activation above an electric field of 10^5 V/cm even at low temperature. [27–28]

ii) Intraband electron transition process in conduction bands is proposed in experimental [14–17] and theoretical [29–31] studies about EL emission from *c*-Si employing a reversely biased *p-n* diode or a MOSFET in which electric field of *c*-Si exceeds 10^5 V/cm. The EL emission from *c*-Si is observed at room temperature with a spectrum decaying near-exponentially from energy gap of 1.1 eV to around 3.0 eV.

Therefore, in the following discussion, we consider that intraband transition dominates the EL emission in *a*-Si:H at higher electric field than 1 MV/cm.

2.4. Mean Free Path

2.4.1. *Evaluation from EL Spectrum*

In the case of intraband transition, the decay of the luminescence spectra in Fig. 2.6 should reflect the electron energy distribution. According to the lucky-drift model [32–35] in which parabolic bands and energy-independent mean free path are assumed, the number of electrons per unit energy $n(E)$, which is normalized by the total number of electrons, is approximately expressed by [35]

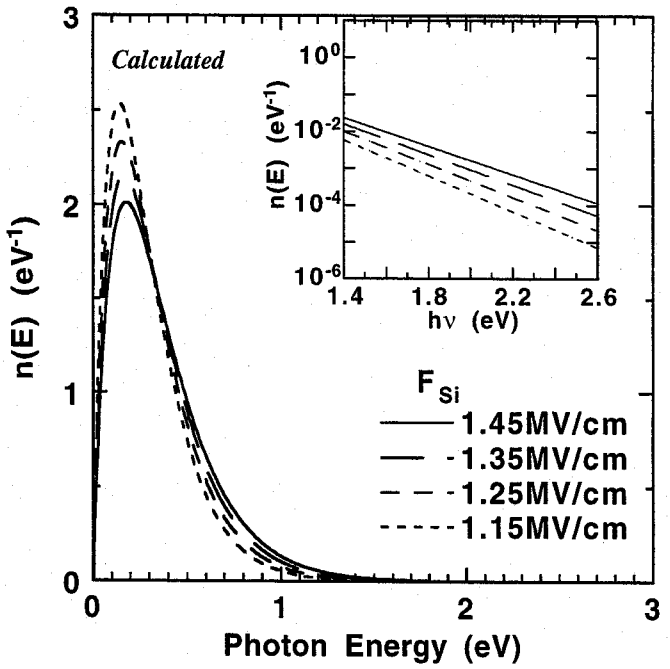

Fig. 2.7. The electron energy distribution $n(E)$ calculated from Eqs. (2.1) and (2.2) as a function of the electric field in a-Si:H from 1.15 MV/cm to 1.45 MV/cm. Inset shows the logarithmic plot of $n(E)$ at the spectral region of the measured EL spectrum.

$$n(E) = \frac{f(E) \cdot N(E)}{\int_{E_c}^{0} f(E) \cdot N(E) dE}$$

$$= \frac{\exp(-E / eF_{Si}\lambda_E) - \exp(-E / eF_{Si}\lambda)}{eF_{Si}(\lambda_E - \lambda)}, \qquad (2.1)$$

where $f(E)$ denotes the electron distribution, $N(E)$ the density of states in the conduction band, E the electron energy, F_{Si} the internal electric field in a-Si:H, e the electronic charge, λ_E the energy relaxation length and λ the mean free path (or the momentum relaxation length; assuming λ is energy-independent in this model). λ_E is given by

$$\lambda_E = \frac{eF_{Si}\lambda^2}{2\hbar\omega}\coth\left(\frac{\hbar\omega}{2k_BT}\right), \tag{2.2}$$

where $\hbar\omega$ denotes the optical phonon energy, k_B the Boltzman constant and T the lattice temperature. Figure 2.7 exhibits a calculated result of the electron energy distribution $n(E)$ employing Eqs. (2.1) and (2.2) as a function of the electric field in *a*-Si:H. The inset of Fig. 2.7 is the logarithmic plot of $n(E)$ at the energetic region for the measured EL spectra. It is clearly found that the electron energy distribution decays almost exponentially. In this high energies, the electron energy distribution $n(E)$ is approximately expressed by

$$n(E) \approx \exp\left(-E / eF_{Si}\lambda_E\right). \tag{2.3}$$

Therefore, the EL spectrum decays more steeply with decreasing in F_{Si} or λ or with increasing the measurement temperature.

The solid lines in Fig. 2.6 are plotted in accordance with Eq. (2.1), in which the mean free path of 1.0 nm is used as the fitting parameter for the spectra at electric fields ranging from 1.0 MV/cm to 1.5 MV/cm. The optical phonon energy of 50 meV is given for the fitting because 50 meV is used as the optical phonon energy of *c*-Si [33] and the mean value of the longitudinal optical (LO) phonon energy of 38 meV and the transverse optical (TO) phonon energy of 60 meV which are revealed by Raman scattering measurements. [36] These parameters lead to an approximate average energy $E_{avg} = eF_{Si}\lambda_E$ of 0.13 eV at a threshold field of the light emission F_{Si} = 1.0 MV/cm.

For amorphous semiconductors, the carrier mean free path near the band edge, namely, the mean free path corresponding to the low electric field carrier transport, has been believed to be very close to the averaged atomic spacing; i.e. around 0.23 nm for *a*-Si:H and its alloys. However, the magnitude on the order of 1 nm has been proven to be still consistent with well-known experimental observations on optical and transport properties including "famous" anomalous Hall sign (for example, Mott [37], Okamoto *et al.* [38] & Tsutsumi *et al.* [39]).

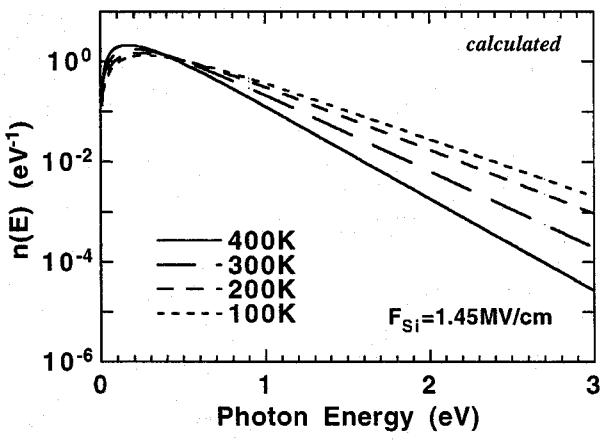

Fig. 2.8. The calculated electron energy distribution $n(E)$ as a function of the temperature ranging from 100 K to 400 K.

The elastic scattering mean free path is basically determined by the product of the velocity of carriers and the scattering time. The latter is proportional to the inverse of the density-of-states at the specific energy, that is, the velocity of carriers (if the quadratic E - **k** dispersion is assumed for the unperturbed reference system), so that the carrier mean free path might have no appreciable "energy dependence" for above-mobility-edge states, being around 1 nm even for high energy carriers. This kind of argument has been made in detail by Economou *et al.* [40], Yonezawa *et al.* [41] and Hattori *et al.* [42] within the context of the tight-binding coherent potential approximation.

Juska *et al.* [10] has lead the similar magnitude of the carrier mean free path for *a*-Si:H from the analysis of "high-field" time-of-flight measurements, and claimed that the absence of avalanche multiplication at the electric fields less than 0.5 MV/cm is due to such a small high energy carrier mean free path as well as the effect of inelastic (phonon) scattering.

We therefore believe that the magnitude of the carrier mean free path at high fields, around 1 nm, concluded in this work does not contradict with any current understanding of charge carrier transport in amorphous semiconductors from the theoretical and experimental points of view.

The lucky-drift model leads to the momentum relaxation time, $\tau_m(E)$, the

energy momentum relaxation time, $\tau_E(E)$, and the saturation drift velocity, v_{ds}, in the following equations: [32–34]

$$\tau_m(E) = \sqrt{\frac{m^*}{2E}}\lambda, \tag{2.4}$$

$$\tau_E(E) = \frac{E}{\hbar\omega}\coth\left(\frac{\hbar\omega}{2k_BT}\right)\cdot\tau_m(E), \tag{2.5}$$

$$v_{ds} = \frac{eF\tau_m(E_{avg})}{m^*} = \sqrt{\frac{\hbar\omega}{m^*}\tanh\left(\frac{\hbar\omega}{2k_BT}\right)}, \tag{2.6}$$

where m^* is the effective mass of electron (= 0.3 m_0). [43] At the average energy $E_{avg.}$ = 0.13 eV (F_{Si} = 1 MV/cm), $\tau_m = 2 \times 10^{-15}$ sec, $\tau_E = 9 \times 10^{-15}$ sec and $v_{ds} = 1.5 \times 10^7$ cm/sec are evaluated. The saturation drift velocity, v_{ds}, of *a*-Si:H is close to that of *c*-Si although almost the one order of magnitude larger field is necessary to saturate the electron velocity.

2.4.2. *Temperature Dependence*

As found from Eq. (2.3), the decay line of the EL spectrum changes as a function of the measurement temperatures. Figure 2.8 shows a calculated result for the electron distribution function $n(E)$ varying the temperature from 100 K to 400 K. The exponential decay is monotonously flattened with an increase in the temperature.

The EL spectrum has been measured at different temperatures ranging in 133–385 K as shown in Fig. 2.9. The EL spectra were measured at an applied voltage fixed to be 130 V which corresponds to the internal electric field in *a*-Si:H of 1.4–1.5 MV/cm (the electric field increases gradually with an increase in the temperature). The exponential decay of the EL spectrum changes with increasing the temperature, however, the change of the decay is not monotonous as shown in

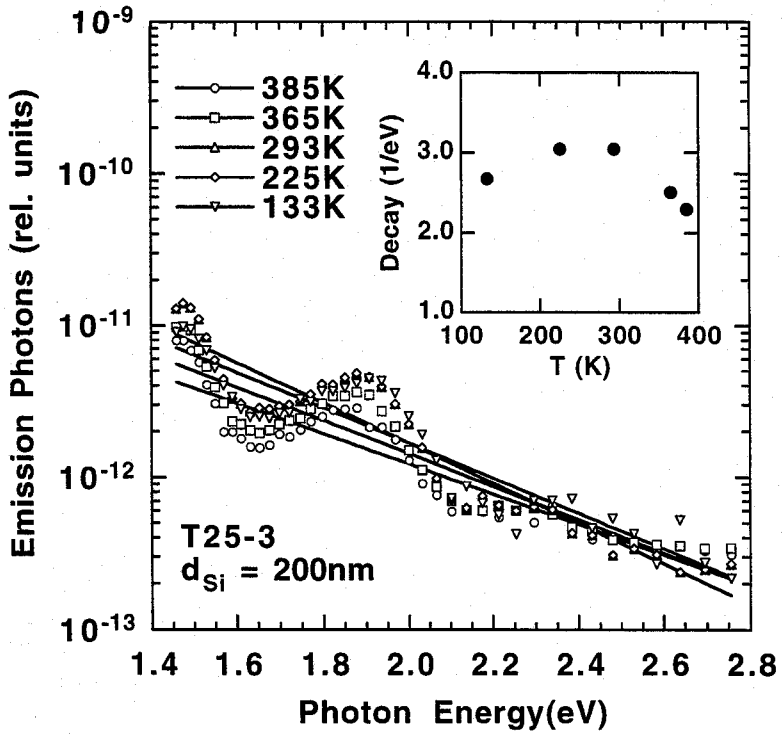

Fig. 2.9. Temperature dependence of the EL spectrum at different temperatures (T) [T: 385 K, ○; 365 K, □; 293 K, △; 225 K ◇; 133 K, ▽]. The EL spectra were measured at a applied voltage fixed to be 130 V which corresponds to the internal electric field in a-Si:H of 1.4–1.5 MV/cm. Inset shows the decay of the EL spectra plotted against the measurement temperatures.

the inset of Fig. 2.9.

In Fig. 2.10, the electron mean free paths deduced from the decay of the EL spectra according to Eq. (2.3) are plotted against the measurement temperatures, T, at different thicknesses of a-Si:H, d_{Si}, and different internal electric fields of a-Si:H, F_{Si}, (the applied voltage was fixed to be 130 V). The mean free paths are independent of the thicknesses and the internal electric fields of a-Si:H, which is consistent of the results shown in Fig. 2.6. In the lower temperatures from 130 K to 300 K, the mean free paths decrease with an increase in the measurement temperatures. The dashed line is a calculated line for the temperature dependence

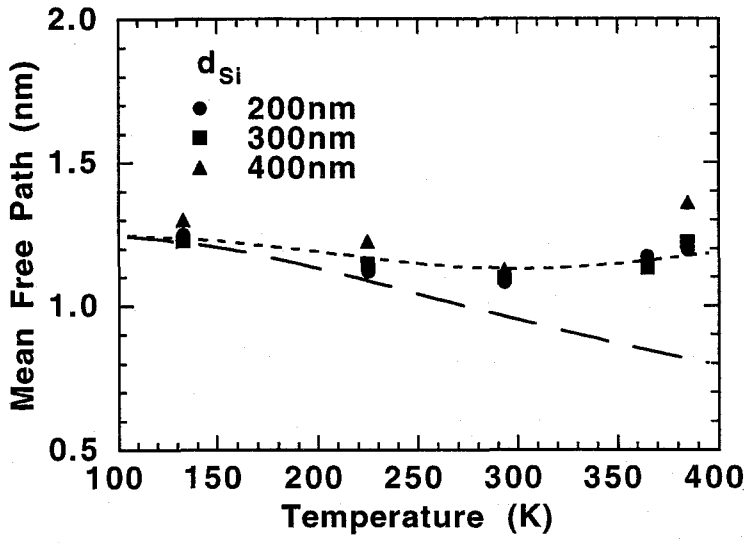

Fig. 2.10. The temperature dependence of the mean free path obtained from the decay of the EL spectra in Fig. 2.9 employing Eq. (2.3). The mean free paths are measured at the different thicknesses of *a*-Si (d_{Si}) and the internal electric fields at *a*-Si:H (F_{Si}) [d_{Si}: 200 nm, F_{Si}: 1.4–1.5 MV/cm, ●; d_{Si}: 300 nm, F_{Si}: 1.3–1.4 MV/cm, ■; d_{Si}: 400 nm, F_{Si}: 1.2–1.3 MV/cm, ▲]. The dashed line is calculated by Eq. (2.7) which is based on the optical phonon scattering. The dotted line is in accordance with the modified model given by Eq. (2.15) including the effect on the structural disorder [$T_0 \approx 28$ K, $a \approx 0.00001$ in Eq. (2.13)].

of the mean free path (we shall now denote λ as λ_p) in a crystalline semiconductor based on the optical-phonon scattering: [33]

$$\lambda_p = \lambda_{p0} \tanh\left(\frac{\hbar\omega}{2k_B T}\right), \tag{2.7}$$

where λ_{p0} is the mean free path at 0 K. The calculated line would explain the decrease in the experimental data on the mean free path. This implies that in the low temperatures the optical phonon scattering would dominate the mean free

path in *a*-Si:H as well as that in crystalline semiconductors.

On the contrary, elevating the temperature up to 400 K, the mean free paths turn to rise. This cannot be explained by the model based on the optical phonon scattering. Let us now modify the carrier transport model including effects of disorder in amorphous materials. According to Economou *et al.*, the conductivity can be written as [40]

$$\sigma = \int dE\, \sigma(E)\left(-\frac{df(E)}{dE}\right) = \int dE\, e\mu(E)N(E)f(E), \tag{2.9}$$

where σ(E) is the energy-dependent conductivity. The microscopic mobility of electrons in states of energy E, $\mu(E)$, is expressed as

$$\mu(E) = \frac{1}{eN(E)}\frac{d\sigma(E)}{dE}. \tag{2.10}$$

Considering the potential fluctuation due to the disorder, we shall define the conductivity near the mobility edge as

$$\sigma(E) \equiv \frac{1}{\pi^3}\frac{e^2}{\hbar}\frac{1}{\Lambda}g, \tag{2.11}$$

where Λ is the mean free path in terms of the disorder. The dimensionless conductance, g, is given by the solution of the following equations:

$$g(C,U)\left[g(C,U) - U + 1\right]^2 = C \cdot U, \tag{2.12a}$$

$$U = E/E_c, \tag{2.12b}$$

$$C = \left(\Lambda/L_i\right)^2, \tag{2.12c}$$

where E_c denotes the mobility edge (≈ 0.1 eV for a-Si:H). Since the average energy of the hot electrons in a-Si:H has estimated to be ~0.13 eV, U is to be almost unity. Let us now approximate the coherence length (or inelastic diffusion length), L_i, at high temperatures as [44]

$$L_i \propto T^{-3} \approx \frac{\Lambda}{\sqrt{1+a\exp(T/T_0)}} \quad (T > 300K), \tag{2.13}$$

where T_0 is the characteristic temperature, and a is the constant.

Furthermore we shall express the observed mean free path, λ_{obs}, as

$$\lambda_{obs}^2 = \frac{2}{e} E\mu(E)\tau_m . \tag{2.14}$$

Employing Eqs. (2.5), (2.11)–(2.14), and assuming the parabolic band, i.e. $N(E) \propto \sqrt{E}$, we finally find

$$\lambda_{obs}^2 \propto \frac{\partial\sigma(E)}{\partial E}\left(\sqrt{E}\cdot\tau_m\right) \propto \frac{\partial\sigma(E)}{\partial E}\lambda_p . \tag{2.15}$$

In Fig. 2.10, the dotted line is the calculated mean free path given by Eq. (2.15). The good agreement between the experimental and the theoretical results implies that the structural disorder in a-Si:H might affect even on the high electric field carrier transport.

2.4.3. Alloy-Induced Effect in a-SiC:H

Substituting a-SiC:H for a-Si:H in the EL device, the hot-electron-induced EL emission has been also observed in a-SiC:H deposited from a mixture of SiH_4 and CH_4 gasses. [3–4] The carbon concentration in a-SiC:H was systematically changed by changing the deposition conditions, i.e. the substrate temperature and the source gas ratio as summarized in Table 2.2. The optical energy gaps obtained

Table 2.2. Substrate temperatures (T_{sub}) , source gas flow ratio ([CH_4] / ([SiH_4] + [CH_4])), and optical energy gap (E_o) of *a*-SiC:H.

T_{sub} (°C)	$\frac{CH_4}{SiH_4 + CH_4}$ (%)	E_o (eV)
280	66.7	1.93
280	83.3	2.04
280	91.7	2.42
180	66.7	2.00
180	83.3	2.13
180	91.7	2.29

from Tauc's plot increases due to an increase in the carbon content which is roughly estimated to be 10–30 at.%. [45]

Figure 2.11 shows the EL emission spectra from *a*-SiC:H layers with different optical energy gaps measured at room temperature with changing the applied voltages V_a. The optical energy gap E_o of *a*-SiC:H in Fig. 2.11(a) is 1.93 eV and that in Fig. 2.11(b) is 2.42 eV. The electric fields are ranging in 1.4–1.6 MV/cm (Fig. 2.11(a)), 1.9–2.3 MV/cm (Fig. 2.11(b)), respectively. The interference fringes superposed on the spectra become smaller with decreasing the difference of the refractive indices between *a*-SiC:H and *a*-SiN:H.

The equal experimental features are found in the EL emission on *a*-SiC:H as found the emission on *a*-Si:H. The EL emission is observed at room temperature and high electric field above 1.4 MV/cm at which PL emission is almost quenched. The broadband spectra show near exponential curves tailing into the energies above the optical energy gap of the *a*-SiC:H layer. Therefore, the features lead us the same EL emission mechanism for *a*-SiC:H as that for *a*-Si:H, i.e. the hot-electron-induced intraband transitions.

The solid lines in Fig. 2.11 are plotted in accordance with Eqs. (2.1) and (2.2), in which the electron mean free paths and the optical phonon are used as the fitting parameters for the EL spectra as enumerated in Table 2.2. The optical phonon energy might be reduced for *a*-SiC:H with carbon content exceeding over 20 at.%

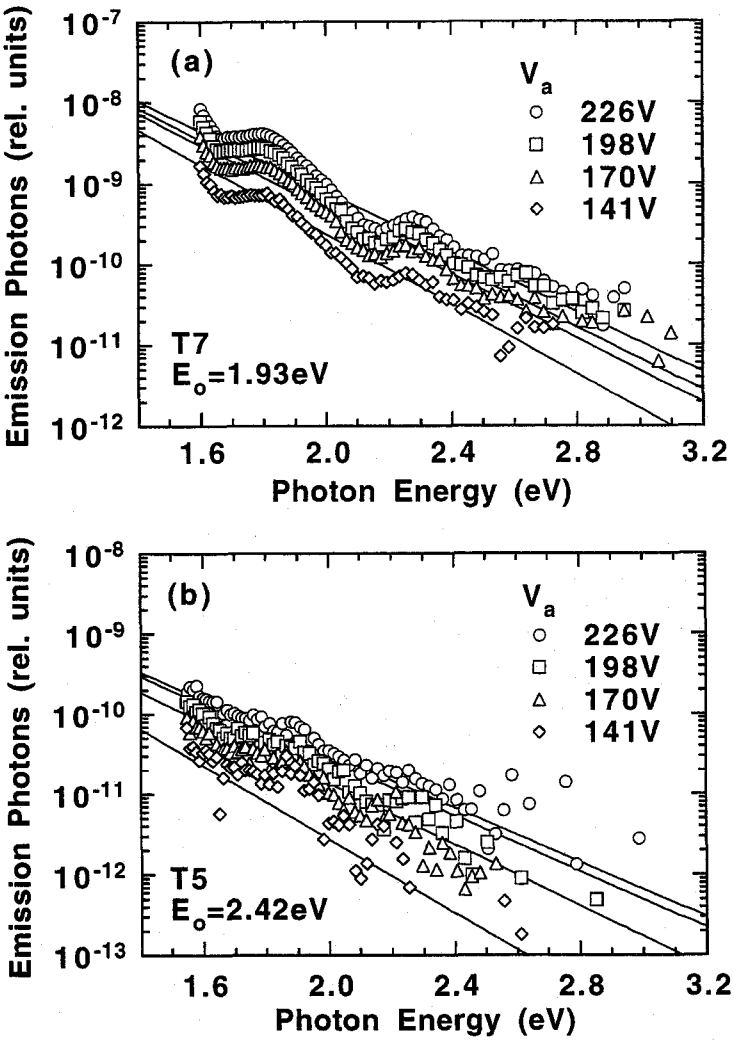

Fig. 2.11. Spectra of emission photon number per unit energy (n_{ph}) at various applied voltages (V_a) [V_a: 226 V, ○; 198 V, □; 170 V, △; 141 V, ◇]. The optical energy gaps of *a*-SiC:H (E_o) are 1.93 eV (a) and 2.42 eV (b). Solid lines are fitted lines calculated from the electron distribution function of Eq. (2.1) [$\lambda = 0.85$ nm, (a); $\lambda = 0.56$ nm, (b)].

due to the relaxation of local strain, which is exhibited as broadening of the TO phonon band and the increase of the LO phonon band in Raman scattering spectra. [46] Therefore for two samples with E_o = 2.29 eV and E_o = 2.42 eV, in which carbon content is estimated to exceed 20 at.%, the optical phonon energies were

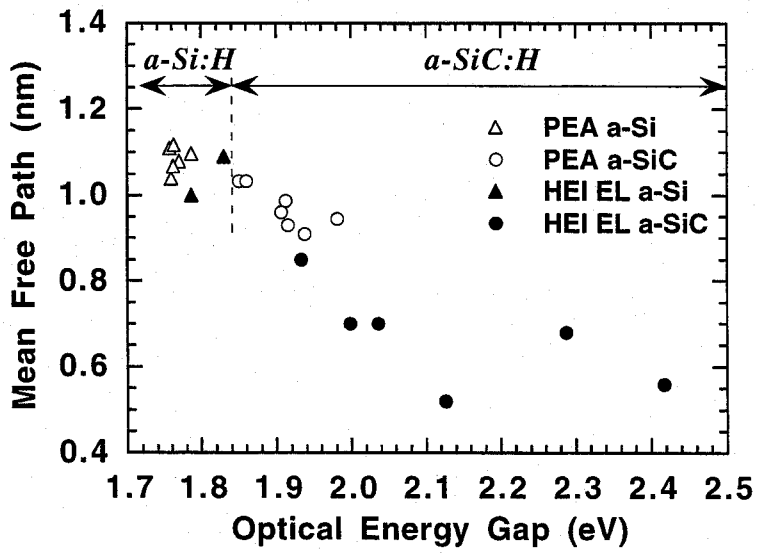

Fig. 2.12. Electron mean free paths in *a*-SiC:H (●) and a-Si:H(▲) plotted against optical energy gap estimated from the decay of EL spectra. Optical energy gap is changed by changing the fabrication conditions of *a*-SiC:H; the source gas ratio and substrate temperature. Open symbols are the electron mean free paths at low electric fields derived from the polarized EA measurements in ref. 39 [a-SiC:H, ○; a-Si:H, △].

assumed as 45 meV, while for the rest samples with the lower optical energy gaps than 2.2 eV, the optical phonon energies of 50 meV, the same value as *a*-Si:H, are adopted.

The electron mean free paths estimated from the fits to the EL spectra according to Eqs. (2.1) and (2.2) are plotted against the optical energy gaps of *a*-SiC:H in Fig. 2.12. The closed triangle symbols represent the mean free path of *a*-Si:H estimated in Figs. 2.6 and 2.10. The mean free path tends to decrease with an increase in the optical energy gap, while it depends rather weakly on the substrate temperatures. The reduction of the mean free path with an increase in the optical energy gap is in good agreement with the experimental results on the polarized EA measurement. The polarized EA measurement has been carried out at lower electric fields of ~10^4 V/cm, so that senses the effect of structural disorder at the band

edge states. [39] The similar trend of the mean free path observed in both experiments is likely to indicate that the effect of alloy-induced structural disorder extends over electron states far away from the mobility edge.

2.5. Conclusions

I. High electric field EL emission in *a*-Si:H has been investigated employing ac-driven double insulating EL devices at various thicknesses of *a*-Si:H ranging from 100 nm to 500 nm. EL emission involving a spectral component above the optical energy gap has been observed at the internal electric field in *a*-Si:H over 1 MV/cm.

II. On two grounds: i) the observed conditions for EL emission including the electric field more than 1 MV/cm and the room temperature, ii) exponential spectral shape tailing into energies higher than the optical energy gap of *a*-Si:H, the intraband transitions of the hot-electrons in the conduction bands are most likely mechanism for the EL emission at the high electric fields.

III. The hot-electron-induced EL spectrum reflects the electron energy distribution. The lucky-drift model leads to the estimated mean free path of 1.0 nm and the average electron energy of 0.13 eV at the electric field in *a*-Si:H of 1 MV/cm, respectively. The estimated values are consistent with the expected values from the experiments at the electric fields within 0.5 MV/cm.

IV. The temperature dependence of the mean free path deduced from the exponential decay of the EL spectrum has been presented. With an increase in the temperature from 130 K to 300 K, the mean free path decreases gradually in accordance with the theoretical line based on the optical phonon scattering process. In contrast, the mean free path turns to rise in the higher temperatures up to 400 K. This result implies the influence of the structural disorder to the carrier transport even at the high electric fields.

V. The visible EL emission at the high electric field has been observed from *a*-$Si_{1-x}C_x$:H ($x < 0.3$) alloys as well as a-Si:H. Since the EL emission exhibits the identical features with the EL emission from *a*-Si:H, the EL emission in *a*-SiC:H would be induced by hot-electrons.

VI. The mean free paths of *a*-SiC:H evaluated from the EL spectra tend to decrease with increasing the optical energy gaps as evaluated from the polarized EA results at low electric fields. This implies that the effect of alloy-induced structural disorder extends over electron states far away from the mobility edge.

References

[1] T. Toyama, K. Hiratsuka, H. Okamoto, and Y. Hamakawa, J. Appl. Phys. **77** (1995) 6354.

[2] T. Toyama, K. Hiratsuka, H. Okamoto, and Y. Hamakawa, J. Non-Cryst. Solids **198–200** (1996) 198.

[3] T. Toyama, T. Matsui, K. Hiratsuka, H. Okamoto, and Y. Hamakawa, Jpn. J. Appl. Phys. **35** (1996) 5975.

[4] T. Toyama, T. Matsui, H. Okamoto, and Y. Hamakawa, Appl. Surf. Sci. (in press).

[5] M. Yoshimi, T. Ishiko, K. Hattori, H. Okamoto, and Y. Hamakawa, J. Appl. Phys. **72** (1992) 3186.

[6] S.C. Jwo, M.T. Wu, Y.K. Fung, Y.W. Chen, J.W. Hong, and C.Y. Chang, IEEE Trans. Electron Devices **32** (1988) 1279.

[7] K. Sawada, C. Mochizuki, S. Akata, and T. Ando, Appl. Phys. Lett. **65** (1994) 1364, *ibid* **68** (1996) 1835.

[8] S. Sugawa, K. Kozuka, T. Atoji, H. Tokunaga, H. Shimizu, and K. Ohmi, Jpn. J. Appl. Phys. **35** (1996) 1014.

[9] J.B. Chévrier and B. Equer, J. Appl. Phys. **76** (1994) 7415.

[10] G. Juska, K. Arlauskas, J. Kocka, M. Hoheisel, and P. Chabloz, Phys. Rev. Lett. **75** (1995) 2984, G. Juska, K. Arlauskas, and J. Kocka, J. Non-Cryst. Solids **198–200** (1996) 202.

[11] M. Wraback and J. Tauc, Phys. Rev. Lett. **69** (1992) 3682.

[12] A. Mourchild, D. Hunlin, R. Vanderhaghen, and P.M. Fauchet, Semicond. Sci. Technol. **7** (1992) B302.

[13] S. Sugawa, K. Ohmi, M. Yamanobe, and Y. Osada, Solid State Comm. **80** (1991) 373.

[14] A.G. Chynoweth, and H.K. McKay, Phys. Rev. **102** (1956) 369.

[15] A. Toriumi, M. Yoshimi, M. Iwase, Y. Akiyama, and K. Taniguchi, IEEE Trans.

Electron Devices **34** (1987) 1501.

[16] M. Herzog, M. Schels, F. Koch, C. Moglesture, and J. Rosenzweig, Solid-State Electron. **32** (1989) 1765.

[17] A.L. Lacaita, F. Zappa, S. Bifiliardi, and M. Manfredi, IEEE Trans. Electron Devices **40** (1993) 577.

[18] J.I. Pankove, in *Electroluminescence, Topics in Applied Physics*, vol. 17, (Spring-Verlag, Berlin, 1977), in *Display Device, Topics in Applied Physics*, vol. 40, (Spring-Verlag, Berlin, 1980).

[19] Y. Hamakawa, D. Kruangam, T. Toyama, M. Yoshimi, S.M. Paasche, and H. Okamoto, Optoelectronics – Device and Technol. – **4** (1989) 281.

[20] Y. Hamakawa, T. Toyama, and H. Okamoto, J. Non-Cryst. Solids **115** (1989) 180.

[21] M. Yoshimi, H. Shimizu, K. Hattori, H. Okamoto, and Y. Hamakawa, Optoelectronics – Device and Technol. – **7** (1992) 69.

[22] T. Toyama, M. Yoshimi, T. Ishiko, T. Tachi, K. Hiratsuka, H. Okamoto, and Y. Hamakawa, Optoelectronics - Device and Technol. - **9** (1994) 401.

[23] Y. Hattori, D.Kruangam, T. Toyama, H. Okamoto and Y. Hamakawa, J. Non-Cryst. Solids, **97&98** (1987) 1079.

[24] R.A. Street, in *Hydrogenated Amorphous Silicon, Semiconductors and Semimetals*, vol. 21, Part B, ed. J.I. Pankove (Academic Press, New York, 1984) Chap. 7, pp. 197–244.

[25] J.I. Pankove and D.E. Carson, Appl. Phys. Lett. **29** (1976) 620.

[26] G.D. Cody, in *Hydrogenated Amorphous Silicon, Semiconductors and Semimetals*, vol. 21, Part B, ed. J.I. Pankove (Academic Press, New York, 1984) Chap. 2, pp. 11–82.

[27] T.S. Nashashibi, I.G. Austin, and T.M. Searle, Philos. Mag. **35** (1977) 831.

[28] K. Jahn, R. Carius, and W. Fuhs, J. Non-Cryst. Solids **97&98** (1987) 575.

[29] T. Figielsky and A. Torun, *Proc. Intern. Conf. Physics of Semiconductors*, Exeter, UK, (1962) 853.

[30] J. Bude, N. Sano, and A. Yoshii, Phys. Rev. **45** (1992) 5848.

[31] S. Villa, A.L. Lacaita, and A. Pacelli, Phys. Rev. B **52** (1995) 10993.

[32] F. Capasso, in *Lightwave Communications Technology, Semicondoctors and Semimetals*, vol. 22, Part D, ed. W.T. Tsang (Academic Press, New York, 1985) Chap. 1, pp. 38–43.

[33] B.K. Ridley, J. Phys. C **16** (1983) 3373.

[34] S. McKenzie and M.G. Burt, J. Phys. C **19** (1986) 1959.

[35] E. Bringuier, Phys. Rev. B **49** (1994) 7974.

[36] M.H. Brodsky, in *Hydrogenated Amorphous Silicon, Semiconductors and*

Semimetals, vol. 21, Part B, ed. J.I. Pankove (Academic Press, New York, 1984) Chap. 2, pp. 11–82.

[37] N.F. Mott, Philos. Mag. B **63** (1991) 3.

[38] H. Okamoto, K. Hattori, and Y. Hamakawa, J. Non-Cryst. Solids **164–166** (1994) 445.

[39] Y. Tsutsumi, H. Okamoto, K. Hattori, and Y. Hamakawa, Philos. Mag. B **69** (1994) 253 , Mater. Res. Soc. Symp. Proc. **336** (1994) 343.

[40] E.N. Economou, C.M. Soukoulis, M.H. Cohen, and A.D. Zdetsis, Phys. Rev. B **31** (1985) 6712, E.N. Economou, M.H. Cohen, and C.M. Soukoulis, J. Non-Cryst. Solids **77–78** (1985) 151.

[41] F. Yonezawa and F. Sato, J. Phys. Soc. Japan, **57** (1988) 1797.

[42] K. Hattori, H. Okamoto, and Y. Hamakawa, J. Non-Cryst. Solids **114** (1989) 687.

[43] K. Hattori, T. Mori, H. Okamoto, and Y. Hamakawa, Phys. Rev. Lett. **60** (1988) 825.

[44] A. Schmid, in *Localization and Interaction, and Transport Phenomena, Solid State Science*, vol. 61, ed. B. Kramer, G. Bergmann, and Y. Bruynseraede (Spring-Verlag, Berlin, 1985) p.212.

[45] Y. Hamakawa, Y. Tawada, K. Nishimura, K. Tsuge, M. Kondo, K. Fujimoto, S. Nonomura, and H. Okamoto, *Proc. 16th IEEE Photovoltaic Specialists Conf.*, San Diego, US (1982) 679.

[46] A. Morimoto, S. Oozora, M. Kumeda, and T. Shimizu, Solid State Commun. **47** (1983) 773.

Chapter III

Avalanche Multiplication in Hydrogenated Amorphous Silicon

3.1. Introduction

In Chapter II, we have elucidated visible electroluminescent (EL) emission at high electric field from hydrogenated amorphous silicon (*a*-Si:H), and concluded that the most likely mechanism for the EL emission is hot-electron induced intraband transitions. In the case of crystalline semiconductors, hot-electron-induced EL emission is one of the precursors for avalanche multiplication. In associated with amorphous semiconductors, Tanioka *et al.* have reported the observation of photocurrent multiplication in amorphous selenium (*a*-Se) as the avalanche multiplication. They have also succeeded in the development of a novel high-gain image pick-up tube as the application device. [1] This has highly stimulated the researchers studying *a*-Si:H with expectation for the avalanche multiplication in *a*-Si:H and application to a high-gain photodiode.

In this chapter, we mention experimental results on the electric field in *a*-Si:H monitored by the electroabsorption (EA) method and on the transferred electron multiplication in *a*-Si:H as the extended experimental results. Furthermore we examine that the transferred electron multiplication is avalanche multiplication in *a*-Si:H. [2–5]

3.2. Electroabsorption

3.2.1. *Experimental Configuration*

The electric field in *a*-Si:H layer F_{Si} has been measured on the actual EL device by the EA technique. [6,7] Figure 3.1 illustrates the setup of the EA measurement apparatus. The EA measurement was carried out at a reflection geometry. Probe light was applied on the EL device from the glass side and reflected by the rear side Al electrode. The reflection light was monitored by a Si photodiode. The wavelength of the probe light was chosen as 660 nm using a light emitting diode or monochromatic tungsten lamp. The EA signal is thereby reflected only for the change in the *a*-Si:H layer, while the signal due to the *a*-SiN:H layers does not appear in this wavelength range. Therefore the "reflection" signal dominantly reflects the electric field induced change in the optical absorption in the *a*-Si:H layer. The incident photon flux is roughly estimated to be 10^{14} photons/cm^2 sec.

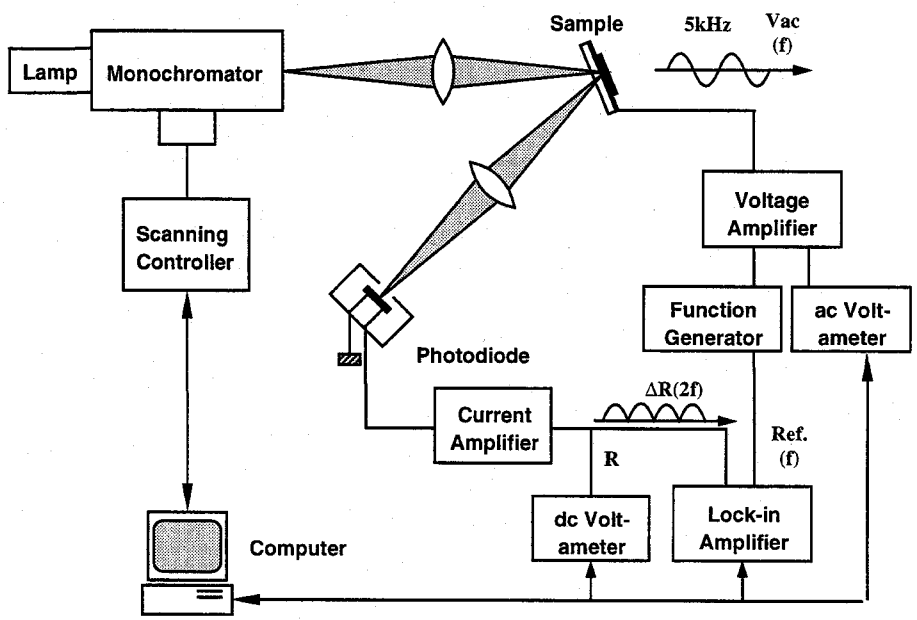

Fig. 3.1. Schematic diagram of EA measurement configuration.

The electric field was modulated at the same frequency of 5 kHz as the EL spectrum measurement in Chapter II, whereas the modulation component of the reflection light was detected at twice frequency by a double phase lock-in amplifier (NF Circuit Block, 5610B) because the absorption coefficient in *a*-Si:H is distorted in accordance with absolute electric field in *a*-Si:H. From the modulation component ΔR and the dc component R, which was monitored simultaneously by a digital multimeter, the EA signal $\Delta S = \Delta R/R$ was obtained.

3.2.2. *Translation from EA Signal to Electric Field*

A typical experimental data is shown in Fig. 3.2, in which the axis of F_{Si} is scaled by the following procedure. Under a low ($F_{Si} \ll 10^8$ V/cm), uniform electric field, the EA signal ΔS is given by

$$\Delta S \propto \Delta\alpha \propto F_{Si}^2 . \tag{3.1}$$

where $\Delta\alpha$ denotes as the field-induced change in the absorption coefficient in *a*-Si:H layer. [6,7] As displayed in Fig. 3.2, the square root of the EA signal is proportional to the total voltage applied across the EL devices (V_a) less than several tens volts (the linear region is changed due to the EL device structures such as *a*-Si:H and *a*-SiN:H thicknesses). In this linear region, the EL device can be modeled as capacitors in series; i.e. an *a*-Si:H capacitor and an *a*-SiN:H one (consisting of the two *a*-SiN:H layers). Thereby the electric field in the *a*-Si:H layer is expressed by

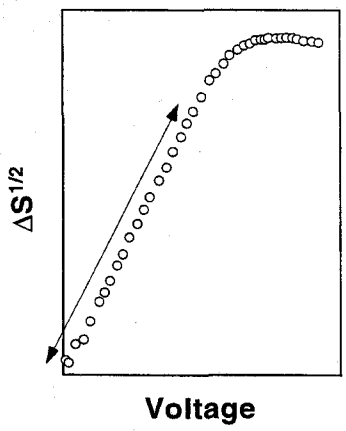

Fig. 3.2. The square of EA signal plotted against the applied voltage.

$$F_{Si} = \frac{C_{SiN}}{d_{Si}(C_{Si} + C_{SiN})} V_a . \tag{3.2}$$

where C_{Si} and C_{SiN} denote the capacitance per unit area which are given by $\varepsilon_0\varepsilon_{Si}/d_{Si}$ and $\varepsilon_0\varepsilon_{SiN}/2d_{SiN}$, respectively. ε_{Si} and ε_{SiN} denote the dielectric constants, d_{Si} and d_{SiN} the thicknesses. The indexes for C, ε, and d refer to the corresponding layers. Employing Eqs. (3.1) and (3.2), the EA signals are translated into the internal electric field in *a*-Si:H, F_{Si}.

3.3. Avalanche Multiplication

3.3.1. *Electric Field in a-Si:H*

Figure 3.3 shows electric field in *a*-Si:H plotted against applied voltage, V_a, as a function of the *a*-Si:H thicknesses of 200–500 nm measured at room temperature. At any thickness of *a*-Si:H, the electric fields in *a*-Si:H tend to saturate above the applied voltage of about 150 V, and the saturation fields exceed 1 MV/cm. The saturation fields decrease with increasing the *a*-Si:H thicknesses. In

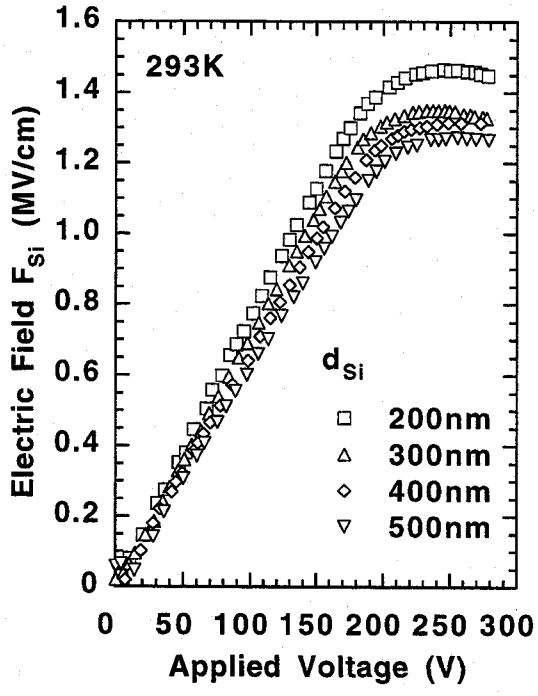

Fig. 3.3. Electric field of *a*-Si:H (F_{Si}) – applied voltage characteristics as a function of *a*-Si:H thickness (d_{Si}). [d_{Si}: 200 nm, □ ; 300 nm, △ ; 400 nm, ◇; 500 nm, ▽]. F_{Si} is translated by Eqs. (3.1), (3.2) from the EA signal.

comparison with Fig. 2.4 which displays the EL intensity characteristics as a function of the applied voltage at various thicknesses of *a*-Si:H, the light emission becomes detectable when electric field in *a*-Si:H reaches nearby 1 MV/cm, just below the saturation field.

3.3.2. *Transferred Charge*

We shall analyze the field saturation phenomenon observed in Fig. 3.3. As described previously, under an operating voltage less than about 150 V, the electric field in *a*-Si:H, F_{Si}, is proportional to the applied voltage, V_a. However, F_{Si} saturates where V_a exceeds about 150 V as shown in Fig. 3.3. We assume that the electric field distortion shown schematically in Fig. 3.4 is caused by the transferred charge per unit area, Q_t, which is accumulated at the interface between *a*-Si:H and *a*-SiN:H, is swept out by the electric field in *a*-Si:H and transferred to the *a*-Si:H/*a*-SiN:H interface locating at the opposite side across the *a*-Si:H layer. [8, 9]

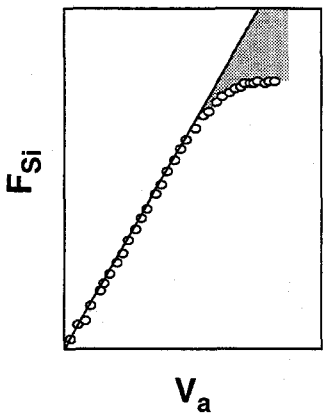

Fig. 3.4. Electric field distortion in F_{Si}–V_a characteristics. We assume the distortion due to the counter electric field caused by the transferred charge (electron).

Now, Q_t is written by

$$Q_t = \varepsilon_0 \varepsilon_{Si} F_{Si} - \varepsilon_0 \varepsilon_{SiN} F_{SiN}. \tag{3.3}$$

Since V_a is expressed by $V_a = F_{Si} d_{Si} + F_{SiN} d_{SiN}$, Eq. (3.2) is reformed as

$$F_{Si} = \frac{C_{SiN} V_a + Q_t}{d_{Si}(C_{Si} + C_{SiN})}. \tag{3.4}$$

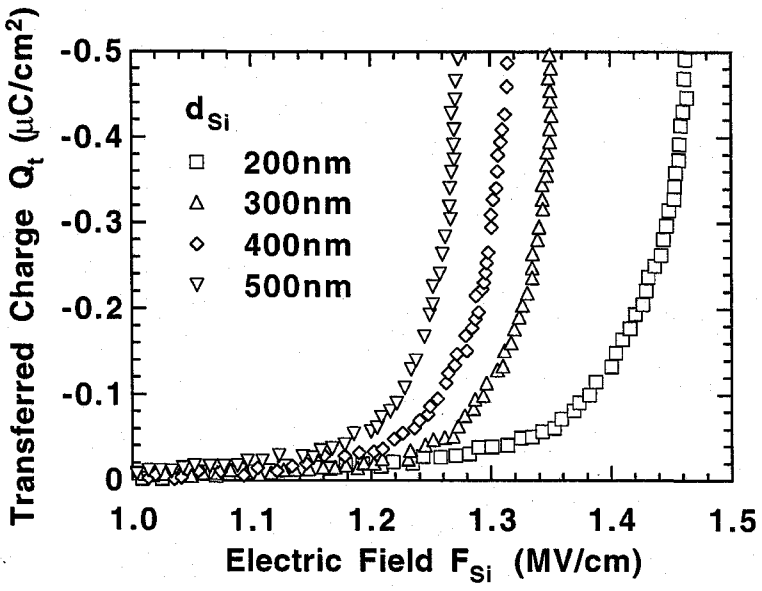

Fig. 3.5. Transferred electron (Q_t) characteristics as a function of electric field of *a*-Si:H (F_{Si}). This figure is replotted from Fig. 3.3 according to Eq. (3.5). [d_{Si}: 200 nm, □; 300 nm, △; 400 nm, ◇; 500 nm, ▽].

Equation (3.4) directly leads to

$$Q_t = d_{Si}(C_{Si} + C_{SiN})F_{Si} - C_{SiN}V_a. \qquad (3.5)$$

Figure 3.5 shows the relation between the transferred charges, Q_t, and the electric fields in *a*-Si:H (F_{Si}) as a function of the thickness of *a*-Si:H layer, which is replotted from Fig. 3.3 in accordance with Eq. (3.5). We claim that electrons would dominate the transferred charge. The transferred electrons increase sharply at any thickness of *a*-Si:H with two features:

i) The increase of the transferred electrons occurs when the electric field exceeds 1.2–1.5 MV/cm.

ii) At the same electric field above 1.2 MV/cm, the transferred electrons increases with an increase in the thickness of *a*-Si:H layer.

3.3.2. *Mechanism for Carrier Multiplication*

Two mechanisms for the multiplication have been proposed: one is the electric-field-induced electron injection from the external electrodes or charge emission from deep level states at *a*-Si:H/*a*-SiN:H interface, and the other is the avalanche multiplication.

To exclude the occurrence of the current injection or the charge emission, the alternative EA measurement was performed. In the EA measurement, the *a*-Si:H thickness was fixed at 200 nm, whereas the thicknesses of two *a*-SiN:H layers in the EL device were simultaneously changed from 200 nm to 500 nm. Figure 3.6 shows the transferred electrons plotted against the electric fields in *a*-Si:H at different thicknesses of *a*-SiN:H. In Fig. 3.6, the electron multiplication occurs at almost the same electric field in *a*-Si:H. As lead from Eq. (3.4), electric field in *a*-SiN:H decreases with an increase in the *a*-SiN:H thickness when the electric field in *a*-Si:H reaches at an equal field. Therefore the electron multiplication is independent of the electric field in the *a*-SiN:H layers. If the transferred electrons in *a*-Si:H

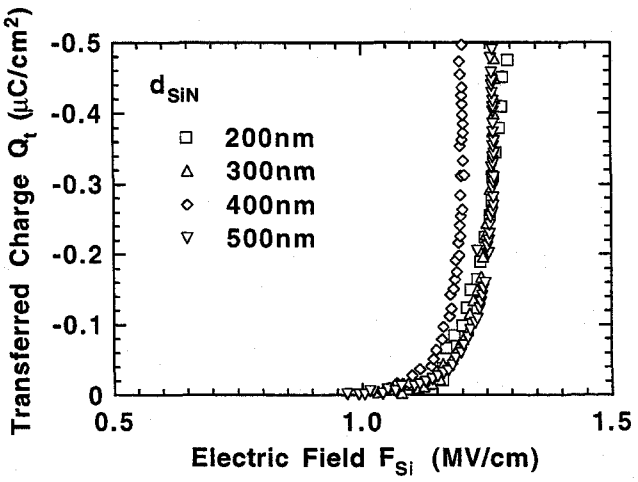

Fig. 3.6. Transferred electron (Q_t) characteristics plotted against internal electric field in a-Si:H (F_{Si}) at various thicknesses of *a*-SiN:H (d_{SiN}). [d_{SiN}: 200 nm, □; 300 nm, △; 400 nm, ◇; 500 nm, ▽].

increase due to the electron injction (i.e. field-induced tunneling injection or field-assisted thermal emission), the amount of transferred electrons depends on the electric field in *a*-SiN:H. Consequently, the result in Fig. 3.6 leads that the electron injection from external electrodes or *a*-Si:H/*a*-SiN:H interface states is negligible.

On the other hand, two electron multiplication features in Fig. 3.5 imply that the multiplication mechanism should dominate avalanche multiplication. The onset electric fields of 1.2–1.5 MV/cm for the electron multiplication is consist with the EL results mentioned in Chapter II, i.e. the onset electric fields are almost equivalent or slightly larger comparing with those of the hot-electron-induced EL in *a*-Si:H. As mentioned previously, the hot-electron-induced EL is a precursor of the avalanche multiplication in crystalline semiconductors.

In addition, the onset electric field of 1.2–1.5 MV/cm is good agreement with the expectation in the study of the reversely biased *a*-Si:H *p-i-n* junction photodiode. [10] In the study the electron multiplication has not monitored at the electric field in *a*-Si:H up to 0.8 MV/cm, although Chévrier and Equer have claimed that the 50-μm-thick undoped *a*-Si:H layer in the photodiode is to be sufficient for that the electron energy gains the threshold energy for the avalanche multiplication if the electric field in *a*-Si:H exceeds 1 MV/cm.

Juska *et al.* have not observed the carrier multiplication in their time-of-flight (TOF) measurements employing the *a*-Si:H *p-i-n* junction photodiode in which undoped *a*-Si:H layer was 50-μm thick. [11] They have estimated that the threshold energy for the avalanche multiplication to be larger than 0.14 eV from their experiments. The average electron energy at 1.2 MV/cm is estimated to be 0.16 eV being almost equivalent to the Juska's estimation.

On the second feature of the electron multiplication in Fig. 3.5, the dependence of the electron multiplication on the *a*-Si:H thicknesses is indicative that the transferred electron increases with increasing the electron transit distance, namely, the transferred electron increases with increasing the average electron energy obtained by the electric field. Tanioka *et al.* have reported the dependence of the photocurrent multiplication on the thickness of *a*-Se and they claim the photocurrent multiplication due to the avalanche multiplication in *a*-Se using the thickness dependence as one of the grounds. [1]

Consequently, the avalanche multiplication is the most acceptable for the mechanism associated with the transferred electron multiplication observed in

Fig. 3.5.

3.4. Impact Ionization Rate

3.4.1. Estimation from EA Results

From Fig. 3.5, the electron ionization rate is estimated. In general, the relation between multiplication factor, M_n, and the ionization rate is expressed as [12]

$$1-\frac{1}{M_n}=\int_0^{d_{Si}}\alpha\exp\left[-\int_0^x(\alpha-\beta)dx'\right]dx, \qquad (3.5)$$

where α denotes the electron ionization rate, β the hole ionization rate, d_{Si} the *a*-

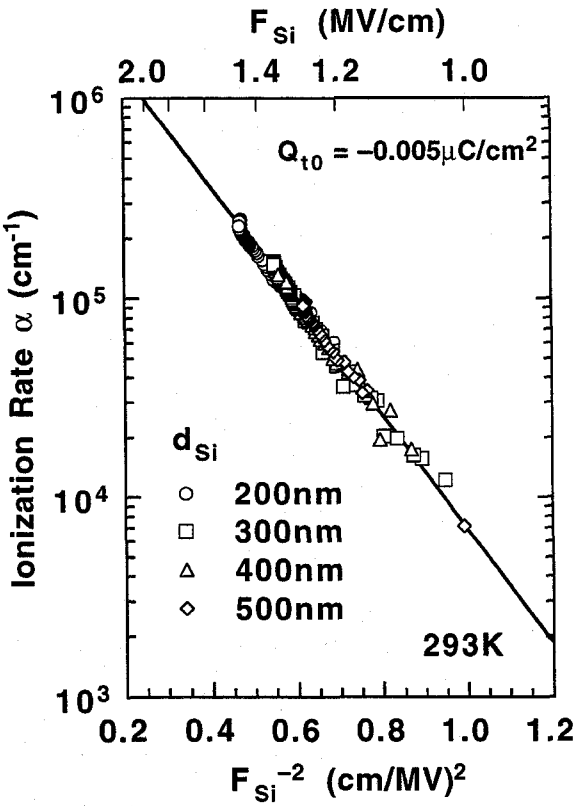

Fig. 3.7. Electron impact ionization rate (α) characteristics plotted against the inverse of the square of the internal electric field in a-Si:H (F_{Si}^{-2}) for different thicknesses of *a*-Si:H (d_{Si}). [d_{Si}: 200 nm, □; 300 nm, △; 400 nm, ◇; 500 nm, ▽].

Si:H thickness. Since the hole drift mobility in *a*-Si:H is much smaller than the electron drift mobility by two orders of magnitude at the electric field within 5×10^5 V/cm, we shall neglect hole transport in *a*-Si:H in the high electric field transport above 1 MV/cm. Namely we shall assume that β is much smaller than α. Furthermore, we consider that the multiplication takes place uniformly through out the *a*-Si:H layer. Thus Eq. (3.5) is reduced to

$$\alpha = \frac{1}{d_{Si}} \ln M_n. \tag{3.6}$$

Letting $M_n = Q_t/Q_{t0}$ and the initial transferred electron, Q_{t0}, to be –0.005 μC/cm^2, the ionization rate, α, is evaluated from Fig. 3.5 as shown in Fig. 3.7. In Fig. 3.7, the electron ionization rate is found to be expressed as a function of the inverse of the square of the internal electric field in *a*-Si:H, F_{Si}^{-2} being independent of *a*-Si:H thicknesses. According to the lucky drift model, [12–15] which successfully explains the EL spectrum in Chapter II, the electron ionization rate is written as [14]

$$\alpha = \frac{1}{\lambda_E} \cdot \frac{\exp(-l_0/\lambda_E) - (\lambda/\lambda_E)\exp(-l_0/\lambda)}{\left[1-\exp(-l_0/\lambda_E)\right] - (\lambda/\lambda_E)^2\left[1-\exp(-l_0/\lambda)\right]}, \tag{3.7}$$

where λ denotes the mean free path. The energy relaxation length, λ_E, is given by Eq. (2.2). The minimum distance, l_0, to gain the ionization threshold energy, E_i, at F_{Si} is expressed by

$$l_0 = E_i / eF_{Si}. \tag{3.8}$$

Neglecting λ relative to λ_E in Eq. (3.7) we find

$$\alpha = \frac{1}{\lambda_E} \exp(-E_i / eF_{Si}\lambda_E), \tag{3.9}$$

or

$$\alpha = \frac{E_i}{eF_{Si}} \exp(-E_i / 2eF_{Si}\lambda_E). \qquad (3.10)$$

As found from Eqs. (3.7) and (3.10), the impact ionization rate decays exponentially as a function of the inverse of the square of the internal electric field in *a*-Si:H, F_{Si}^{-2}. The mean free path is evaluated from Fig. 3.7 employing Eq. (3.10) to be 1.0 nm at the impact ionization threshold energy, E_i, of 1.8 eV. The mean free path of 1.0 nm is consistent with that deduced from the decay of the EL spectrum in Chapter II.

3.4.2. Temperature Dependence

Figure 3.8 is a calculated result on the temperature dependence of the electron ionization rate employing Eq. (3.10). Elevating the measurement temperature, the ionization rate at the same electric field decreases due to an increase in the optical-phonon scattering rate, and the slope of the ionization rate becomes monotonously

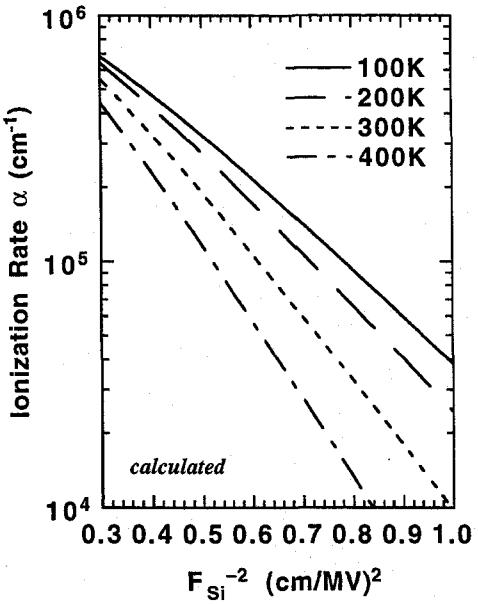

Fig. 3.8. Calculated result on the temperature dependence of electron impact ionization rate employing Eq. (3.10).

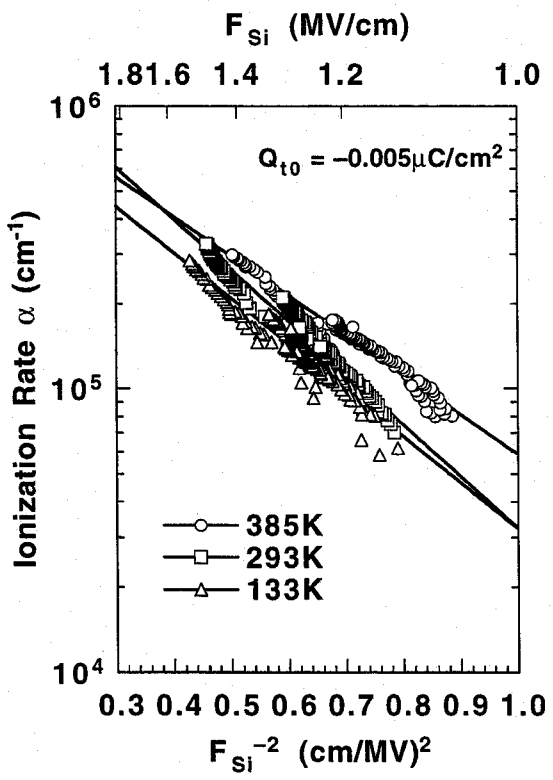

Fig. 3.9. Electric field dependence of electron impact ionization rate (α) at different measurement temperatures (T). [T: 385 K, ○; 293 K, □; 133 K, △].

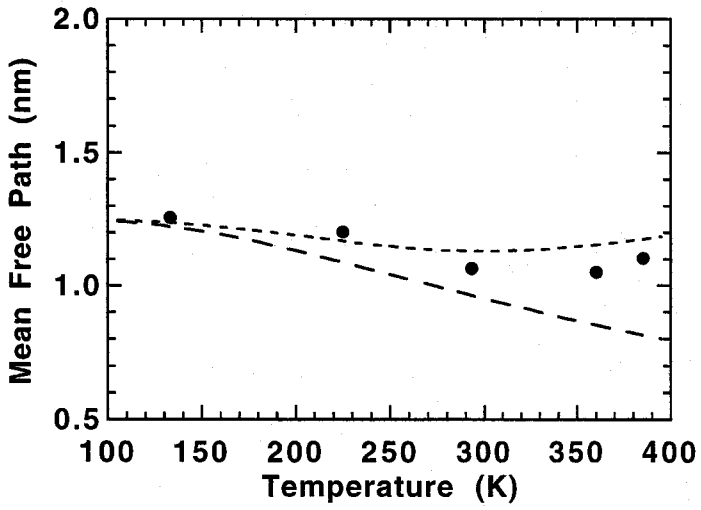

Fig. 3.10. Temperature dependence of the electron mean free path deduced from Fig. 3.8 employing Eq. (3.10). The dotted line is theoretical line calculated by Eq. (2.15).

steep.

As shown in Fig. 3.9, the electron impact ionization rate has derived at different temperatures from the EA results according to the experimental procedure in this chapter. With an increase in the temperatures, the magnitude of the ionization rate increases, which is unexpectable on the basis of the phonon scattering process.

In Fig. 3.10, the electron mean free paths deduced from the decay of the electron ionization rate according to Eq. (3.10) are plotted against the measurement temperatures. In this case, we shall neglect the temperature dependence of the impact ionization threshold energy, E_i (assuming E_i = 1.8 eV at any temperatures). With increasing the temperature up to 300 K, the mean free paths gradually decrease, while the mean free paths tend to rise in higher temperatures between 300 K and 400 K. This behavior is good agreement with the result in Fig. 2.10 in which the electron mean free paths are obtained from the decay of the hot-electron-induced EL spectrum. The dotted line in Fig 3.10 is the theoretical line based both on the optical phonon scattering and the structural-disorder-induced effect as discussed in Chapter II in detail.

Keldish showed that for semiconductors with large dielectric constants, the probability per unit time of electron-initiated impact ionization, $1/\tau_i$, can be approximated near threshold by [12,16]

$$\frac{1}{\tau_i} = \frac{1}{\tau_{ph}(E_i)} \cdot P \cdot \left(\frac{E - E_i}{E_i} \right)^2, \qquad (3.11)$$

where $1/\tau_{ph}(E_i)$ is the phonon-scattering rate of the electron at threshold energy, E_i, and P is the dimensionless constant (often assumed $P \gg 1$). In Chapter II, we have suggested that the electron mean free path in *a*-Si:H at high energies of ~0.1 eV would be determined by both phonon scattering process and structural-disorder-induced scattering process. The temperature dependence of the electron mean free path in Fig. 3.10 is thereby indicative that the term of $1/\tau_{ph}(E_i)$ in Eq. (3.11) should be modified by the model including the structural-disorder-induced scattering for the impact ionization in a-Si:H as well as the hot-electron-induced EL.

3.4.3. *Alloy Induced Effect in a-SiC:H*

The electron multiplication in *a*-SiC:H has been also observed by the EA measurements. The samples were the same as those enumerated in Table 2.2, thus the optical energy gaps of *a*-SiC:H were varied from 1.93 eV to 2.42 eV. The wavelength of the monochromatic probe light was also varied from 510 nm to 640 nm. Then the photon energy of the probe light exceeds the optical energy gap of *a*-SiC:H by about 0.1 eV. Thus the EA signal reflects only the field-induced change in the absorption coefficient of the *a*-SiC:H layer. According to the same procedure applied for *a*-Si:H, the EA signals are converted into the electric fields, the transferred electrons and the electron ionization rate in *a*-SiC:H.

As shown in Fig. 3.11, the transferred electrons in *a*-SiC:H at the different optical energy gaps arise sharply at the threshold electric fields of 1.4–1.9 MV/cm as those in *a*-Si:H. The same features on the multiplication, from which the electron multiplication is identified to be the avalanche multiplication, are also found in *a*-

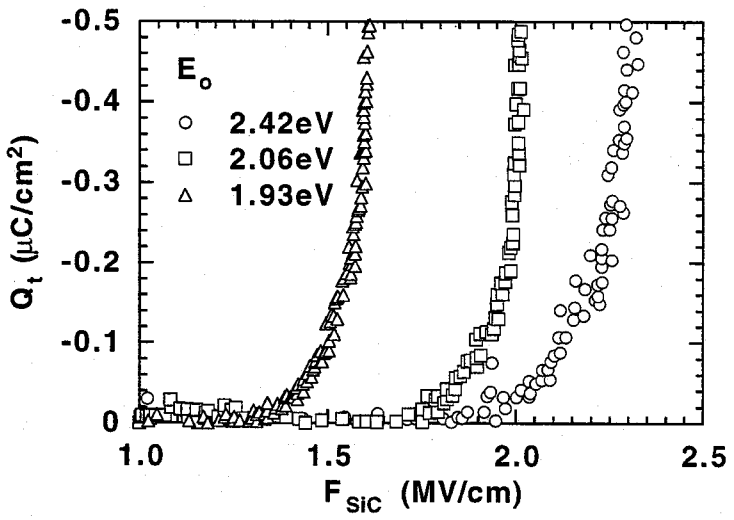

Fig. 3.11. Transferred electron (Q_t) characteristics plotted against internal electric field in a-SiC:H (F_{SiC}) at various optical energy gaps of a-SiC:H (E_o). [E_o: 2.42 eV, ○; 2.04 eV, □; 1.93 eV, △].

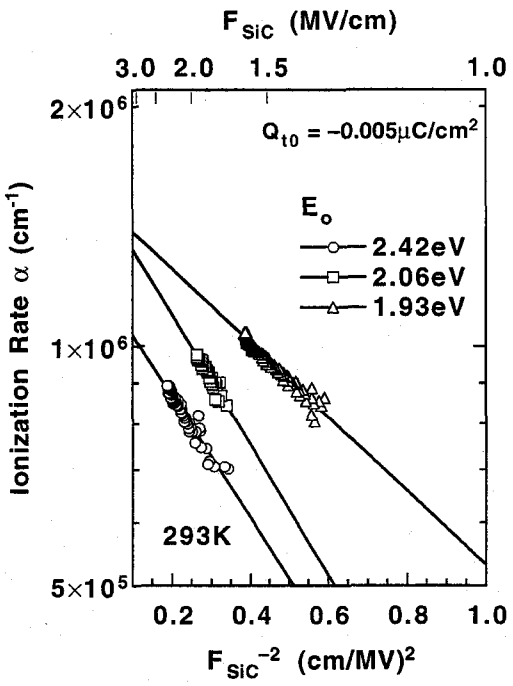

Fig. 3.12. Electron impact ionization rate (α) characteristics plotted against the inverse of the square of the internal electric field in a-SiC:H (F_{SiC}^{-2}) for different optical energy gaps of a-SiC:H (E_o). [E_o: 2.42 eV, ○ ; 2.04 eV, □ ; 1.93 eV, △].

SiC:H as in *a*-Si:H:

i) The electron multiplication depends on the thickness of *a*-SiC:H; the transferred electron increases with increasing the thickness of *a*-SiC:H.

ii) The electric field reaches a strength sufficient to generate hot-electrons just before the threshold of the multiplication as revealed from the results of the EL emission study.

Concluded by them, avalanche multiplication would dominate the electron multiplication in *a*-SiC:H shown in Fig. 3.11 as that in *a*-Si:H shown in Fig. 3.5.

The dependence on the optical energy gap is clearly found in electron ionization rate in *a*-SiC:H as a function of the inverse of the square of the internal electric field in *a*-SiC:H, F_{SiC}^{-2}, as displayed in Fig. 3.12. The electron ionization rate at an equal electric field tends to decrease with an increase in the optical energy gap of *a*-SiC:H. This tendency would be equivalent with the relation between the ionization rate and the band gap of crystalline semiconductors

3.5. Conclusions

I. Employing the EA technique, the internal electric field in *a*-Si:H has been measured with the use of the ac-driven double insulating EL devices at various thicknesses of *a*-Si:H ranging from 100 nm to 500 nm. The internal electric field saturates at the fields of 1.2–1.5 MV/cm and the saturation field decreases with an increase in the *a*-Si:H thickness.

II. Assuming the field distortion due to the transferred charge swept out from the *a*-Si:H/*a*-SiN:H interface to the counter *a*-Si:H/*a*-SiN:H interface, the transferred charge has been estimated. The transferred charge rises sharply above the threshold fields of 1.2–1.5 MV/cm.

III. Supported by three reasons: i) the dependence of the increase in the transferred charge on the electric field in *a*-Si:H as well as the thickeness of *a*-Si:H, ii) the observation of the hot-electron-induced EL emission, iii) independent of the electric fields in *a*-SiN:H layers, the avalanche multiplication mechanism is the most acceptable explanation for the carrier multiplication.

IV. The electron impact ionization rate is found to depend on the inverse of the square of the electric field in *a*-Si:H being independent of the *a*-Si:H thicknesses. The luck-drift model leads from the electron ionization rate to the estimated mean free path of 1.0 nm at the ionization threshold energy of 1.8 eV.

V. The temperature dependence of the mean free path evaluated from the electron ionization rate is good agreement with that evaluated from the EL spectrum; i.e. with an increase in the temperature from 130 K to 300 K, the mean free path gradually decreases in accordance with the theoretical line based on the optical phonon scattering process, while the mean free path tends to increase at the higher temperatures up to 400 K.

VI. The avalanche multiplication has been observed on *a*-$Si_{1-x}C_x$:H ($x < 0.3$) alloys. The electron ionization rate decreases with an increase in the optical energy gap as generally found in crystalline semiconductors.

References

[1] K. Tanioka, K. Shidara, K. Taketoshi, T. Kawamura, S. Ishioka, and Y. Takasaki, IEEE Trans. Electron Devices Lett. **8** (1987) 392.

[2] T. Toyama, K. Hiratsuka, H. Okamoto, and Y. Hamakawa, J. Appl. Phys. **77** (1995) 6354.

[3] T. Toyama, K. Hiratsuka, H. Okamoto, and Y. Hamakawa, J. Non-Cryst. Solids **198–200** (1996) 198.

[4] T. Toyama, T. Matsui, K. Hiratsuka, H. Okamoto, and Y. Hamakawa, Jpn. J. Appl. Phys. **35** (1996) 5975.

[5] T. Toyama, T. Matsui, H. Okamoto, and Y. Hamakawa, Appl. Surf. Sci. (in press).

[6] S. Nonomura, H. Okamoto, and Y. Hamakawa, Appl. Phys. A **32** (1983) 31.

[7] H. Okamoto, K.Hattori, and Y. Hamakawa, J. Non-Cryst. Solids **137&138** (1991) 627.

[8] E. Bringuier, J. Appl. Phys. **66** (1989) 1316.

[9] K.A. Neyts and P.De Visschere, J. Appl. Phys. **68** (1990) 4163.

[10] J.B. Chévrier and B. Equer, J. Appl. Phys. **76** (1994) 7415.

[11] G. Juska, K. Arlauskas, J. Kocka, M. Hoheisel, and P. Chabloz, Phys. Rev. Lett. **75** (1995) 2984, G. Juska, K. Arlauskas, and J. Kocka, J. Non-Cryst. Solids **198–200** (1996) 202.

[12] F. Capasso, in *Lightwave Communications Technology, Semicondoctors and Semimetals*, vol. 22, Part D, ed. W.T. Tsang (Academic Press, New York, 1985) Chap. 1, pp. 38–43.

[13] B.K. Ridley, J. Phys. C **16** (1983) 3373.

[14] S. McKenzie and M.G. Burt, J. Phys. C **19** (1986) 1959.

[15] E. Bringuier, Phys. Rev. B **49** (1994) 7974.

[16] L.V. Keldysh, JETP **10** (1960) 509.

Chapter IV

Red-Band Luminescence from Electrochemically Anodized Nanocrystalline Silicon

4.1. Introduction

In the next two chapters, let us introduce to the description in associated with visible light emission from nanocrystalline silicon (*nc*-Si) thin films with their optical and structural properties to discuss their emission mechanism. We elucidate two kinds of *nc*-Si thin films; electrochemically anodized *nc*-Si emitting red-band luminescence ranging in 1.7–2.0 eV in Chapter IV [1,2] and rapidly grown *nc*-Si exhibiting blue-band luminescence ranging in 2.5–2.8 eV in Chapter V. [3]

Red-band light emission from *nc*-Si has been intensively studied since the first report concerning with strong photoluminescence (PL) from porous Si and its relation to the quantum confinement effects as a low dimensional material. [4,5]. Most of the previous reports have centered upon porous Si employing crystalline Si (*c*-Si) substrates. [5,7] On the other hand, several authors have reported red-band light emission from *nc*-Si thin films with various fabrication techniques; sputtering at low temperature of ~100 K, [8] co-sputtering [9] or laser ablation [10] with the use of Si and SiO_2 target, solid phase growth by laser annealing [11] and thermally oxidization [12] or electrochemically anodization [13] from microcrystalline Si (μc-Si) prepared by plasma chemical vapor deposition (CVD).

Table 4.1 summarizes the emission models which have proposed in literature. We shall categorize the emission models to three groups: a) the quantum

Table 4.1. Proposed origins for red-band PL.

a) quantum confinement effects	
c-Si quantum wire	[4].
c-Si quantum dot	[14].
b) surface states on nc-Si	
strain-induced surface states in nc-Si	[15].
molecules on internal surface	[16].
structurally relaxed interfacial layer	[17].
defects outside or at boundary of nc-Si	[18].
near surface region of nc-Si	[19].
c) passivating materials	
SiH_2 complexes	[20].
siloxen ($Si_6O_3H_3$) derivatives	[21].
hydride-polysilane (SiH_x) complexes	[22].
a-Si phase	[23].

confinement effects, [4,14] b) the surface defects [15–19] and c) the passivating materials. [20–23] We note that the proposed model in Table 4.1 is not completely competitive for each other. In particular, one of the second origin in associated with the surface defects has proposed as the *smart* quantum confinement model by Koch *et al.* [17] which incorporates a realistic spectrum of surface states along with confinements. In this model, the dominant absorption characteristics are those of quantum confinement, but the red-band PL occurs via boundary states on the relaxed and reconfigured outermost layers of Si nanocrystallites.

In this chapter, we elucidate red-band PL from the *nc*-Si thin film formed by anodization from plasma-CVD-deposited μc-Si. In particular, we mention the dependence of the emission intensity on the crystallinity of *nc*-Si thin films comparing with PL and Raman results. From these experimental results, we discuss the emission model with the emphasis on the relation to the quantum confinement effects.

4.2. Experimental Details

4.2.1. *Sample Fabrication*

The *p*-type *nc*-Si thin film was electrochemically formed on a SnO_2-coated glass substrate from boron-doped *p*-type *μc*-Si. The *μc*-Si was deposited by the rf plasma CVD method with a low deposition temperature of 180°C. The rf power was roughly 2.5 times higher than that for an *a*-Si film. The thicknesses of the *μc*-Si were varied from 0.2 μm to 1.5 μm. A mixture of SiH_4, B_2H_6 and H_2 gases was used as a source gas. The B_2H_6/SiH_4 flow rate ratio was varied in the range from 0.1 to 2.5 vol.% to change the crystalline volume fraction in the film. The SiH_4/H_2 flow rate ratio was set to be less than about 3 vol.%. The deposition conditions for the *μc*-Si thin films are summarized in Table 4.2.

Electrochemical anodization was performed in HF aqueous solution. A 50% HF solution was further diluted by H_2O into 1/20–1/50. The anodizing current density and time were changed in the range of 1.4–9.7 mA/cm^2 and 0.5–5 min, respectively. In this experiment, bias illumination was not employed during the anodization. The anodizing conditions for the *nc*-Si thin films are summarized in Table 4.3. Anodization is quickly completed with a lower HF concentration and a lower current density in comparison with the formation of conventional porous Si. [3,4]

In addition, the thickness of *μc*-Si before anodization is found to play a crucial

Table 4.2. Deposition Conditions for *μc*-Si.

Substrate Temperature	**180°C**
Pressure	**133 Pa (1.0 Torr)**
r.f. Power	**135–210 W**
B_2H_6/SiH_4 GasFlow Rate Ratio	**0.1–2.5 vol.%**
Initial Thickness	**0.2–1.5 μm**

Table 4.3. Anodizing conditions for *nc*-Si. Anodization is quickly completed with a lower HF concentration and a lower current density in comparison with the formation of conventional porous Si.

Current density	**1.4–32.5 mA/cm^2**
Time	**0.5–2.5 min**
HF solution	
50%HF:H_2O =	**1:20–1:50**
Area	**1.54 cm^2**

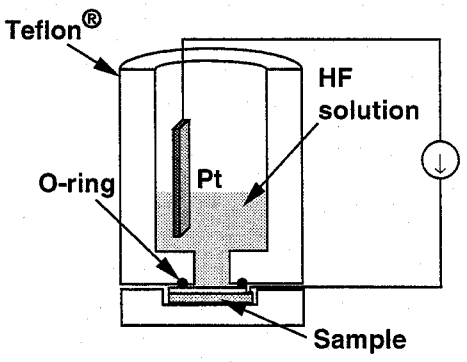

Fig. 4.1. Experimental setup for anodization. The setup is almost equivalent to the conventional setup as used in the formation of porous Si.

role for the formation of the *nc*-Si thin film. In Fig. 4.2, the formation region of the *nc*-Si is schematically displayed as a function of the initial thickness at different anodizing current densities for the anodizing time of 1 min. We shall call the thickness of μc-Si before anodization as the initial thickness of *nc*-Si.

4.2.2. *Film Characterization*

PL spectrum measurements were performed excited by ultraviolet light with a wavelength of 325 nm using a He-Cd laser (Omnichrome 3074). Since ultraviolet light was used as the excitation source, we shall consider that the excitation light is almost completely absorbed into the *nc*-Si thin films with any initial thicknesses. Therefore PL intensity would reflect simply the external emission efficiency. The excitation light power was roughly estimated to be 40 mW. The PL spectra were measured at room temperature with the use of the conventional lock-in detection system: the monochromator, the cooled GaAs(Cs) photomultiplier and the lock-in amplifier (see Chapter II). The laser light was mechanically chopped with a frequency of 820 Hz. The PL spectra were corrected by the spectral response of the optical system.

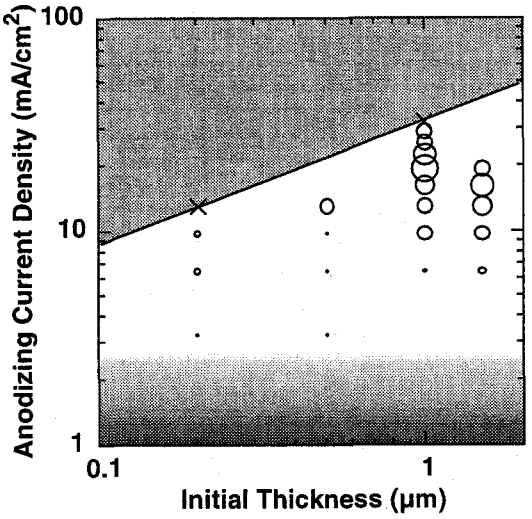

Fig. 4.2. Map for formation of the *nc*-Si plotted against the initial thickness at different anodizing current densities for anodizing time of 1 min. The diameter of the open circle schematically exhibits the PL peak intensity obtained from the *nc*-Si samples. At the cross symbols, the Si thin films were lifted off from the substrate. The left upper gray region thereby means that it is impossible to form the *nc*-Si due to the removing off at these conditions. The PL is unexpected to be detectable after anodization with a low anodizing current density within the below gradation area.

As structural characterization, Raman scattering measurement were carried out employing a microprobe system (JEOL JRS-SYSTEM 1000) including an Ar^+ laser with a wavelength of 514.5 nm. Raman scattering was measured upon an area with a diameter of about 100 μm, and incident light is perpendicular to polarization of light. The x-ray diffraction (XRD) system (Rigaku Rad-B) and the high resolution field emission scanning electron microscope (SEM) system (JEOL JSM 6020F) were employed for the characterization.

4.3. Red-Band Photoluminescence

The typical PL emission spectra are displayed in Fig. 4.3. The *nc*-Si samples in Fig. 4.3 were anodized with different anodizing current densities for 1 min. The initial thickness was set to be 0.2 μm. The red-band PL was detected from the anodized *nc*-Si thin films at room temperature except for the sample anodized at 1.4 mA/cm^2 of which the Raman spectrum is almost unchanged from that before anodization. The PL intensity increases gradually with an increase in anodizing current density.

In addition PL properties are found to depend on the initial thickness of the *nc*-Si thin films as exhibited in Fig. 4.4. The *nc*-Si samples with the different initial thicknesses ranging in 0.2–1.5 μm were anodized at 9.7 mA/cm^2 for 1 min. In Fig. 4.4, he PL peak energy shifts down and the PL intensity increases with an increase in the initial thickness.

Gaussian broadband spectral shape with peak energies of 1.6–1.8 eV and

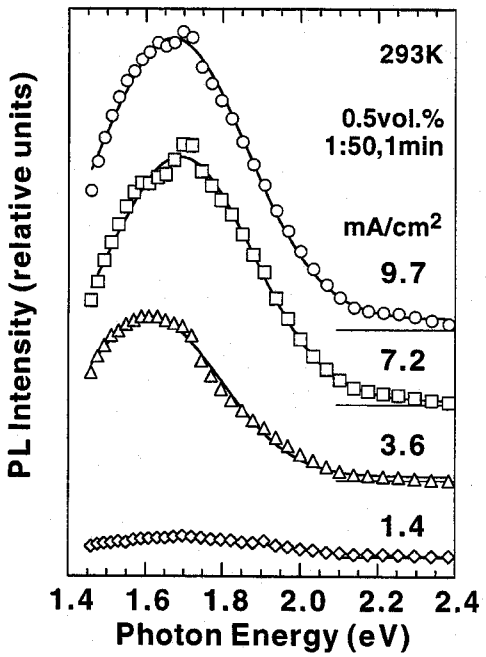

Fig. 4.3. PL spectra from the *nc*-Si excited by a He-Cd laser (λ_{exc} = 325 nm) at room temperature. The samples were anodized at different anodizing current densities [9.7 mA/cm^2, ○; 7.2 mA/cm^2, □; 3.6 mA/cm^2, △; 1.4 mA/cm^2, ◇] for 1 min. The initial thickness was set to be 0.2 μm. The lines are fitting results to the Gaussian form.

full width at half-maximums (FWHMs) as large as 0.2–0.3 eV are similar to the PL spectrum observed in porous Si and some other low-dimensional Si materials. [4,6–7] Blue shift and broadening of the PL spectrum with an increase in the anodizing current density are found as done in porous Si. [24] Regarding porous Si, the porosity of porous Si increases with increasing anodizing current density. Therefore the blue shift of PL spectrum with increasing anodizing current density is believed to be provided the first important evidence that quantum confinement effects could be playing a role. Additionally the correlation between the PL properties and the porosity has been found in the depth profile in porous Si, i.e. with increase in the distance from the porous Si surface, the porosity decreases and the PL peak energy and the PL intensity also decrease. The depth profile in porous Si would be induced by the difference of the anodizing time. Thus the depth dependence of porous Si cannot be directly applied to the initial thickness dependence of the *nc*-Si which was anodized for constant time. However the correlation between PL properties and the crystallite size is expectable to be applied to the case of the *nc*-Si.

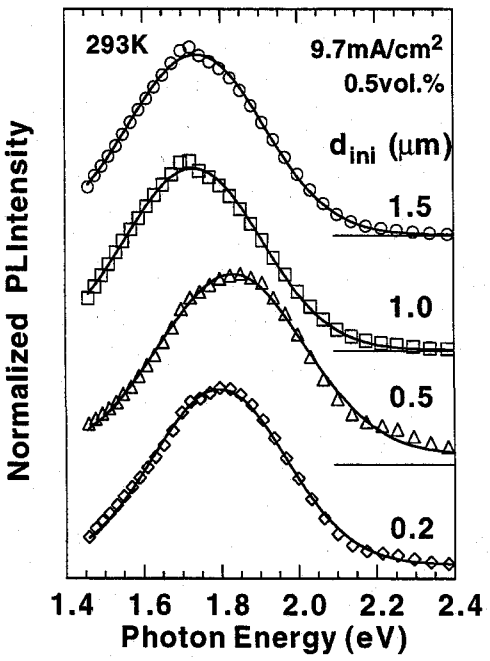

Fig. 4.4. PL spectra from the *nc*-Si as a function of the initial thickness (d_{ini}) [d_{ini}: 1.5 μm, ○; 1.0 μm, □; 0.5 μm, △; 0.2 μm, ◇]. The lines are fitting results to the Gaussian form. The spectrum in Fig. 4.4 (◇) and the spectrum in Fig. 4.3 (○) are measured on different samples with the same anodizing conditions and the different deposition conditions for *μc*-Si before anodization.

4.4. Structural Characterization

4.4.1. *Surface Morphology*

Let us discuss the structural properties through SEM, XRD and Raman scattering results with a stress on crystallite size of the *nc*-Si comparing with the results of porous Si in literature.

Figure 4.5 shows the surface morphology of the Si thin films taken by the SEM comparing the surface before anodization (Fig. 4.5(a)) with that of after anodization (Fig. 4.5(b)). The sample in Fig. 4.5(b) anodized at an anodizing current density of 9.7 mA/cm^2 exhibited a visible light emission. Before anodization, several small Si crystallites seem to form on large SnO_2 polycrystallites with a diameter ranging in 200–300 nm. After anodization, the grain of *nc*-Si is not clearly identified within the present SEM resolving power even in Fig. 4.5(c) in which the further enlarged surface image of the sample in Fig. 4.5(b) is displayed. However, the *nc*-Si seems to be formed on the grains as an overcoating tissue. The pore can not be found anywhere on the surface after the anodization unlike the conventional porous Si surface. Therefore increasing PL intensity as shown in Fig. 4.3 with increasing an anodizing current density is impossible to be explained due to increasing with the porosity as done in porous Si. The differences in the porosity of porous Si are believed to reflect those in the dimensions of Si nanocrystallites within porous Si. Thus there arises a question concerning with light emission from our *nc*-Si based on the quantum confinement effects due to the dimensional change of Si nanocrystallites within the thin films.

4.4.2. *Crystallite Size*

An attempt to determine the average grain size due to the conventional way utilizing the XRD pattern has been done for the Si thin films. In Fig. 4.6, the XRD pattern of the Si thin film before anodization (Fig. 4.6(a)) is compared with that after anodization (Fig. 4.6(b)). The initial thickness was set to be 0.5 μm. The solid lines are a smoothing line of the original data as exhibited by gray lines. The

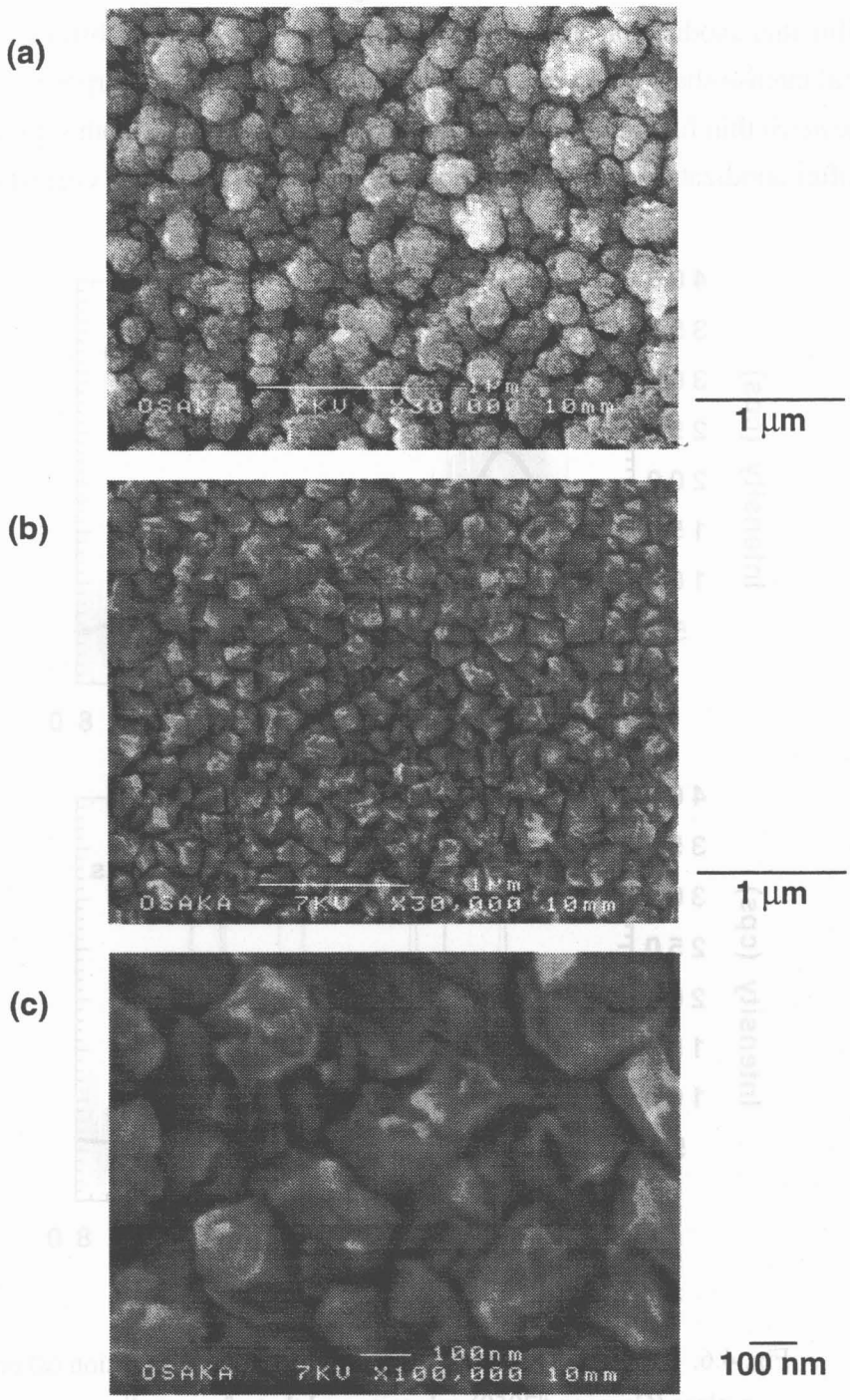

Fig. 4.5. Surface SEM image of the Si thin films before anodization (a) after anodization (b), and the enlarged image of the surface after anodization (c). The Si thin film was fabricated on SnO_2/glass substrates.

film before anodization was fabricated on a glass substrate (Corning #7059), while the film after anodization was fabricated on a SnO_2 coated glass substrate. Therefore several intense sharp peaks due to SnO_2 polycrystallites are superposed on the line of the *nc*-Si thin film after anodization. The XRD patterns for both samples before and after anodization draw the quite broadband spectra near 28° corresponding to

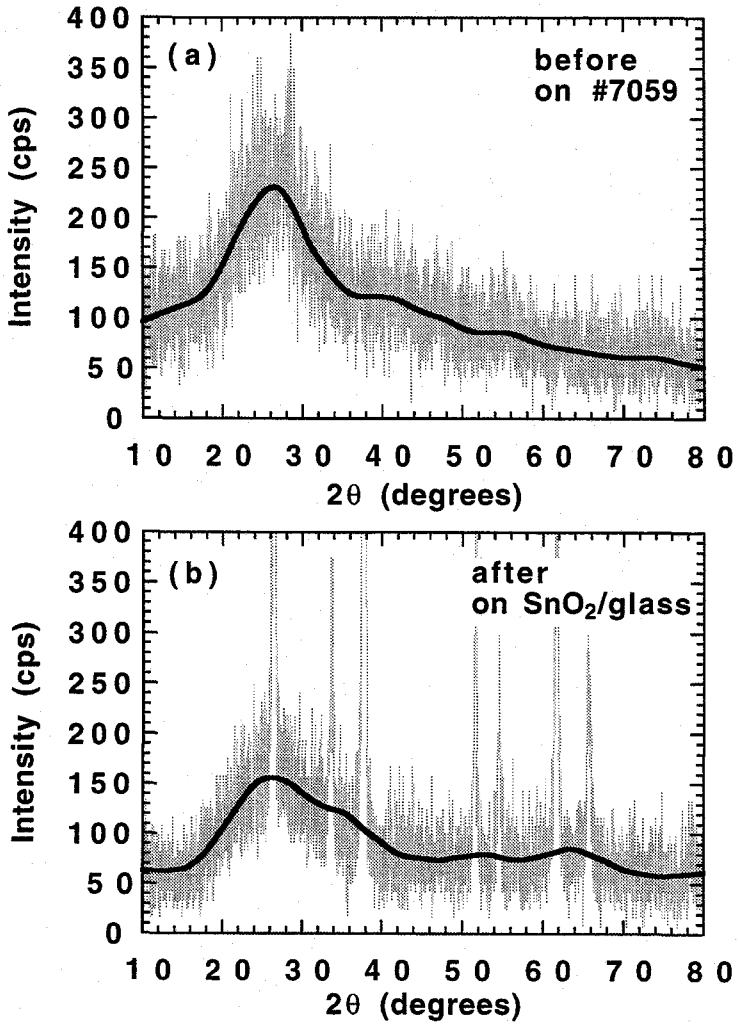

Fig. 4.6. XRD pattern of the Si thin film before anodization (a) on a glass (Corning #7059) substrate and that after anodization on a SnO_2/glass substrate (b). Solid thick lines are smoothing results evaluated from original data represented by gray thin lines. Sharp gray peaks in Fig. 4.6 (b) occur due to SnO_2 polycrystallites.

(111) plane. In addition, the FWHM of the peak at 28° for the sample after anodization becomes slightly broader than that for the sample before anodization.

The average crystallite size, L, is estimated from the FWHM by means of the Scherrer's formula: [25]

$$L = \frac{\beta \cdot \lambda}{\Gamma \cos \Theta}, \tag{4.1}$$

where λ denotes the wavelength of x-ray (CuKα, 0.15418 nm), Γ the FWHM of the XRD peak, Θ the peak angle of XRD pattern, β the collection coefficient ($\beta = 0.9$). The estimated diameters for both samples before and after anodization are only ~2 nm. However Iqbal *et al.* have reported a crystallite size of ~3 nm as the lower limit of the stability of the crystalline diamond lattice of Si from the experimental results on *μc*-Si. [26] They have claimed that below a crystallite size of ~3 nm the *μc*-Si is unstable and transforms discontinuously into the amorphous phase which is confirmed by x-ray diffraction. In the x-ray amorphous phase the crystalline component corresponding to the Γ_{25}' phonon disappears and only the Raman feature corresponding to the amorphous-like component persists. By contrast, Kanemitsu *et al.* has estimated the average diameter of Si nanocrystallites within porous Si to be 2 nm by transparent electron microscope (TEM) analysis. [19]

To accurately examine the average grain diameter of the *nc*-Si, Raman scattering measurements have been performed. Figure 4.7 displays the Raman spectra due to transverse optical (TO) phonon scattering on the *nc*-Si thin films, of which PL spectra are shown in Fig. 4.3, for various anodizing current densities. As previously mentioned, the Raman spectrum of the sample anodized at 1.4 mA/cm^2 is almost unchanged from that for as-deposited (before anodization) *μc*-Si. For the samples anodized at 3.6–9.7 mA/cm^2, the Raman spectrum becomes twofold lying at the peak of ~510 cm^{-1} corresponding to crystalline component and at the peak of ~480 cm^{-1} corresponding to amorphous-like component. [27] With an increase in anodizing current density, the crystalline/amorphous-like component ratio decreases. Comparing the PL result in Fig. 4.3, with decreasing the crystalline fraction, PL intensity increases and PL peak energy slightly shifts to blue. The decrease in the crystalline fraction in the Raman spectrum is likely to indicate the

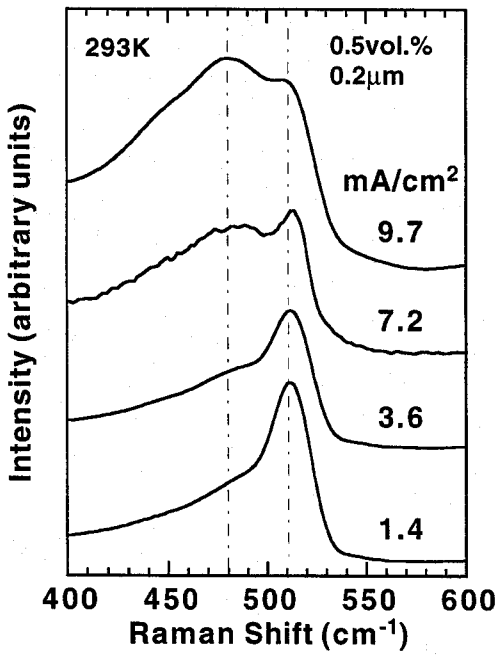

Fig. 4.7. Raman scattering spectra for the *nc*-Si samples in Fig. 4.3 as a function of anodizing current densities of 1.4–9.7 mA/cm^2.

reduction of the crystallite size.

Figure 4.8 shows the Raman spectra on the *nc*-Si thin films, of which PL spectra are shown in Fig. 4.4, for the various initial thicknesses. Also shown in Fig. 4.8 are Raman spectra on the μc-Si before anodization. With increasing the initial thickness of the *nc*-Si, the amorphous-like component at the peak of ~480 cm^{-1} almost disappears. Concerning with the samples except for the thinnest one, the spectral change between before and after anodization is markedly small. The spectral shape is asymmetry with a lower central frequency by ~10 cm^{-1} and broader spectral width of 30–40 cm^{-1} comparing with the spectrum in *c*-Si.

The asymmetry Raman spectrum in Si nanocrystallites has been induced due to the reduction of the crystallite size. [28] Richer *et al.* have interpreted the Raman signal from μc-Si (and *nc*-Si) is described in terms of a relaxation in the q vector selection rule for the excitation of the Raman active optical phonon. [29] Following Richer's work, Campbell and Fauchet have demonstrated that a Gaussian phonon confinement function with a rigid boundary yields consistent experimental results for Si crystallites. [30] According to Campbell and Fauchet, the first order Raman spectrum $I(\omega)$ is given by

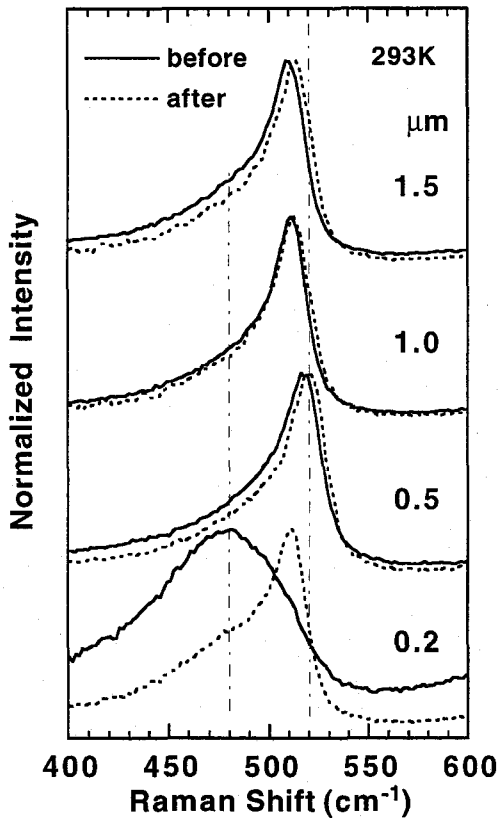

Fig. 4.8. Raman scattering spectra for the *nc*-Si samples in Fig. 4.4 as a function of the initial thickness ranging from 0.2 μm to 1.5 μm. The solid lines represent the spectra on the samples after anodization and the dotted lines denote the spectra on the samples before anodization.

$$I(\omega) = \int_0^1 \frac{\exp\left(-q^2 L^2 / 4a^2\right)}{\left[\omega - \omega(q)\right]^2 + (\Gamma_0 / 2)^2} d^3 q, \qquad (4.2)$$

where q is expressed in units of $2\pi/a$, a is the lattice constant (= 0.54 nm), and Γ_0 is the natural linewidth ($\approx$ 3.6 cm^{-1} for c-Si at room temperature). Let us express analytically the phonon dispersion as [31]

$$\omega(q) = A - Bq^2, \qquad (4.3)$$

with A = 520.5 cm^{-1} and B = 120 cm^{-1} which reproduces approximately the dispersion relation for TO phonons along with [001] in Si for $L \gg a$. In Fig. 4.9, the experimental Raman spectrum is compared with the theoretical line shape

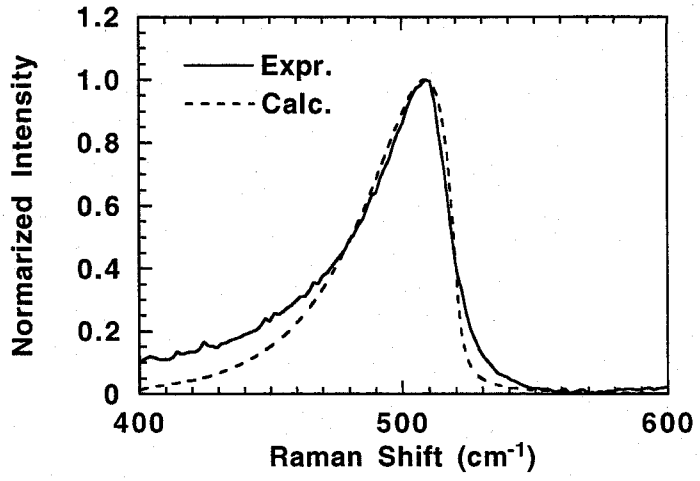

Fig. 4.9. Calculated result of Raman spectrum (dashed line) comparing with typical experimental result (solid line). The calculated line is obtained by Eqs. (4.2) and (4.3) for L = 2.65 nm.

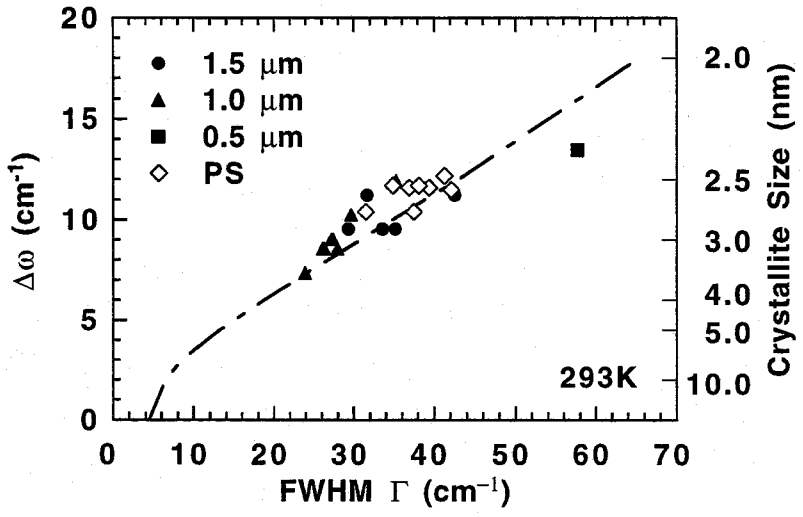

Fig. 4.10. Down-shift in center of Raman scattering frequencies from *c*-Si ($\Delta\omega$) plotted against FWHM of Raman spectrum (Γ) for various initial thicknesses (d_{ini}) of the *nc*-Si before anodization [d_{ini}: 1.5 μm, ○; 1.0 μm, □; 0.5 μm, △]. The open diamonds are the data on porous Si in ref. 31. The dashed-dotted line is theoretical line obtained from Eqs. (4.2) and (4.3). The right axis represents the crystallite size used in the calculation.

obtained from Eqs. (4.2) and (4.3).

The down-shifts of the measured Raman spectra on the *nc*-Si are plotted against the broadening in Fig. 4.10 in comparison with the theoretical line calculated by Eqs. (4.2) and (4.3). The plotted data in Fig. 4.10 are derived from the spectra almost consisting of the crystalline component, and the spectral shape was changed by the anodizing current density and the initial thickness. The right axis in Fig. 4.10 represents the crystallite size for the calculation. Also shown in Fig. 4.10 is the experimental result on porous Si in literature. [31] Figure 4.10 implies that the Raman results on the *nc*-Si would be expressed by the phonon confinement as well as porous Si and give the average size of nanocrystallites incorporated in the *nc*-Si thin films to be 2.4–3.8 nm.

In addition, we have found that the amorphous-like component in the Raman spectrum markedly appears for the Raman spectrum with $\Gamma > 60$ cm^{-1}. We believe that structural phase transition from crystal to amorphous in the nanocrystallites occurs within the threshold crystallite size of ~2.4 nm which is slightly less than the size of ~3 nm evaluated by Iqbal *et al.* [26] Apart from powder consisting of nano-sized particles, [32] the crystallites with a size of ~2.0 nm are unlikely to be stable in the passivating materials to form thin films.

4.5. Light Emission Mechanism

Let us now discuss the light emission mechanism with the described and extended results on Raman and PL measurements. As the prime concern, we shall prove whether the third term of the proposed origins in Table 4.1, i.e. amorphous-like passivating materials are responsible for the red-band PL from the *nc*-Si thin films or not.

We have performed Raman and PL measurements on the *nc*-Si with changing the crystalline volume fraction before anodization due to the gas phase boron doping ratio. The crystalline volume fraction in the μc-Si before anodization is shown in Fig. 4.11 as a function of B_2H_6/SiH_4 flow rate ratio. Also shown is the PL intensity at the photon energy of 1.7 eV after the anodization with various anodizing current densities.

From the Raman spectrum consisting of the crystal and the amorphous-like

components, the crystalline volume fraction (F_c) is estimated by [33]

$$F_c = \frac{F_c'}{F_c' + y(1 - F_c')}, \tag{4.4}$$

where $F_c' = I_c/(I_c + I_a)$, I_c and I_a are the integrated Raman intensity for crystalline and amorphous-like components, respectively. We used $y = 0.88$, the ratio of the integrated Raman cross section for *a*-Si:H to *c*-Si, and separated both components

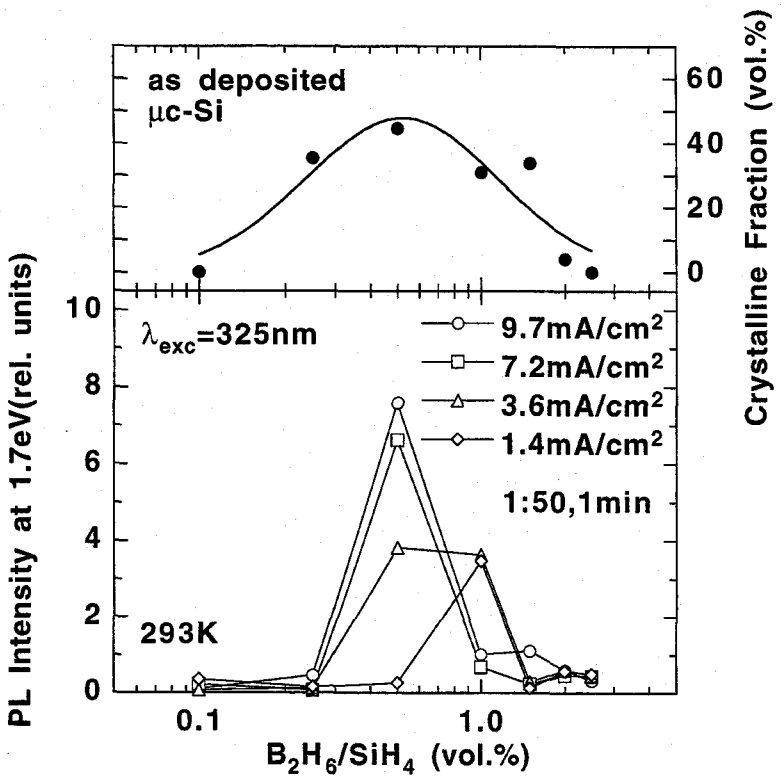

Fig. 4.10. Crystalline volume fraction (●) in the *μc*-Si before the anodization evaluated from Raman scattering measurements and PL intensity after the anodization plotted against B_2H_6/SiH_4 flow rate ratio. PL measurements were performed on the samples processed with various anodizing current densities [9.7 mA/cm^2, ○ ; 7.2 mA/cm^2, □ ; 3.6 mA/cm^2, △; 1.4 mA/cm^2, ◇]. The lines are a guide for the eye.

simply assuming to be Lorentzian lineshape.

A comparison between both results indicates that stronger PL emission occurs on the samples possessing the larger volume fraction before the anodization. In the *nc*-Si samples from which PL emission is well observed, the crystalline phase of the Raman scattering spectrum remains after anodization. On the other hand, for the samples represented as the 0% volume fraction, namely, entirely *a*-Si:H thin film before the anodization, PL emission was not detected after the anodization at any anodizing current unlike the previous report [34,35] concerning with PL emission from anodized *a*-Si:H. This implies that the luminescence in associated with the amorphous-like component, i.e. the passivating materials as proposed in literature enumerated in Table 4.1 would be inefficient comparing with the emission due to the crystalline component. If the light-emission is mainly attributed to the passivating layer, it should occur in both microcrystalline and amorphous samples, because the anodization process would identically affect on both the microcrystalline and amorphous Si. Therefore the quantum confinement and/or the surface states are likely to make a prime contribution for the emission mechanism.

Next, let us consider the correlation between the Raman and PL results on the case of the *nc*-Si with the initial thickness larger than ~0.5 μm for which the average crystallite size has obtained. Figure 4.11 shows PL properties plotted against FWHMs of the Raman spectrum, Γ, at different initial thicknesses of the *nc*-Si. The top axes represent the average crystallite size estimated from the calculation in Eqs. (4.2) and (4.3). As clearly found in Fig. 4.11(a), the PL peak intensities increase with an increase in Γ, i.e. with a decrease in the average size of nanocrystallites with in the *nc*-Si thin films. By contrast, as shown in Fig. 4.11(b), the PL peak energies are almost unchanged at any crystallite size.

The behavior on the PL intensity against the crystallite size intensely implies that the quantum confinement effects are the prime mechanism for the red-band PL in the *nc*-Si. Nevertheless, as decried in associated with Fig. 4.8, the Raman spectrum of the *nc*-Si with the large initial thickness of 0.5–1.5 μm is almost unchanged from the spectrum of *μc*-Si before anodization. This indicates that the average crystallite size of *μc*-Si would be almost equal to the crystallite size of the *nc*-Si, although visible light emission is not detectable from *μc*-Si at room temperature. This is indicative that the crystallite size of the *nc*-Si is almost determined by the size of μc-Si, i.e. the deposition conditions for μc-Si including

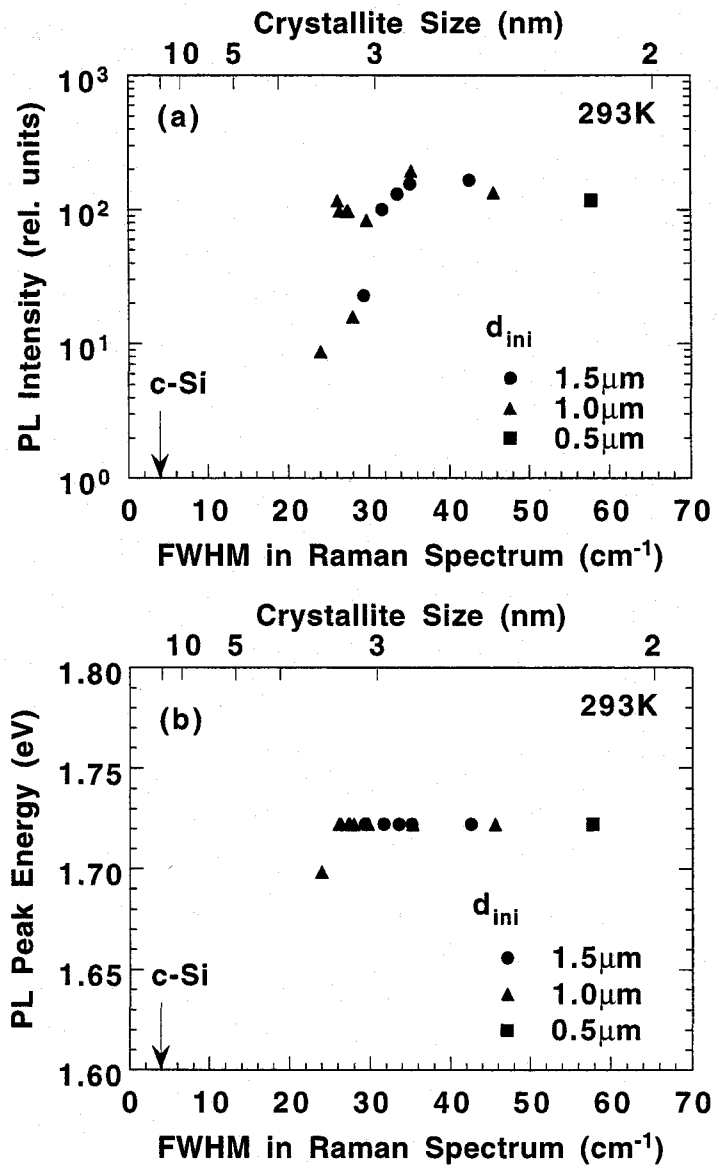

Fig. 4.12. PL peak intensities (a) and PL peak energies (b) plotted against FWHM of Raman spectrum (Γ) for various initial thicknesses (d_{ini}) [d_{ini}: 1.5 μm, ○; 1.0 μm, □; 0.5 μm, △]. Top axes represent the average nanocrystallite size of the *nc*-Si extimated in Fig. 4.10.

substrate temperatures, rf power, hydrogen dilution and gas phase boron doping ratio. Besides anodization might play a role as activation of the surface states on the *nc*-Si into the luminescent center rather than for the reduction of the crystallite size.

Tsybeskov and Fauchet have shown that there is a "universal" curve relating the red PL peak energy to the ratio of the number of Si-O and Si-H bonds, as determined from infrared spectroscopy. [36] The red PL shifts to the blue with increasing Si-O/Si-H bond number ratio. They have elucidated that the PL is produced by recombination involving surface states and comprises a combination of some luminescent bands due to different species. On the basis of this model, the results shown in Fig. 4.11 are can be interpreted that the PL intensity increases probably due to an increase in the number of Si-O and Si-H bonds, whereas the PL peak energy is almost unchanged probably due to a roughly constant Si-O/Si-H bond number ratio.

4.6. Conclusions

I. We have performed optical and structural studies on electrochemically formed *nc*-Si thin films exhibiting red-band PL emission at room temperature. The formation depends on the initial thickness and the anodizing conditions.

II. The PL properties are found to change due to the fabrication conditions including the anodizing current density, the anodizing time, the initial thickness and the crystalline volume fraction in μc-Si before anodization.

III. From the experimental and theoretical results on the Raman spectrum, the Raman spectrum in the *nc*-Si would be expressed by the phonon confinement as well as porous Si and give the average size of nanocrystallites incorporated in the *nc*-Si thin films to be 2.4–3.8 nm.

IV. The Raman scattering and PL measurements of the nc-Si have revealed the correlation between the crystalline volume fraction of μc-Si before anodization and the PL emission, indicating that the passivating materials are unlikely to contribute to the light emission.

V. The correlation between the Raman and PL results has also revealed that with decreasing the crystallite size, the PL intensity increases, while the PL

peak energy is insensitive, indicating that the light emission from the *nc*-Si would be induced by both the quantum confinement effects and the surface states on the *nc*-Si.

VI. The crystallite size mainly depends on the deposition conditions for μc-Si before anodization, while the surface states on the crystallites might be activated for the light emission due to anodization.

References

[1] T. Toyama, T. Matsui, Y. Kurokawa, H. Okamoto, and Y. Hamakawa, Appl. Phys. Lett. **69** (1996) 1261.

[2] T. Toyama, T. Matsui, T. Yamamoto, and H. Okamoto, Mater. Res. Soc. Symp. Proc. **452** (1997) (to be published).

[3] T. Toyama, T. Ouchida, H. Okamoto, and Y. Hamakawa, Appl. Surf. Sci. (in press).

[4] L.T. Canham, Appl. Phys. Lett. **57** (1990) 1046.

[5] V. Lehmann and U. Gösele, Appl. Phys. Lett, **58** (1991) 856.

[6] L.T. Canham, Phys. Stat. Sol. (b) **190** (1995) 9 and references there in.

[7] as recent studies, Z.C. Feng and R. Tsu, *Porous Silicon*, (World Scientific, Singapore, 1994), R.W. Collins, C.C. Tsai, M. Hirose, F. Koch and L. Brus, *Microcrystalline and Nanocrystalline Semiconductors*, (MRS, Pittsburgh, 1995).

[8] S. Furukawa and T. Miyasato, Jpn. J. Appl. Phys. **27** (1988) L2207.

[9] M. Yamamoto, R. Hayashi, K. Tsunetomo, K. Kohno, and Y. Osaka, Jpn. J. Appl. Phys. **30** (1991) 136.

[10] T. Takehito, Y. Yamada, and T. Orii, Mater. Res. Soc. Symp. Proc. **452** (1997) (to be published).

[11] K.M.A. El-Kader, J. Oswald, J. Kocka, and V. Cháb, Appl. Phys. Lett. **64** (1994) 2555.

[12] S. Veprek, M. Rückschoss, B. Landkammer, and O. Ambacher, Mater. Res. Soc. Symp. Proc. **298** (1993) 117.

[13] M.S. Brandt, Appl. Phys. Lett. **12** (1991) 1522.

[14] J.C. Vial, A. Bsiesy, F. Gaspard, M. Ligeon, F. Muller, R. Romestain, and R.M. Macfarlane, Phys. Rev. B **45** (1992) 14171.

[15] T. Ito, T. Ohta, and A. Hiraki, Jpn. J. Appl. Phys. **31** (1992) L1.

[16] Z.Y. Xu M. Gal, and M. Gross, Appl. Phys. Lett. **60** (1992) 1375.

[17] F. Koch, Mater. Res. Soc. Symp. Proc. **298** (1993) 319.

[18] G.G. Qin and Y.Q. Jia, Solid State Commun. **86** (1993) 559.

[19] Y. Kanemitsu, H. Uto, Y. Masumoto, T. Matsumoto, T. Futagi, and H. Mimura, Phys. Rev. Lett. B **48** (1993) 2827.

[20] C. Tsai, K.-H. Li, J. Sarathy, S. Shih, J.C. Campbell, B.K. Hance, and J.M. White, Appl. Phys. Lett. **59** (1991) 2814.

[21] M.S. Brandt, H.D. Fuchs, M. Stutzmann, J. Weber, and M. Cardons, Solid State Commun, **81** (1992) 307.

[22] S.M. Prokes O.J. Glembocki, V.M. Bermudez, R. Kaplan, L.E. Friedersdorf, and P.C. Searson, Phys. Rev. B **45** (1992) 13788.

[23] R.P. Vasquez, R.W. Fathauer, T. George, A. Ksendzov, and T.L. Lin, Appl. Phys. Lett. **60** (1992) 1004.

[24] M.I.J. Beale, N.G. Chew, M.J. Uren, A.G. Cullis, and J.D. Benjamin, Appl. Phys. Lett. **46** (1985) 86.

[25] B.D. Cullity, in *Elements of X-Ray Diffraction* (Addison-Wesley, Massachusetts, 1956).

[26] Z. Iqbal and S. Veprek, J. Phys. C. **15** (1982) 377.

[27] M.H. Brodsky, M. Cardona, and J. J. Cuomo, Phys. Rev, B **16** (1977) 3556, M.H. Brodsky, in *Light Scattering in Solids*, ed. M. Cardona, *Topics in Applied Physics*, vol. 8 (Spring-Verlag, 1975) p. 205.

[28] Stress-induced effects due to lattice expansion as described in ref. 26 should be incorporated into the origin for the down shift and broadening in the Raman spectrum. Furthermore, for the case of the microscope experimental setup, laser-light-induced thermal effects might not be neglected to affect to the down-shift and broadening. However we have followed the simple model in ref. 23–25 which explains the asymmetry shape as well as the down shift and broadening.

[29] H. Richer, Z.P. Wang and L. Ley, Solid State Commun. **39** (1981) 625.

[30] I.H. Campbell and P.M. Fauchet, Solid. State Commun. **58** (1986) 739.

[31] Z. Sui, P.P. Leong, I.P. Herman, G.S. Higashi, and H. Temkin, Appl. Phys. Lett. **60** (1992) 2086.

[32] H. Takagi, H. Ogawa, Y. Yamasaki, A. Ishizaka, and T. Nakagiri, Appl. Phys. Lett. **56** (1990) 2379.

[33] R. Tsu, J. Gonzalez-Hernandez, S. S. Chao, Sc. Lee, and K. Tanaka, Appl. Phys. Lett. **40** (1982) 534.

[34] E. Bustarret, M. Ligeon, and L. Ortega, Solid State Commun, **83** (1992) 461, E. Bustarret, M. Ligeon, and M. Rosenbauer, Phys. Stat. Sol. (b) **190**, 111 (1995).

[35] R.B. Wehrspohn, J.-N. Chazalviel, F. Ozanam, and I. Solomon, Phys. Rev. Lett.

77, 1885 (1996), J.-N. Chazalviel, R.B. Wehrspohn, I. Solomon, and F. Ozanam, Mater. Res. Soc. Symp. Proc. **452** (1997) (to be published).

[36] L. Tsybeskov and P.M. Fauchet, Appl. Phys. Lett. **64** (1994) 1983.

Chapter V

Blue-Band Photoluminescence from Rapidly Grown Nanocrystalline Si

5.1. Introduction

Investigations for visible strong photoluminescence (PL) at room temperature from nanocrystalline silicon (*nc*-Si) have been extended from those for red-band PL as mentioned the last chapter to those for blue-band PL. [1–3] Several authors have reported blue-band PL in further oxidized porous Si by some ways: by rapid thermal oxidization at high temperatures of 800–1200°C, [4,5] or by exposure to methanol [6] or boiling water. [7] In addition, blue-band PL is also observed from spark-eroded crystalline Si (*c*-Si) surface [8] and a *nc*-Si thin film fabricated by co-sputtering [9] grown from amorphous Si (*a*-Si:H) by RTA in nitrogen ambience. [10] In these cases, *nc*-Si is unexceptionally embedded in oxidized Si matrix, which is evidenced by infrared (IR) absorption spectra derived from Fourier-transform infrared (FTIR) measurements.

Table 5.1 summarizes the emission models which have proposed in literature. We shall assort the emission models for blue-band PL into three major groups in accordance with the category for red-band PL summarized in Table. 4.1 : a) quantum confinement effects, b) the surface defects, and c) the passivating materials. Furthermore the mechanism of blue-band PL has been modeled on the presence of the oxidized Si, i.e. three categories are also expressed as: a) quantum confinement effects induced by Si nanocrystallites in SiO_2, [7–11] b) Si/SiO_2 interface states, [4–6] and c) defects in SiO_2, [12–14] although the mechanism still remains

Table 5.1. Proposed origins for blue-band PL.

a) quantum confinement effects	
quantum wires	[7].
quantum dots	[9,10].
bound excitons	[11]
b) surface states on nc-Si	
surface states in nc-Si	[4].
near surface region of nc-Si	[5].
c) passivating materials	
OH groups adsorbed on defects in SiO_2	[12].
siloxen like cluster	[13].
carbon or halogen related defects in SiO_2	[14].

controversial.

In this chapter, we report blue-band PL emission from *nc*-Si thin films grown in vacuum by an RTA technique. [15] Characterization of structural properties including IR absorption due to Si-O vibration mode and crystalline size indicates that the above mechanism for the blue-band emission cannot apply to our case. A drastic change in the optical absorption spectrum upon the RTA-processed *nc*-Si is observed by a temperature modulation technique in the luminescence spectral range, which is discussed in association with the blue-band emission.

5.2. Experimental Details

5.2.1. Sample Fabrication

The fabrication process of the *nc*-Si thin film on a *c*-Si or a fused quartz substrate mainly consists of two steps; deposition of undoped *a*-Si:H by a plasma chemical vapor deposition method and solid-phase crystal growth from the *a*-Si:H

Table 5.2. Deposition conditions for *a*-Si:H

Substrate Temperature	**280°C**
Pressure	**133Pa (1.0 Torr)**
r.f. Power	**45 W**
90%SiH_4/10%H_2 Flow Rate	**20 sccm**
Thickness	**200 nm**

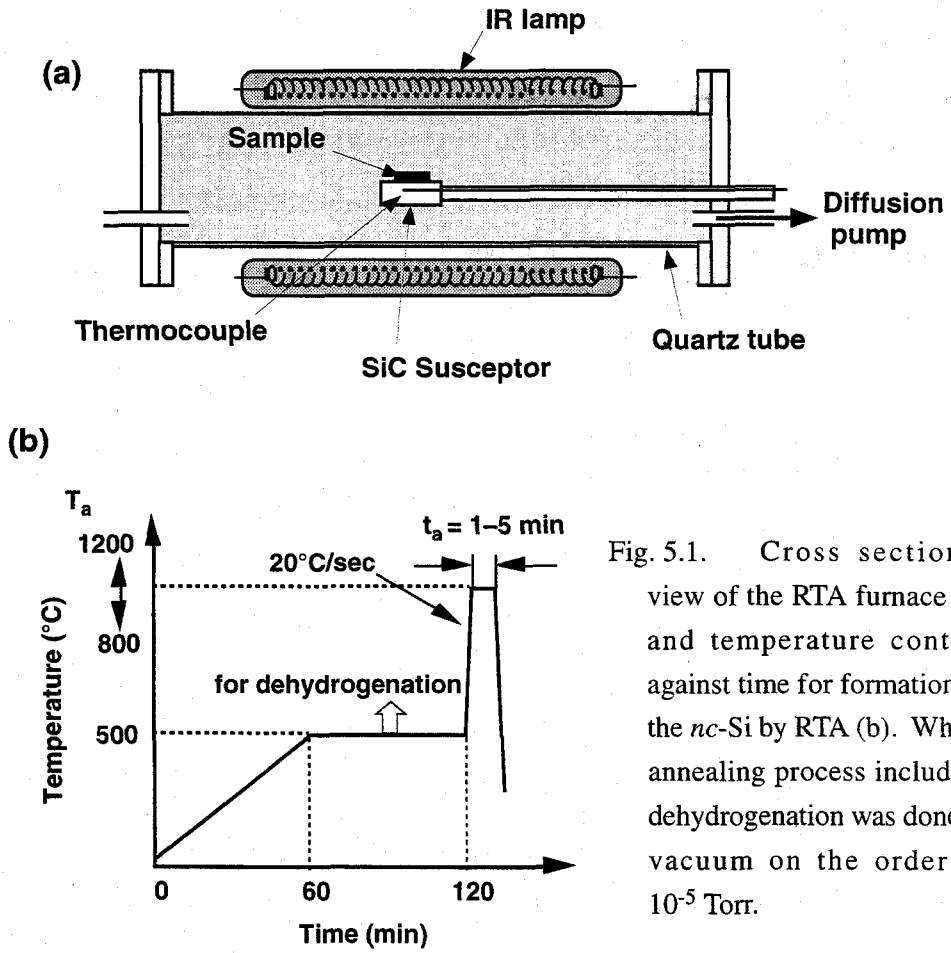

Fig. 5.1. Cross sectional view of the RTA furnace (a) and temperature control against time for formation of the *nc*-Si by RTA (b). Whole annealing process including dehydrogenation was done in vacuum on the order of 10^{-5} Torr.

by an RTA method. The deposition conditions are summarized in Table 5.2. The relatively high temperature of 280°C was held during the deposition to achieve low hydrogen incorporation in *a*-Si:H. After the first annealing for further dehydrogenation of the *a*-Si:H at 500°C for 1 h, the RTA was subsequently carried out employing an IR-lamp annealing furnace as illustrated in Fig 5.1(a). Both annealing processes were performed in vacuum with a pressure on the order of 10^{-5} Torr. The whole heating sequence was automatically controlled; ramp rate of 20°C/sec was kept from the dehydrogenation up to the growth temperature without overshooting of the temperature. The annealing time and temperature monitored at the SiC susceptor were varied in the range of 1–5 min and 800–1200°C, respectively. After the annealing process, the furnace was naturally cooled down. The time chart for the annealing process involving dehydrogenation and film growth are demonstrated in Fig. 5.1(b).

5.2.2. Film Characterization

As structural characterization, x-ray diffraction (XRD) (Rigaku RINT2000) and an atomic force microscope (AFM) (Digital Instrument NanoScope II) measurements were carried out. Raman scattering spectrum was measured with the use of a microprobe system including a 514.5-nm Ar^+ laser (JEOL JRS-SYSTEM1000). The local vibration mode in the material was analyzed by IR transmittance spectra using a FTIR measurement system (JASCO FT/IR-3).

As optical characterization, PL and optical absorption measurements were carried out. The PL was induced from the resulting *nc*-Si thin film with the use of the equipment as described in Chapter IV. Transmittance measurements were performed with the use of the optical spectrometer (Shimadzu, UV-3100PC).

Light-induced thermal modulation technique was utilized for the thermoabsorption spectroscopy (TAS) measurement. [16] As illustrated in Fig. 5.2, IR light of the wavelength above about 760 nm was mechanically modulated by an optical chopper at a frequency of 80 Hz and applied to the sample with a different angle from the probe light for the temperature modulation. A tungsten lamp light was normally applied on the sample as a probe light and its transmission light was dispersed by a monochromator (Jobin Yvon, H-20UV). Finally after detected by a Si photodiode (Hamamatsu Photonics, S1336-8BQ) and amplified by a current

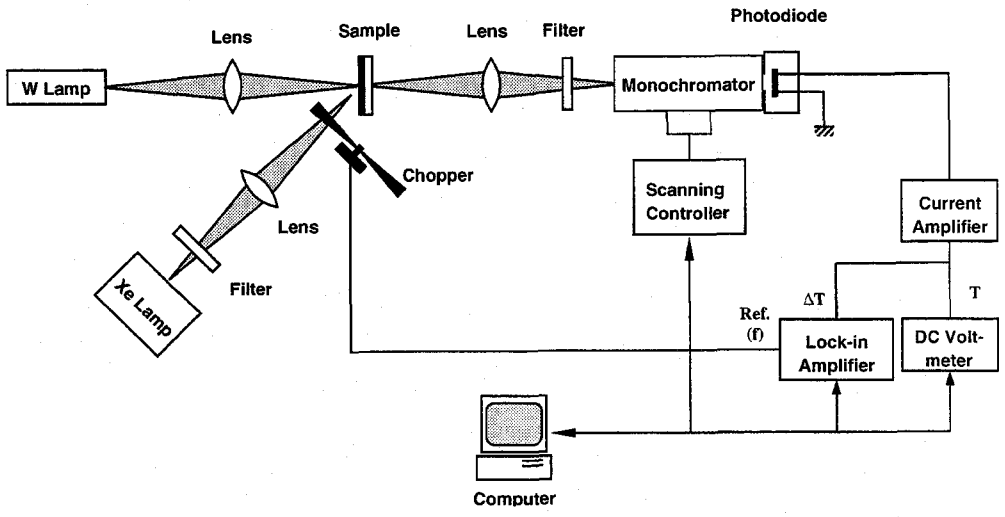

Fig. 5.2. TAS measurements apparatus.

amplifier, the transmittance component, T, and modulation component, ΔT, were simultaneously measured by a dc voltage meter and a lock-in amplifier (NF Circuit Block, 5610B), respectively. TAS measurements were performed at room temperature.

Employing the TAS technique, the changes in optical absorption can be monitored due to following principle. Modulation spectroscopy including TAS is a derivative technique which emphasizes most rapid changes in a spectrum. The TAS signal, $-\Delta T/T$, reflects the change in the absorption coefficient, $\Delta\alpha$, according to the following principle. [17] Let us consider light transmission through the thin film with a thickness of d and with an optical absorption coefficient of α. If we can assume that the extinction coefficient, k, is much smaller than the refractive index, n, in the spectral domain for the measurement (this generally applies in the region where transmission measurements are possible), the average transmission, T, is given by

$$T = \frac{(1-R)^2}{\left(e^{\alpha d} - R^2 e^{-\alpha d}\right)}, \quad k \ll n, \tag{5.1}$$

where R denotes the average reflectivity. Multiple reflections in the thin film have been taken account in this formula. For $e^{2\alpha d} \gg R^2$, T is simply reduced to

$$T = (1-R)^2 e^{-\alpha d}. \tag{5.2}$$

For the modulation transmission we find

$$\frac{\Delta T}{T} = -\frac{2\Delta R}{1-R} - \alpha\Delta d - d\Delta\alpha, \tag{5.3}$$

by differentiation of Eq. (5.2). The first and the second terms on the right side should be neglected because ΔR and a are small in the spectral region for the transmission measurement. Therefore the third term is usually the leading term so that the modulation signal, $-\Delta T/T$, is proportional to the change in the absorption coefficient, $\Delta\alpha$, related to the temperature change:

$$-\frac{\Delta T}{T} \approx d\Delta\alpha. \tag{5.4}$$

5.3. Blue-Band Photoluminescence

Visible PL emission is observed from the *nc*-Si thin film grown by the RTA process. Figure 5.3(a) demonstrates the PL spectra of the *nc*-Si grown at 1200°C as a function of the annealing time. Apart from the emission intensity, the overall feature of the blue-band emission spectra appears to be less sensitive to the annealing time than expected, that is, the peak energy lies at 2.7 eV for 5 min and at about 2.5 eV for 3 min and 1 min, respectively. In contrast, PL intensity is increased by about one order of magnitude with increasing in the annealing time from 1 min to 5 min. Similar behavior is observed for the samples annealed for 5 min with various annealing temperatures as shown in Fig 5.3(b). The PL peak energy is kept almost constant, while the PL intensity is enhanced with an increase in the temperatures from 1000°C to 1200°C. The samples annealed at 800°C did not exhibit observable

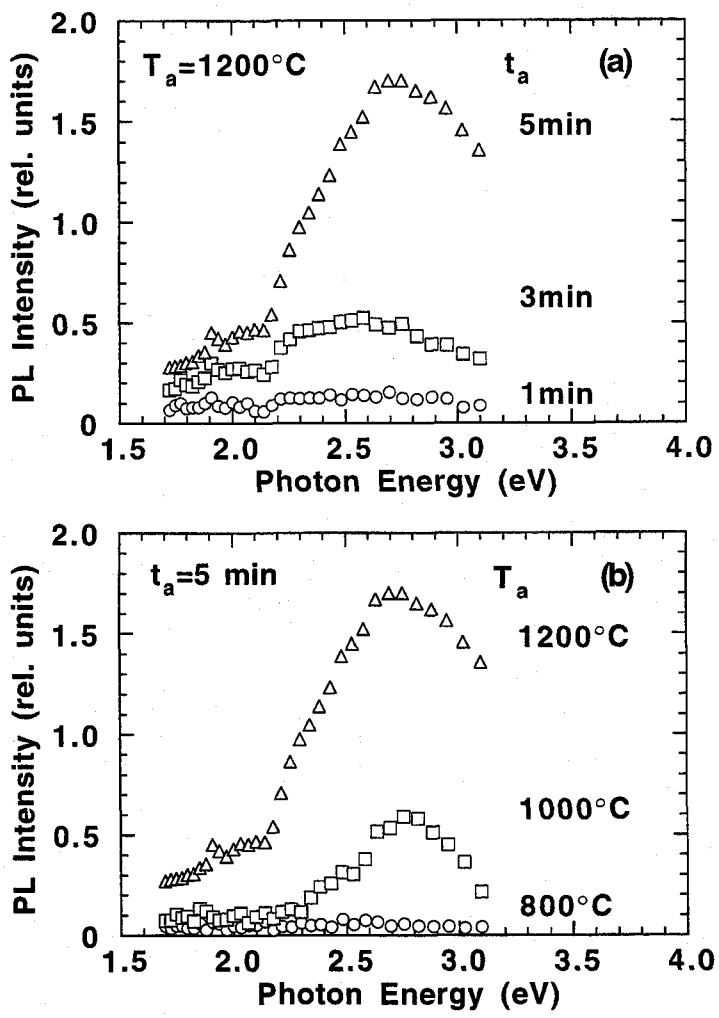

Fig. 5.3. PL spectra of the *nc*-Si annealed at T_a = 1200°C with changing of the annealing time t_a = 1–5 min (a) annealed for t_a = 5 min with T_a = 800–1200°C (b). PL measurements were carried out at room temperature employing 325.0-nm line of He-Cd ultraviolet laser as an excitation source.

emission within the annealing time of 5 min. The PL dependence on both annealing time and temperature is summarized in Fig. 5.4.

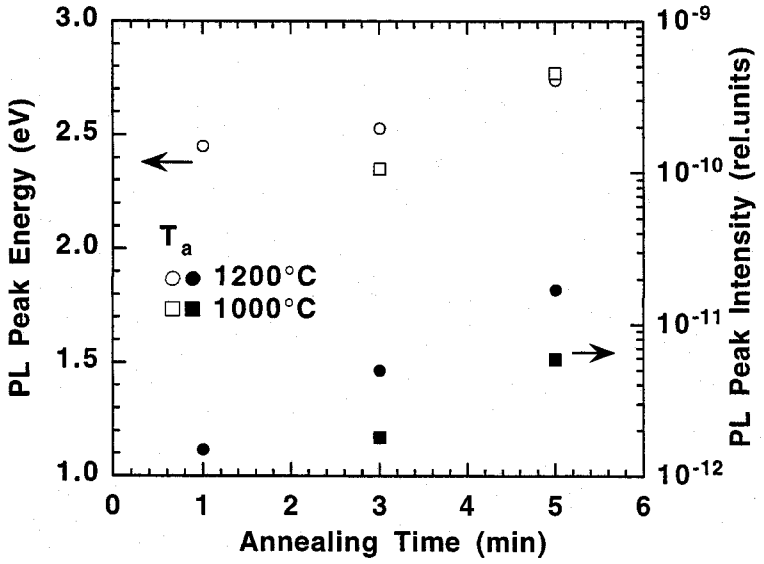

Fig. 5.4. PL peak energies and PL peak intensitis plotted against the annealing time. The *nc*-Si samples were processed at T_a = 1200°C (circles) and 1000°C (squares).

5.4. Structural Characteristics

5.4.1. Local Bond Vibration

As previously mentioned, the blue-band light emission observed from *nc*-Si, which is fabricated by various techniques, is interpreted within the context of three different models. Namely, the emission is ascribed to Si/SiO_2 interface states, defects in SiO_2 or quantum confinement effects on the basis of strongly oxidized *nc*-Si as summarized in Table 5.2.

On the contrary, IR transmittance spectra from our *nc*-Si exhibit no marked absorption associated with Si-O vibration mode. As shown in Fig. 5.5, the Si-O mode absorption at around 1100 cm^{-1} is not clearly found even in the sample annealed by the identical conditions for the blue-band light emission as displayed in Fig. 5.3. No substantial incorporation of SiO_x would be in good agreement with our annealing environment, namely, a vacuum condition. Furthermore, no

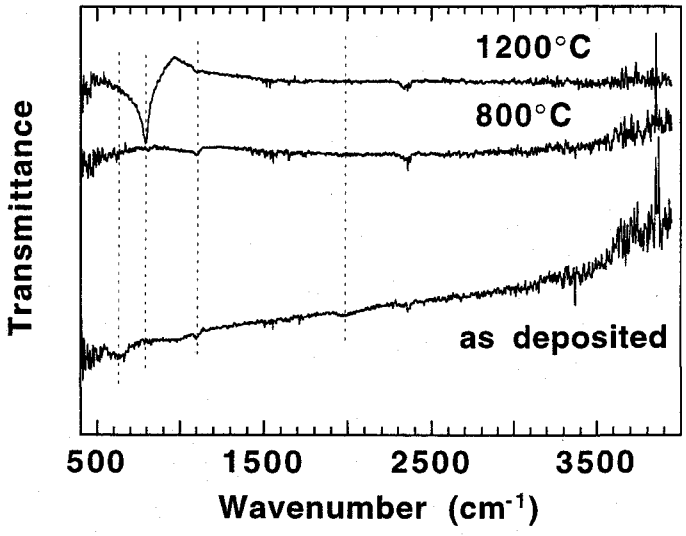

Fig. 5.5. IR transmission spectra of the *nc*-Si annealed at 1200°C and 800°C in comparison with that of *a*-Si:H as deposited. Dotted lines correspond to the vibration mode due to Si-H_x bonds (~630 cm^{-1}, ~2000 cm^{-1}), Si-O_x bonds (~1100 cm^{-1}) and unassigned absorption in the substrate (~790 cm^{-1}).

pronounced absorption arising from Si-H_x at 630 cm^{-1} or 2000 cm^{-1} and Si-OH mode at around 3500 cm^{-1} is also observed in RTA-processed samples as found in Fig. 5.5. [18] A very strong absorption located at 790 cm^{-1} appearing only from the sample annealed at 1200°C is the absorption in the *c*-Si substrate since the absorption is also observable from the substrate annealed at 1200°C without film deposition. The result of IR absorption spectra implies that the blue-band PL may occur from the *nc*-Si without strong oxidization. The possibility of the light emission associated with Si/SiO_2 interface states or defects in SiO_2 should be excluded in the present case.

5.4.2. Crystallite Size

If the grain size of the RTA-processed *nc*-Si is sufficiently small, the possibility to explain the blue-band PL in conjunction with quantum confinement effects on Si crystallites embedded in unknown dielectric silicide still remains. Thus the

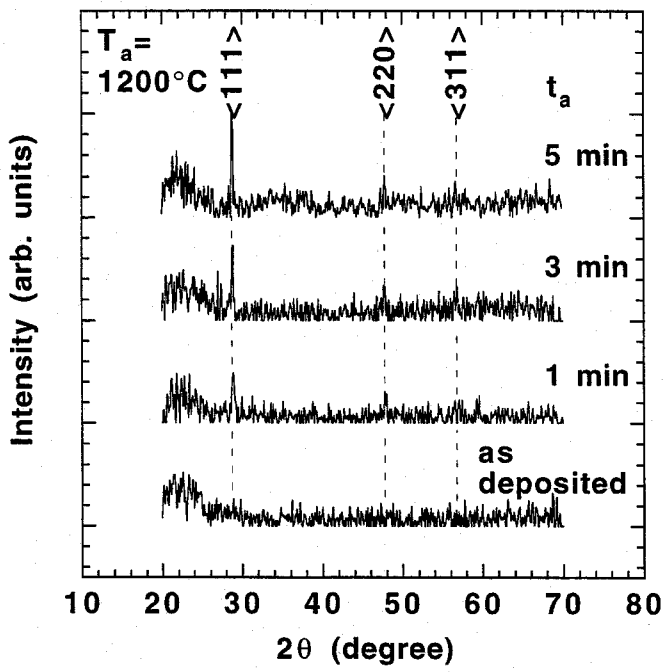

Fig. 5.6. XRD patterns for the *nc*-Si grown at 1200°C as a function of the annealing time. The bottom pattern was derived from *a*-Si:H before RTA process.

grain size of the *nc*-Si was estimated by means of both XRD and AFM measurements. As exhibited in Fig 5.6 regarding the *nc*-Si samples processed with various annealing time, the XRD pattern reveals growth of the *nc*-Si which is almost oriented to the <111> axis and slightly oriented to the <111> and <311> axes. According to the Schererr formula (see Eq. (4.1) in Chapter IV), [19] employing a full width at half maximum (FWHM) of the diffraction peak of the <111> axis, the average grain size of the *nc*-Si annealed at 1200°C for 5 min, from which blue-band emission is observed, is roughly estimated to be about 80 nm.

The grain size can be directly measured by the AFM surface image. Figure 5.7 displays the surface morphology of the blue-band light emitting *nc*-Si annealed for 1 min (Fig. 5.7(a)) and 5 min (Fig. 5.7(b)). The grains are clearly observed as ellipsoidal sphere-like shape. The diameter and height are estimated to be 50–100 nm and ~30 nm. The grain size from the surface view by AFM images is almost unchanged according to the annealing time and temperatures. Thus both

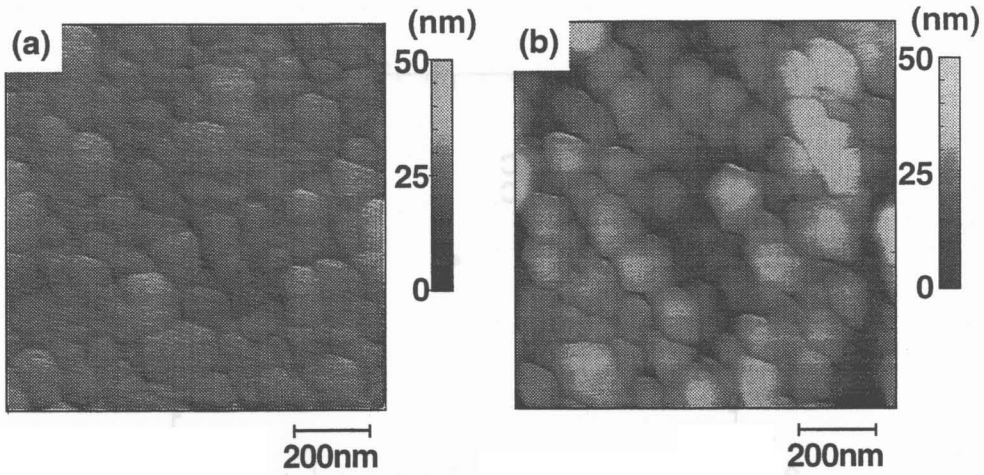

Fig. 5.7. AFM images of the *nc*-Si surface annealed at 1200°C for 1min (a) and 5 min (b).

XRD and AFM results indicate that the grain of the present *nc*-Si is as large as in tens-nanometer.

The PL with a peak energy of 2.7 eV as shown in Fig. 5.3 can be derived from the material at least with the band gap as large as the peak energy, if the carriers excited at both bands directly recombine. According to the calculations of the band gap on the quantum dot or quantum wire consisting of Si embedded in several materials, [2] the grain size should have a diameter less than 2 nm in order to enhance the band gap as high as the PL peak energy.

5.4.3. Correlation between Raman and PL Results

Furthermore, the relation between the grain size and PL properties are confirmed from a result of Raman scattering. As displayed in Fig. 5.8(a), the down-shift of the central frequency of transverse optical (TO) phonon mode with respect to *c*-Si increases with FWHM of the Raman spectrum. It is also found that the PL peak energy exhibits less sensitive against the Raman spectrum broadening in Fig. 5.8(b), while the PL emission intensity from the *nc*-Si decreases with the broadening in Fig. 5.8(c).

The increase in the Raman peak shift is found to be correlated the decrease in

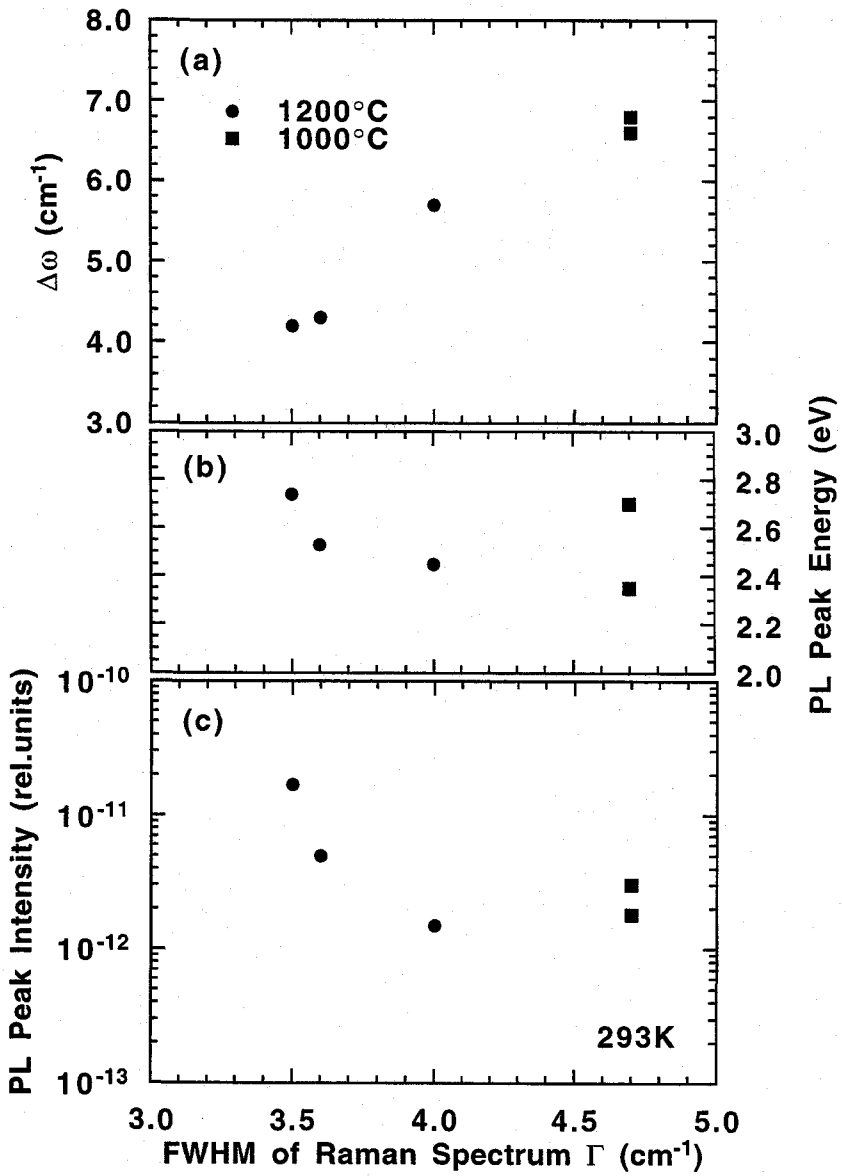

Fig. 5.8. Raman and PL results on the *nc*-Si plotted against FWHM of the Raman spectrum (Γ). Central frequency down-shift ($\Delta\omega$) in Raman spectra from the peak frequency of *c*-Si ($\approx$ 520 cm^{-1}) (a), PL peak energies (b) and PL peak intensities (c). The *nc*-Si thin films were annealed at 1200°C (●) and 1000°C (■) for various annealing time.

the crystal grain size because the shift and slight broadening of the Raman line have been explained as a result of phonon confinement in low dimensional material as mentioned in Chapter IV. [20] Thus the PL intensity tends to increase with the grain size of the *nc*-Si, while the PL peak energy is almost independent of the size. This tendency in the present *nc*-Si does not agree with the relation between PL and Raman spectra observed in porous Si. [21] These observations are almost impossible to be explained on the basis of the quantum confinements, so that the quantum size effects would be excluded from the key emission mechanism associated with the present *nc*-Si.

5.5. Optical Transition

5.5.1. Optical Transmittance

Any existing models for the blue-band PL emission cannot apply to our *nc*-Si thin films which contains little Si-O bonds and Si crystallites of which grain

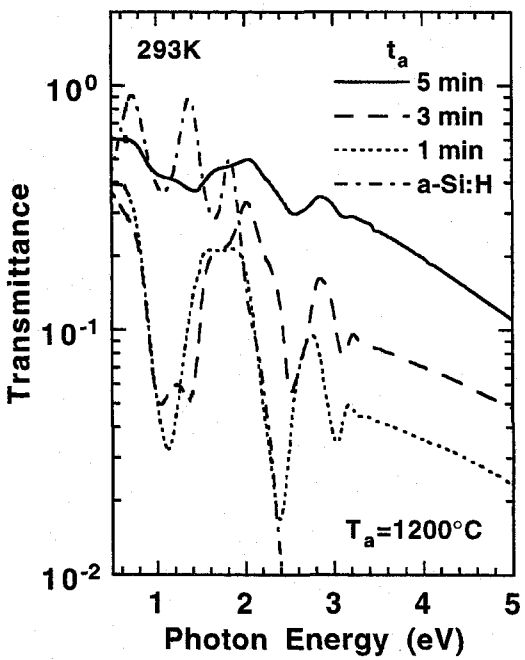

Fig. 5.9. Optical transmittance spectra of the *nc*-Si annealed at 1200°C as a function of the annealing time (t_a) [t_a: 5 min, solid line; 3 min, dashed line; 1 min, dotted line]. The dashed-dotted line is the transmittance spectrum of the *a*-Si:H before the RTA process.

size is relatively large. To seek for an alternative possibility, extended optical measurements were performed. Figure 5.9 displays transmittance spectra derived from the *nc*-Si thin films as a function of the annealing time, t_a. Also shown in Fig. 5.9 is the transmittance spectrum of *a*-Si:H before the RTA process with the large oscillation due to Fabry-Pérot interference. Any transmittance spectrum for the *nc*-Si is quite different from the spectrum for *a*-Si:H. The optical absorption edge of the *nc*-Si thin films seems to shift to blue with increasing the annealing time. In addition, the transmittance spectra of the *nc*-Si thin films involve the spectral features, i.e. the changes in the transmittance are found at the photon energies of ~1.1 eV, 2.4–2.6 eV and ~3.1 eV for any spectra of the *nc*-Si. In particular, the absorption at 2.4–2.6 eV seems to correspond to the PL emission band of the *nc*-Si.

5.5.2. *Differential Optical Transmittance*

In Fig. 5.10, TAS signals, $-\Delta T/T$, are plotted against the photon energy in the spectral region covering the observed PL band. The signals of the *nc*-Si annealed at 1200°C for various annealing time Fig. 5.10(a) and for 5 min at various annealing temperatures Fig. 5.10 (b), for which PL spectra are already shown in Fig. 5.3, are compared with that of *a*-Si:H as deposited. Above 2.8 eV, all of the TAS signals for the *nc*-Si markedly increase, while that of *a*-Si:H steeply rises at an energy of 2.1 eV near its optical energy gap. The signal rising onset is almost equivalent at around 2.8 eV for any annealing time. On the other hand, as displayed in Fig. 5.10(b), the onset energy shifts to higher energies with an increase in the annealing temperatures. The TAS signals sharply rise at 2.4 and 2.7 eV for the samples annealed at 800°C and 1000°C, respectively.

Since the modulated transmission, $-\Delta T/T$, is proportional to the change in the absorption coefficient, $\Delta\alpha$, against the temperature change, the onset of the TAS signal rising should reflect the rapid increase in the absorption coefficient. The blue shift of the onset energy from *a*-Si:H to the *nc*-Si would be interpreted as the shift of the optical absorption edge, depending on the annealing temperatures. Furthermore, the increase in the onset energy agrees with the decrease in the volume fraction of amorphous tissue in the films, which was evidenced by the Raman scattering spectra. The amorphous volume fraction almost disappears in *nc*-Si

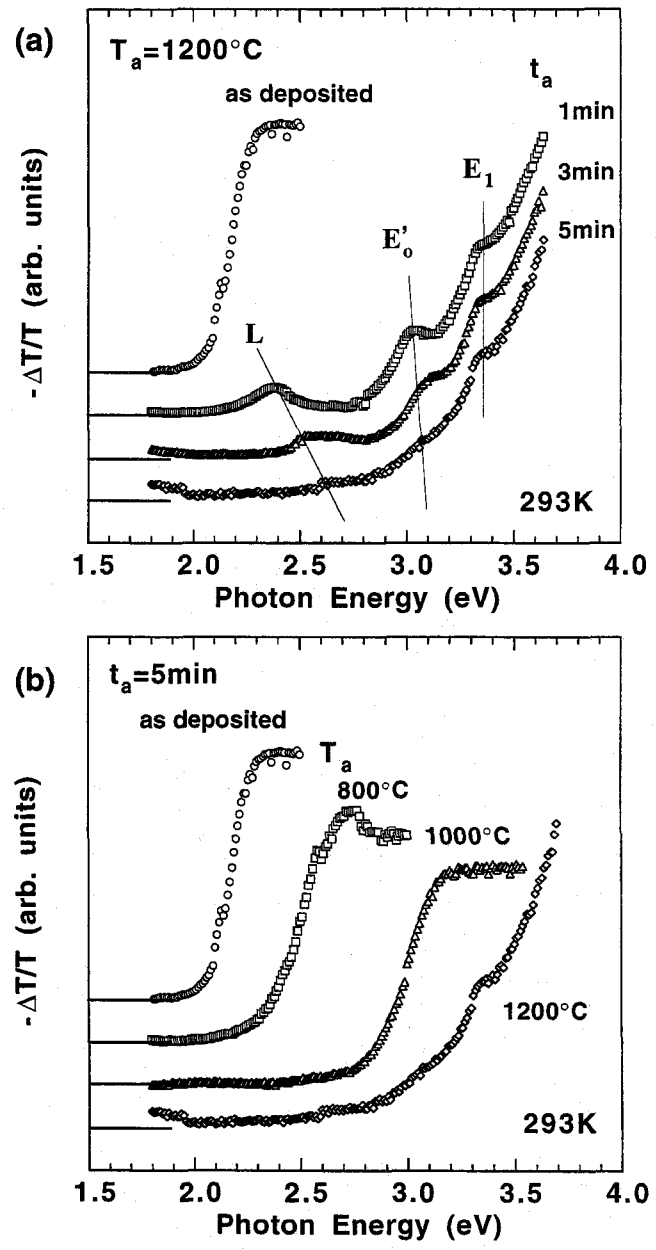

Fig. 5.10. TAS spectra of the *nc*-Si annealed at T_a = 1200°C with changing of the annealing time t_a = 1–5 min (a) annealed for t_a = 5 min with T_a = 800–1200°C (b) in comparison with that of *a*-Si:H as deposited. The labels indicate energies of optical transitions which might correspond to the signal features, at E_1 edge, E'_0 edge and localized states (*L*), respectively.

annealed at 1200°C. Thus the absorption in the remaining amorphous phase would make the lowest absorption edge, while the absorption in the crystallites should be related to the TAS signal rising with the onset energy of 2.8 eV appearing on the 1200-°C annealed samples which almost entirely consist of crystallites. In addition, the PL emission is hardly observed from the sample showing the onset energy below 2.7 eV. This implies the absorption due to amorphous phase might weaken blue-band emission.

The TAS signals on the 1200-°C annealed *nc*-Si in Fig. 5.10(a) also exhibit staircase structures at 3.0–3.1 eV and 3.4 eV. The staircase structures at 3.4 eV could be assigned to the $L_{3'v}$–L_{1c} optical transition at the E_1 edge, and the structures at 3.0–3.1 eV are close to the transition at the E'_0 edge in energy bands of a bulk *c*-Si [22]. Therefore the optical transition $\Gamma_{25'v}$–Γ_{15c} at the E'_0 edge is likely to form the lowest absorption edge which could be responsible for the blue-band emission.

The TAS signals also appear with the small peaks at 2.4 eV and 2.5 eV for the *nc*-Si annealed for 1 min and 3 min, respectively, and with the quite small structure at 2.6 eV for the 5-min annealed sample. The energetic location for the small structures is close to their PL peak energies. Furthermore, the other signal structures at lower energies of 2.4–2.6 eV observed on the 1200-°C annealed samples might be related to the absorption due to localized states found at the grain boundary region. If carriers recombine unradiationally through these localized states, the observation can be well accounted for that the smaller TAS signal intensity at 2.4–2.6 eV, the greater the PL intensity becomes.

5.6 Conclusions

I. Optical and structural properties of *nc*-Si thin films exhibiting the blue-band PL have been investigated. The *nc*-Si thin films were fabricated by solid phase growth employing the RTA method at 800–1200°C for 1–5 min in vacuum employing plasma-CVD-prepared *a*-Si:H.

II. PL occurs at room temperature with a peak energy of 2.5–2.7 eV, which is almost independent of the RTA temperature and time. By contrast, the PL intensity depends on the RTA conditions.

III. The *nc*-Si possesses structural features distinguished from blue-band emitting Si in literature, i.e. the *nc*-Si consists of crystallites with a grain size as large as 50–100 nm and little amount of Si-O_x bonds. Therefore the emission models based on *nc*-Si embedded in SiO_x matrix can not be adopted for this case.

IV. The differential optical transmittance spectrum of the *nc*-Si thin film measured by the TAS technique has three spectral features: at 2.6–2.7 eV, 3.0–3.1 eV and 3.4 eV. The latter two spectral features should correspond to the optical transition in the quasi three dimensional energy band structure in *c*-Si.

V. Since the spectral feature in the TAS spectrum at 2.6–2.7 eV corresponds to the PL peak energy of the film, the optical transition may be associated with the localized states on the boundary of *nc*-Si crystallites, and is the most possible origin for the PL emission.

References

[1] L.T. Canham, Phys. Stat. Sol. (b) **190** (1995) 9 and references there in.

[2] D.J. Lockwood, Solid State Commun. **92** (1994) 101 and references there in.

[3] as recent studies, Z.C. Feng and R. Tsu, *Porous Silicon*, (World Scientific, Singapore, 1994), R.W. Collins, C.C. Tsai, M. Hirose, F. Koch, and L. Brus, *Microcrystalline and Nanocrystalline Semiconductors*, (MRS, Pittsburgh, 1995).

[4] S. Sen, A.J. Kontkiewicz, A.M. Kontkiewicz, G. Nowak, J.Siejka, P. Sakthivel, K. Ahmed, P. Mukeherjee, S. Witanachchi, A.M. Hoff, and J. Lagowski, Mater. Res. Soc. Symp. Proc. **358** (1995) 369.

[5] H. Mimura, T. Futagi, T. Matsumoto, T. Nakamura, and Y. Kanemitsu, Jpn. J. Appl. Phys. **33** (1994) 586.

[6] J.M. Rehm, G.L. McLendon, L. Tsybeskov, and P.M. Fauchet, Appl. Phys. Lett. **66** (1995) 3669.

[7] X.Y. Hou, G. Shi, W. Wang, F.L. Zhang, P.H. Hao, D.M. Huang, and X. Wang, Appl. Phys. Lett. **62** (1993) 1097.

[8] D. Rüter, T. Kunze, and W. Bauhofer, Appl. Phys. Lett. **64** (1994) 3006.

[9] Q. Zhang, S.C. Bayliss, and D.A. Hutt, Appl. Phys. Lett. **66** (1995) 1977.

[10] X. Zhao, O. Schoenfeld, J. Kusano, Y. Aoyagi, and T. Sugano, Jpn. J. Appl. Phys.

33 (1994) L649.

[11] J.F. Harvey, H. Shen, R.A. Lux, and M. Dutta, J. Pamulapati, and R. Tsu, Mater. Res. Soc. Symp. Proc. **256** (1992) 175.

[12] H. Tamura, M. Rückschloss, T. Wirschem, and S. Veprek, Appl. Phys. Lett. **65** (1994) 1537.

[13] D.T. Jiang, I. Coulthard, T.K. Sham, J.W. Lorimer, S.P. Frigo, X.H. Feng, and R.A. Rosenberg, J. Appl. Phys. **74** (1993) 6335.

[14] A.J. Kontkiewicz, A.M. Kontkiewicz, J. Siejka, S. Sen, G. Nowak, A.M. Hoff, P. Sakthivel, K. Ahmed, P. Mukjerjee, S. Witanachchi, and J. Lagowski, Appl. Phys. Lett. **65** (1994) 1436.

[15] T. Toyama, T. Ouchida, H. Okamoto, and Y. Hamakawa, Appl. Surf. Sci. (in press).

[16] K. Hattori, T. Mori, H. Okamoto, and Y. Hamakawa, Phys. Rev. Lett. **60** (1988) 825.

[17] B. Batz, in *Modulation Techniques, Semiconductors and Semimetals*, vol. 9, eds. R.K. Willardson and A.C. Beer (Academic Press, New York ,1972) pp. 316–402.

[18] as references to assign IR spectral peak, P.J. Zanzucchi, in *Hydrogenated Amorphous Silicon, Semiconductors and Semimetals,* vol. 21, Part B, ed. J.I. Pankove (Academic Press, New York, 1984) pp. 113–140, P. Deák, Z. Hajnal, M. Stutzmann, H.D. Fuchs, Thin Solid Films, **255** (1995) 241.

[19] B.D. Cullity, in *Elements of X-Ray Diffraction* (Addison-Wesley Publishing, Massachusetts, 1956).

[20] I.H. Campbell and P.M. Fauchet, Solid State Comm. **58** (1986) 739.

[21] R. Tsu, H. Shen, and M. Dutta, Appl. Phys. Lett. **60** (1992) 112.

[22] G.E. Jellison Jr. and F.A. Modine, Phys. Rev. B **27** (1983) 7466.

Chapter VI

Application toward Optoelectronic Thin Film Devices

6.1. Introduction

In this chapter, we first elucidate the application to a hydrogenated amorphous silicon (*a*-Si:H) based photodiode founded on our new results associated with the avalanche multiplication in Chapter III. We have developed the *a*-Si:H/crystalline Si (*c*-Si) heterostructure as one of the alternative structures of the double insulating electroluminescence (EL) structure in order to transport the photogenerated carrier in *a*-Si:H to external electrodes. [1] Next, we present development of the thin film light emitting diode (TFLED) employing the electrochemically formed nanocrystalline Si (*nc*-Si) described in Chapter IV as a light emitting active layer. We have observed visible light emission from the *nc*-Si based TFLED for the first time as the entirely solid state device. [2,3]

A great deal of interest has been placed on *a*-Si:H based photodiodes provided with a photocurrent multiplication function because of its large impact on a variety of high performance integrated imaging devices. There have already appeared several reports which demonstrate a photocurrent multiplication factor exceeding almost 10 under high reverse biased conditions. [4–7] However, the increased photocurrent tends to be accompanied by a rapidly growing dark current, resulting in a poor signal-to-noise ratio. Another deficit which impedes a wide spread use of these devices is a relatively slow response time being on the order of ten milli-

seconds.

This work is aimed at pursuing the possibility for removing these limitations by employing new junction structure and fabrication processes. The photocurrent multiplication factor over 30 and the signal-to-noise ratio of around 170 has been achieved on an *a*-Si:H/*c*-Si heterojunction photodiode without any marked increase in the dark current at the reverse bias voltage around 35 V. In this chapter, some details of photocurrent characteristics are described, followed by a brief discussion on the possible mechanism of the photocurrent multiplication. [1]

Extensive efforts have carried out to develop a novel light emitting diode (LED) based on *nc*-Si represented by electrochemically anodized silicon (porous Si) [8] which shows strong visible photoluminescence (PL) [9]. From the first observation of EL in Schottky barrier diodes [10,11] and *p-n* junction diodes, [12] the emission color covers almost whole the visible spectral region including blue [13] and the external quantum efficiency reaches about 0.2%. [14] Therefore it will be an attractive approach to fabricate light emitting *nc*-Si thin films due to combining both fabrication techniques of microcrystalline Si (μc-Si) thin films and porous Si for development of large area light emitting devices. Little work has been performed for EL emission from electrochemically formed *nc*-Si thin films produced from plasma-CVD-prepared μc-Si [15] as well as from polycrystalline Si fabricated by low pressure CVD. [16] The EL emission is obtained using an electrolyte junction in both cases.

Microcrystalline Si deposited by plasma chemical vapor deposition (CVD) have been successfully applied to the optoelectronic devices such as image sensors [17] and TFLEDs [18] as the *p*-type and *n*-type layers of the junction due to the higher dark conductivity than that of *a*-Si:H by several orders of magnitude. [17] The device fabrication utilizes fully the benefit of the plasma CVD method (i.e. large area deposition at low temperature on several substrates involving glass, steel and polymer films).

In this chapter, we present the entirely solid state *p-i-n* junction thin film light emitting diode (TFLED) incorporated with *p*-type *nc*-Si, undoped and *n*-type amorphous layers and the device performances of the *nc*-Si TFLED including EL and current–voltage characteristics. [2,3]

6.2. Amorphous Silicon/Crystalline Silicon Heterostructure High Gain Photodiode

6.2.1. *Device Structure*

The device employed in this work has a heterojunction structure fabricated on *n*-type *c*-Si substrate as shown schematically in Fig. 6.1. The *n*-type *μc*-Si (10 nm) and undoped *a*-Si:H (1.0 μm) were deposited by the plasma CVD method displayed in Fig. 2.2 on ion-implanted p^+-region in the *c*-Si substrates. Details of the plasma CVD conditions for undoped *a*-Si:H are almost the same as those enumerated in Table 2.1. An indium tin oxide (ITO) layer was formed on the front surface as a front side transparent electrode. To reduce dark leakage current, the peripheral region of the p^+-type *c*-Si other than the defined photosensitive pixel area (2.5 mm × 2.5 mm) was covered with thermal oxide, and the sample was encapsulated into a nitrogen purged package. Various photocurrent characteristics including the reverse bias voltage dependence and spectral response have been measured.

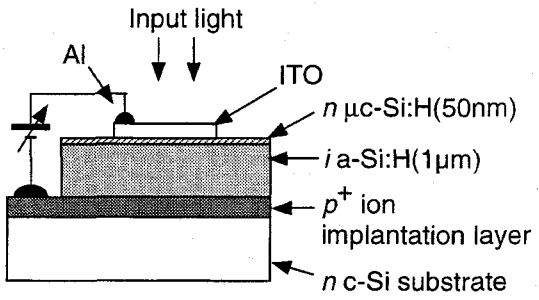

Fig. 6.1. Cross sectional view of the structure of the *a*-Si:H/*c*-Si heterostructrure photodiode.

6.2.2. *Device Performances*

Our prime concern in the present work is how the photocurrent behaves under the reverse bias condition, V_r, which is shown in Fig. 6.2. The photocurrent density, J_{ph}, appears to saturate upon applying reverse bias voltage of a few volts as commonly observed for the primary photocurrent in *a*-Si:H based photovoltaic devices. The photocurrent saturation occurs by the complete field-assisted collection

of photogenerated carriers and is determined basically by the optical absorption in the photovoltaic active undoped *a*-Si:H layer. The level defines I.Q.E. = 1, where I.Q.E. denotes the internal quantum efficiency, and the photocurrent density being relevant to I.Q.E. = 1 is denoted as J_{ph0}.

A distinguished feature found in Fig. 6.1 is a steep rise in J_{ph} occurred at the V_r at around 25 V. Highly contrasted to the marked increase in the photocurrent, the dark current exhibits no substantial increase over the range of V_r covered in this

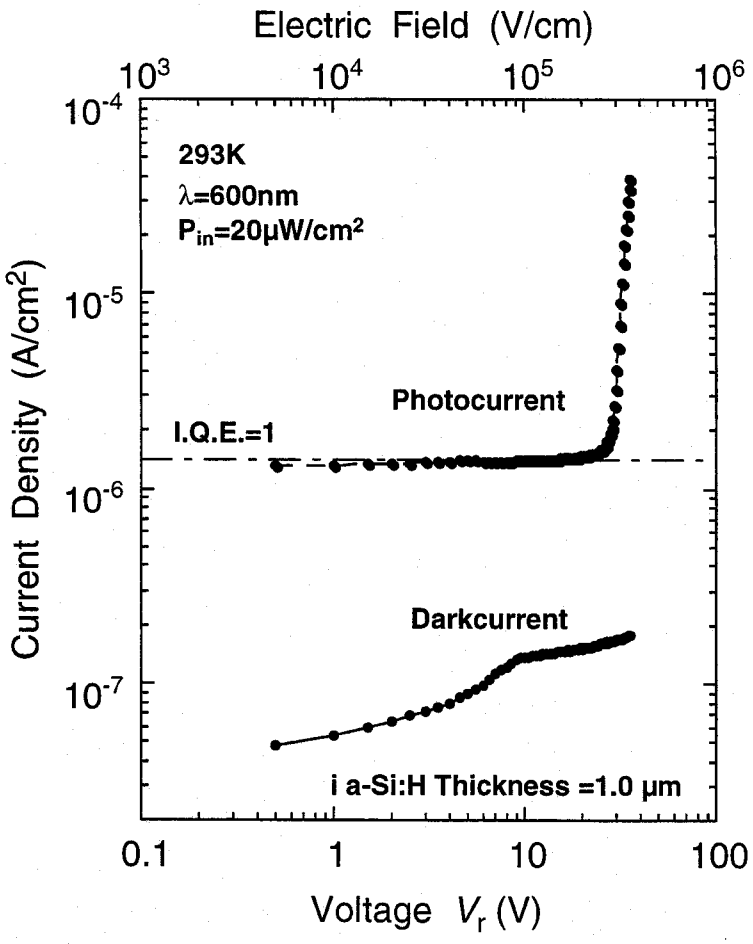

Fig. 6.2. Photocurrent (○) and darkcurrent (●) of the photodiode as a function of reverse bias voltage (V_r). The averaged electric field for *a*-Si:H is shown in the upper horizontal axis. The dashed-dotted line indicates that the internal quantum efficiency (I.Q.E.) is equal to unity.

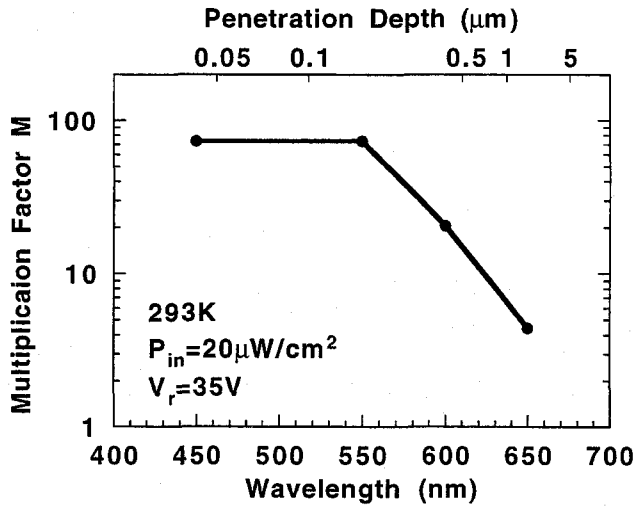

Fig. 6.3. Spectral response for photocurrent multiplication factor (M) at 293 K, P_{in} = 20 μW/cm^2 and V_r = 35 V. The penetration depth in a-Si:H estimated from the optical absorption coefficient is shown in the upper horizontal axis. The line is a guide for the eye.

experiment, so that the signal-to-noise ratio reaches around 170 for the light intensity, P_{in}, of 20 μW/cm^2. The photocurrent behavior under the deep reverse bias regime is reminiscent of the avalanche photocarrier multiplication although the onset electric field (shown in the upper horizontal axis) is unexpectedly lower than that expected for a-Si:H of 1 MV/cm as discussed in Chapter III. This point will be discussed later in conjunction with the photocurrent response time.

The photocurrent behaves practically in the same fashion as in Fig. 6.3 for various illumination wavelengths ranging from 450 nm to 650 nm. Figure 6.3 displays the photocurrent multiplication factor, $M = J_{ph}(35\ V)/J_{ph0}$, against illumination wavelength, λ. The photocurrent multiplication factor gets smaller for the illumination wavelength. If photocarrier generates uniformly over 1-μm thick photosensitive undoped a-Si:H layer, the spectral response in Fig. 6.3 suggests that holes generated in the vicinity of the n-type μc-Si/undoped a-Si:H interface may dominate the photocurrent multiplication.

To judge whether the photocurrent multiplication in Fig. 6.2 is the avalanche multiplication, extended investigation has carried out. If the avalanche photocarrier

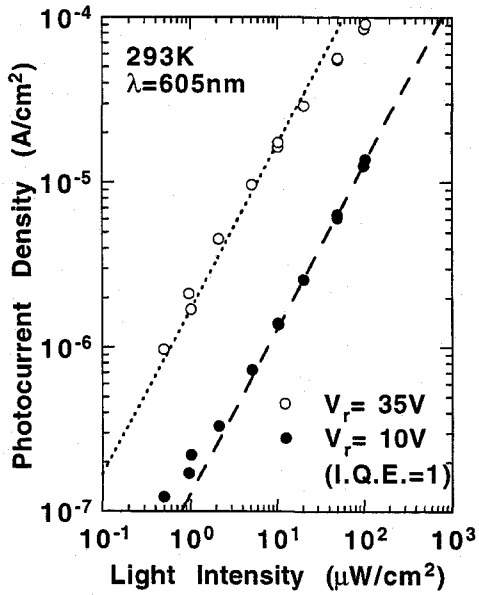

Fig. 6.4. Photocurrent density (J_{ph}) of the photodiode as a function of illumination intensity (P_{in}) at different bias voltages (V_a). [V_a: 10 V ($M = 1$), ○; 35 V ($M = 13$), ●]. The lines exhibit $J_{ph} \propto P_{in}$.

multiplication operates, J_{ph} would be proportional to the intensity of the incident light as usually does in the case of normal primary photocurrent, J_{ph0}. Fig. 6.4 demonstrates J_{ph} as a function of light intensity, P_{in}, for $\lambda = 605$ nm for two specific reverse bias conditions ($V_r = 10$ V and 35 V). J_{ph} appears to be proportional to P_{in}, excepting for the high P_{in} region, which convinces us that the photocurrent multiplication does not arise from secondary effects like carrier injection from electrodes, in which cases the photocurrent depends sublinearly on the illumination intensity. [4]

The experimental result of the temperature dependence of the photocurrent multiplication factor, M, on our *a*-Si:H device is shown in Fig. 6.5, where M at $V_r = 35$ V for the illumination wavelength of 600 nm is plotted against the absolute temperature, T. The multiplication factor, M, exhibits a weak positive temperature dependence although the experimental temperature covers only a limited range.

The time response analysis has been performed on the device to get more insight for the mechanism of the observed photocurrent multiplication. It turns out, although not shown in this article, that the photocurrent reaches the steady state level exceeding I.Q.E. = 1 at the order of ten milli-seconds after a step illumination and decays with the similar time constant after the cession of the

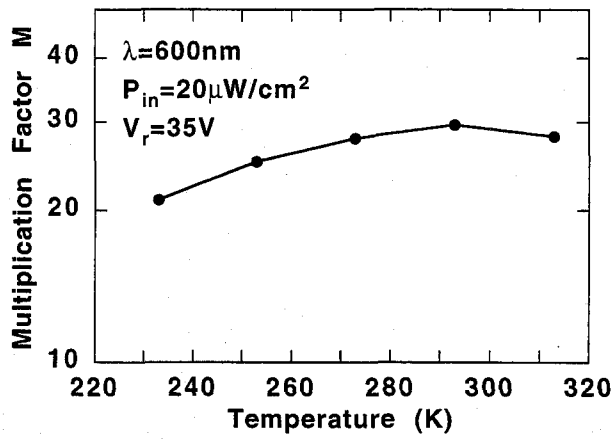

Fig. 6.5. Photocurrent multiplication factor (M) of the photodiode as a function of measurement temperature at λ = 600 nm, P_{in} = 20 μW/cm^2 and V_r = 35 V. The line is a guide for the eye.

constant illumination. Both the temperature and time dependence of the photocurrent cast a fundamental question on the mechanism of the photocurrent multiplication based on the avalanche photocarrier multiplication.

We can not draw any firm conclusion about the mechanism of the observed photocurrent multiplication at the present stage of the experiment, however, some points should be addressed here in favor of the avalanche photocarrier multiplication in our *a*-Si:H device. It should be noted here that the threshold electric field read for example from Fig 6.3 applies only if the externally applied voltage is uniformly distributed over the entire undoped *a*-Si:H layer. In reality, photogenerated carriers are to be trapped upon transport at deep localized states and give rise to a redistribution of electric field in the undoped *a*-Si:H layer, resulting in a formation of higher electric field regions, presumably in the vicinity of the *n*-type *μc*-Si/ undoped *a*-Si:H junction region. If the electric field in such a specific region exceeds 1 MV/cm, the avalanche carrier multiplication can occur. Since a built-up of the high electric field requires time corresponding to an average time of emission from mid gap localized states, that is on the order of ten milli-seconds, [19] the rise time of the photocurrent would be governed by this time scale. The same argument is likely to stand for the photocurrent decay time.

6.3. Nanocrystalline Silicon Light Emitting Diode

6.3.1. *Device Structure*

The structure of the TFLED is illustrated in Fig. 6.6. The *p*-type *nc*-Si thin film was electrochemically formed on a SnO_2-coated glass substrate from boron-doped *p*-type μc-Si as already explained in Chapter IV. Since the initial thickness of the *p*-type layer was set to be 200 nm as deposited (before anodization), the thickness must become less than 200 nm after anodization. On the *p*-type *nc*-Si layer, 50-nm-thick undoped *a*-Si:H, and 50-nm-thick *n*-type hydrogenated amorphous SiC (*a*-SiC:H) were sequentially deposited by the plasma CVD method with the deposition temperature of 180°C. The use of *a*-SiC:H for *n*-type layer is refereed to the structure of a-SiC:H-based TFLEDs. [20] Finally, evaporation of Al back contact with an area of 0.033 cm^2 completed the construction of the TFLED.

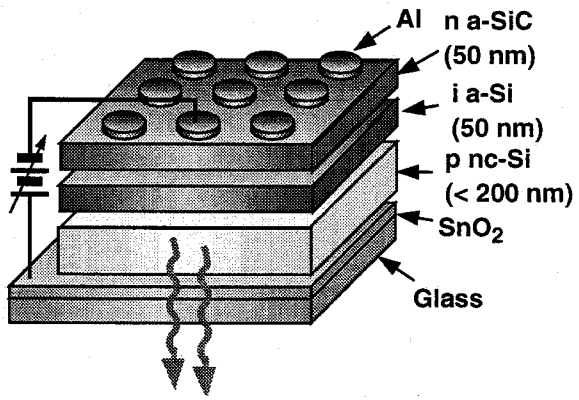

Fig. 6.6. Structure of *p*-type *nc*-Si/undoped *a*-Si:H/*n*-type *a*-SiC:H heterostructure TFLED. The *nc*-Si layer was electrochemically anodized from plasma-CVD-deposited μc-Si. The initial thickness of the *p*-layer was set to be 200 nm before anodization.

6.3.2 *J–V Characteristics*

As shown in Fig. 6.7, the entirely solid state TFLED consisting of *p*-type *nc*-Si, undoped and *n*-type amorphous layers exhibits clear rectification in the current – voltage (*J–V*) characteristics with a threshold voltage of about 1.5 V in the forward direction (applying positive bias on SnO_2) and the soft breakdown voltage of about 4–5 V for the reverse direction. The rectification ratio at 3 V is 33 and the series resistance is found to be almost negligible which is different feature from porous-Si-based LEDs in which large series resistance is commonly observed.

As shown the inset of Fig. 6.7 which is the logarithmic plot of the *J–V* characteristics, the *J–V* characteristics is approximately expressed by the conventional diode *J–V* characteristics given by [21]

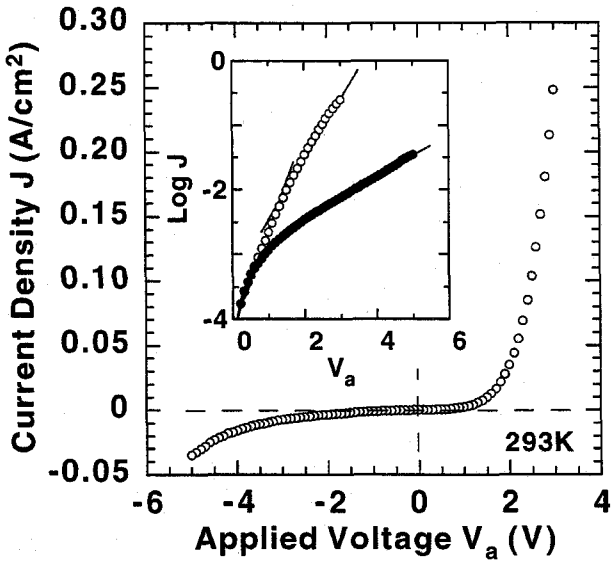

Fig. 6.7. *J–V* characteristics of the *nc*-Si TFLED at room temperature showing clear rectification. The diode ideality factor is quite large value more than 2. Inset shows the logarithmic plot of the *J–V* characteristics [forward; ○, reverse; ●].

$$J = J_0 \exp\left(\frac{eV}{nk_BT}\right), \tag{6.1}$$

where J_0 denotes the saturation current, V the applied voltage, k_B the Boltzman constant and T the temperature. As well known, the diode ideality factor, n, is taken between 1 and 2 for the conventional diode. The diode ideality factor, n, however, is estimated to be quite large value much more than 2 (n = 11 at V = 0–1.5 V, n = 18 at V = 1.5–3 V) for the forward current characteristics in the present TFLED. Furthermore, as shown the inset of Fig. 6.7, the exponential approximation can apply to the *"reverse"* (the light emitting direction) current characteristics with the huge ideality factor n of 50. The diode ideality factor more than 2 is also found in n-type ITO/p-type porous Si heterojunction diode in which the large factor (n = 8–10) is explained as due to the interface layer at the Si crystallite boundary [22,23].

The EL emission was detected only under the reverse bias voltage within the measurable spectral range of the photomultiplier (300–850 nm). In Fig. 6.8, the unmonochromated light output L is plotted against the current density J ranging in 0.1–2 A/cm^2. The EL intensity increases as the square of the current density. The

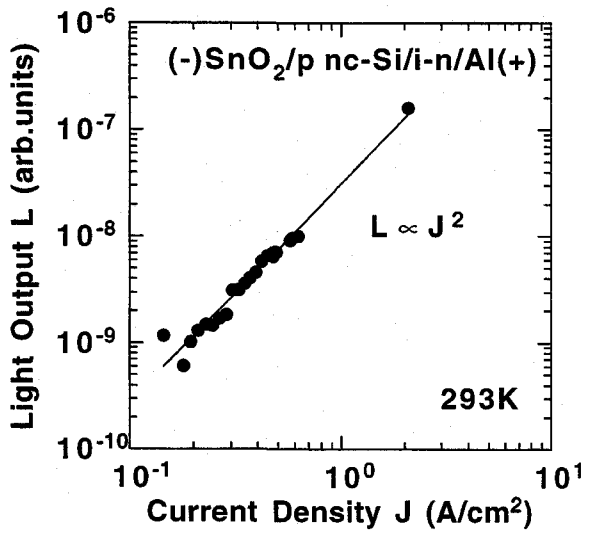

Fig. 6.8. *L–J* characteristics of the *nc*-Si TFLED at room temperature. The EL intensity increases with the square of the current density.

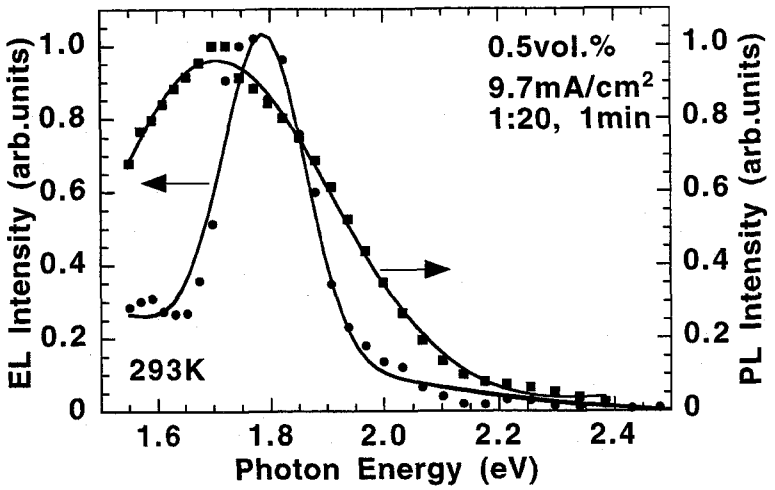

Fig. 6.9. EL (●) and PL (■) spectra from *nc*-Si thin film fabricated under the same conditions. EL spectrum was measured applying a reverse bias voltage of 4 V on the *p-i-n* structure TFLED. The lines are the fitting results to the Gaussian form, and the EL peak energy lies in 1.8 eV with FWHM of 0.2 eV.

square-law in the *L–J* characteristics is also observed in the *n*-type ITO/*p*-type porous Si heterojunction at current densities less than about 2 A/cm^2 in which it is likely to be ascribed to recombination at defects in the space charge region [22,23]. Since both *J–V* and *L–J* characteristics in the TFLED behaves as those in the *n*-type ITO/*p*-type porous Si heterojunction diode, it might be expected that the EL emission in the TFLED occurs rather at the *n*-type SnO_2/*p*-type *nc*-Si junction region than at the *p-i-n* heterojunction.

Figure 6.9 shows the EL spectrum of the *nc*-Si TFLED under a reverse bias voltage of 4 V. The light emission from the TFLED can be detected by naked eyes and the emission color is orange-red. Also shown in Fig. 6.9 is the PL spectrum of the *p*-type *nc*-Si layer fabricated by the same conditions including the *μc*-Si deposition and the electrochemical treatments. PL and EL measurements were carried out at room temperature employing the same detection system but with the observation directions from the *nc*-Si film side for PL and from the SnO_2/glass

substrate side for EL. If PL is measured from the glass side, the visible PL emission from the commercial glass substrate merges into the PL emission from *nc*-Si. The EL spectrum from the TFLED shows the peak energy of about 1.8 eV and FWHM of 0.2 eV. The EL spectrum shifts to the higher energy and becomes narrower with a pronounced reduction of its lower energy emission in comparison with the PL spectrum.

6.5. Conclusions

I. We have investigated various photocurrent characteristics in a heterojunction structure consisting of plasma-CVD-deposited *n*-type μc-Si (10 nm) and undoped *a*-Si:H (1.0 μm) layers on p^+-type ion-implanted region in an *n*-type *c*-Si substrate.

II. The photocurrent multiplication factor over 30 and the signal-to-noise ratio of around 170 have been achieved on an *a*-Si:H/*c*-Si heterojunction photodiode without any marked increase in the dark current at the reverse bias voltage around 35 V, although any definitive evidence can not be raised for the photocurrent multiplication based on the avalanche carrier multiplication mechanism from the present experiments.

III. We have investigated the entirely solid state TFLED on a SnO_2-coated glass substrate using electrochemically anodized *p*-type *nc*-Si as a light emitting active layer.

IV. The TFLED, of which *p-i-n* structure consists of the *nc*-Si and amorphous layers, exhibits clear rectifying *J–V* characteristics, while the visible EL emission is observed with applying the negative bias voltage on the SnO_2 electrode. The EL emission peak energy locates at 1.8 eV and observed emission color is orange-red.

References

[1] K. Ishida, S. Nakamura, T. Toyama, H. Okamoto, and Y. Hamakawa, Appl. Surf. Sci. (in press).

[2] T. Toyama, T. Matsui, Y. Kurokawa, H. Okamoto, and Y. Hamakawa, Appl. Phys. Lett. **69** (1996) 1261.

[3] T. Toyama, T. Matsui, T. Yamamoto, and H. Okamoto, Mater. Res. Soc. Symp. Proc. **452** (1997) (to be published).

[4] M.Yoshimi, T.Ishiko, K.Hattori, H.Okamoto, and Y.Hamakawa, J. Appl. Phys. **72** (1992) 3186.

[5] S.C. Jwo, M.T. Wu, Y.K. Fung, Y.W. Chen, J.W. Hong, and C.Y. Chang, IEEE Trans. Electron Devices **32** (1988) 1279.

[6] K. Sawada, I. Katayama, J. Yamazaki, M. Kosugi, and T. Ando, Jpn. J. Appl. Phys. **32** (1993) L39, K. Sawada, C. Mochizuki, S. Akata, and T. Ando, Appl. Phys. Lett. **65** (1994) 1364.

[7] S. Sugawa, K. Kozuka, T. Atoji, H. Tokunaga, H. Shimizu, and K. Ohmi, Jpn. J. Appl. Phys. **35** (1996) 1014.

[8] as recent studies, Z.C. Feng and R. Tsu, *Porous Silicon*, (World Scientific, Singapore, 1994), R.W. Collins, C.C. Tsai, M. Hirose, F. Koch, and L. Brus, *Microcrystalline and Nanocrystalline Semiconductors*, (MRS, Pittsburgh, 1995).

[9] L.T. Canham, Phys. Stat. Sol. (b) **190** (1995) 9 and references there in.

[10] A. Richter, P. Steiner, F. Kozlowski, and W. Lang, IEEE Elect. Device Lett. **12** (1991) 691.

[11] N. Koshida and H. Koyama, Appl. Phys. Lett. **60** (1992) 347.

[12] Z. Chen, G. Bosman, and R. Ochoa, Appl. Phys. Lett. **62**, 708 (1993).

[13] P. Steiner, F. Kozlowski, M. Wielunski, and W. Lang, Jpn. J. Appl. Phys. **33** (1994) 6075.

[14] J. Linnros and N. Lalic, Appl. Phys. Lett. **66** (1995) 3048.

[15] E. Bustarret, M. Ligeon, J. C. Bruyère, F. Muller, R. Hèrino, F. Gaspard, L. Ortega, and M. Stutzmann, Appl. Phys. Lett. **61** (1992) 1552.

[16] N.M. Kalkhoran, F. Namavar, and H.P. Maruska, J. SID, **3/1** (1995) 3.

[17] J. Kanicki, in *Amorphous and Microcrystalline Semiconductor Devices, Optoelectronic Devices* (Artech House, London, 1991) vol. 1.

[18] Y. Hamakawa, D. Kruangam, T. Toyama, M. Yoshimi, S.M. Paasche, and H. Okamoto, Optoelectronics – Devices and Technol. –, **4** (1989) 281.

[19] H. Kida, K. Hattori, H. Okamoto, and Y. Hamakawa, J. Appl. Phys. **59** (1986) 4079.

[20] S.M. Sze, in *Physics in Semiconductor Devices 2nd ed.* (Wiley, New York, 1981).

[21] F. Namavar, H.P. Maruska, and N.M. Kalkhoran, Appl. Phys. Lett. **60** (1992) 2514.

[22] H.P. Maruska, F. Namavar, and N.M. Kalkhoran, Appl. Phys. Lett. **61** (1992) 1338.

Chapter VII

Conclusions

A systematic study has been carried out on visible light emission from hydrogenated amorphous silicon (*a*-Si:H) and nanocrystalline Si (*nc*-Si). The main results acquired in this thesis work are enumerated as follows:

I. EL emission in *a*-Si:H at a high electric field over 1 MV/cm has been investigated employing ac-driven double insulating EL devices. EL emission involving a spectral component above the optical energy gap has been observed at the internal electric field in *a*-Si:H over 1 MV/cm. Intraband transitions of hot-electrons in conduction bands are the most likely mechanism for the EL emission.

II. The hot-electron-induced EL spectrum reflects the electron energy distribution. The lucky-drift model leads to the estimated mean free path of 1.0 nm and the average electron energy of 0.13 eV at the electric field in *a*-Si:H of 1 MV/cm, respectively. The estimated values are consistent with the prospected values in the previous reports on the investigations at the electric fields up to 0.5 MV/cm.

III. Utilizing the EA technique, the internal electric field in *a*-Si:H of the ac-driven double insulating EL device has been found to saturate at the fields of 1.2–1.5 MV/cm against increasing the applied voltage. Assuming the

electric field distortion due to generation of the transferred charge, the estimated transferred charge is found to rise sharply above the threshold fields of 1.2–1.5 MV/cm. The avalanche multiplication mechanism is the most acceptable explanation for the carrier multiplication.

IV. The electron impact ionization rate depends on the inverse of the square of the electric field in *a*-Si:H being independent of the *a*-Si:H thicknesses. From the dependence of the electron ionization rate on the electric field in *a*-Si:H, the mean free path of 1.0 nm at the ionization threshold energy of 1.8 eV has been estimated according to the luck-drift model.

V. The mean free paths deduced from the EL spectrum and from the ionization rate show the similar temperature dependence. With an increase in the temperature from 130 K to 300 K, the mean free paths gradually decrease in accordance with the theoretical line based on the optical phonon scattering process. In contrast, the mean free path turns to rise in the higher temperatures up to 400 K. This implies that the structural-disorder-induced may affect to the electron transport in a-Si:H even at high electric fields.

VI. The hot-electron-induced EL emission and the avalanche multiplication have also been observed on *a*-$Si_{1-x}C_x$:H ($x < 0.3$) alloys. The mean free paths of *a*-$Si_{1-x}C_x$:H evaluated from the EL spectra tend to decrease with increasing the optical energy gaps, and this tendency on the optical energy gap is consistent with that on the polarized EA results at low electric fields. This implies that the effect of alloy-induced structural disorder extends over electron states far away from the mobility edge.

VII. The *nc*-Si thin films were electrochemically anodized from the plasma-CVD-prepared *μc*-Si. The *nc*-Si thin films exhibit the red-band PL emission with a peak energy of 1.6–1.8 eV at room temperature and the PL properties change corresponding to the fabrication conditions including the anodizing current density, the anodizing time, the initial thickness and the crystalline volume fraction in *μc*-Si before anodization.

VIII. The Raman scattering and PL results indicate that the emission model based on the amorphous-like passivating layer is unlikely to explain the PL emission, while the both origins of quantum confinement effects and the surface states would be responsible for the visible light emission. The crystallite size of 2.4–3.8 nm depends mainly on the deposition conditions for *μc*-Si before anodization, while the surface states on the crystallites might be made active for the light emission due to anodization.

IX. The *nc*-Si thin films were fabricated by solid phase growth employing the RTA method at 800–1200°C for 1–5 min in vacuum employing a-Si:H. PL occurs at room temperature with a peak energy of 2.5–2.7 eV, which is almost independent of the RTA temperature and time. By contrast, the PL intensity depends on the RTA conditions.

X. The *nc*-Si possesses structural features distinguished from blue-band emitting Si in literature, i.e. the *nc*-Si consists of crystallites with a grain size as large as 50–100 nm and little amount of Si-O_x bonds. Therefore the emission models based on *nc*-Si embedded in SiO_x matrix can not be adopted for this case.

XI. The differential optical transmittance spectrum of the *nc*-Si thin film measured by the TAS technique exhibits three spectral features: at 2.6–2.7 eV, 3.0–3.1 eV and 3.4 eV. The first feature corresponds to the PL peak energy of the film, the optical transition which may be associated with the localized states on the boundary of *nc*-Si crystallites is the most possible origin for the PL emission. The latter two spectral features should correspond to the optical transition in the quasi three dimensional energy band structure in *c*-Si.

XII. Various photocurrent characteristics in a heterojunction structure consisting of *n*-type *μc*-Si (10 nm) and undoped *a*-Si:H (1.0 μm) layers on a p^+-type ion-implanted region in *n*-type *c*-Si substrate has been investigated. The photocurrent multiplication factor over 30 and the signal-to-noise ratio of around 170 have been achieved without any marked increase in the dark

current at the reverse bias voltage around 35 V.

XIII. The entirely solid state TFLED on a SnO_2-coated glass substrate using electrochemically anodized *p*-type *nc*-Si as a light emitting active layer has been developed. The TFLED, of which *p-i-n* structure consists of the *nc*-Si and amorphous layers, exhibits clear rectifying *J–V* characteristics, while the visible EL emission is observed with applying the negative bias voltage on the SnO_2 electrode. The EL emission peak energy locates at 1.8 eV and observed emission color is orange-red.

VITA

Toshihiko Toyama was born in Hamamatsu, Shizuoka, Japan in August 17, 1964. He graduated from Hamamatsu-Kita Senior High School, Hamamatsu in March 1983 and entered Osaka University, Toyonaka, Osaka in April 1983. He graduated from Osaka University in March 1987 and entered the Graduate School in April 1987. He received his Master of Engineering degree in Electronic Engineering in March 1989 from Osaka University. He has worked for Research and Development Center of Eastman Kodak (Japan) Ltd., Yokohama from 1989 to 1993. He returned to the Graduate School of Osaka University in April 1994.